PION PHOTOPRODUCTION IN THE (3,3) RESONANCE REGION

by

PETER ERIC BOSTED

B.S. Massachusetts Institute of Technology
(1975)

SUBMITTED IN PARTIAL FULFILLMENT
OF THE REQUIREMENTS FOR THE
DEGREE OF

DOCTOR OF PHILOSOPHY

at the

MASSACHUSETTS INSTITUTE OF TECHNOLOGY
(January 1980)

Signature of Author . . . . . .
Department of Physics, January 11, 1980

Certiied by . . . . . .
Thesis Supervisor

Accepted by . . . . . .
Chairman, Department Comittee

PION PHOTOPRODUCTION IN THE (3,3)RESONANCE REGION

by

PETER ERIC BOSTED

Submitted to the Department of Physics on January 11, 1980 in partial fulfillment of the requirements for the degree of Doctor of Philosophy.

ABSTRACT

Total cross sections for $^{12}C(\gamma,\pi^-)^{12}N$ and $^{7}Li(\gamma,\pi^-)^{7}Be$ have been measured from threshold to 360 MeV photon energy by detecting the radioactivity of the residual nuclei, thereby singling out the ground state of ^{12}N and the ground and first excited states of ^{7}Be. The cross sections are found to peak at about 40 MeV pion energy and then to fall gradually. In contrast to pion charge exchange and other photopion experiments, these results are well reproduced both in shape and in magnitude by distorted-wave-impulse-approximation calculations.

The differential cross sections at 90° for $^{10}B(\gamma,\pi^+)^{10}Be$ and $^{16}O(\gamma,\pi^+)^{16}N$ have been observed in the (1236) region (pion energies from 80 to 200 MeV). The contributions from the ground and first excited states in ^{10}Be are observed separately, while in ^{16}N the four lowest lying states were summed over. The data for $^{10}B(\gamma,\pi^+)^{10}Be$ are found to be in reasonable agreement with a preliminary DWIA calculation, while for the $^{16}O(\gamma,\pi^+)^{16}N$ case one calculation is in much better agreement with the data than another. The data represent the first photopion differential cross sections to discrete states of complex nuclei in the delta energy region.

Thesis Supervisor: Aron M. Bernstein
Title: Professor of Physics

ACKNOWLEDGEMENTS

I would like first of all to thank Professor Aron Bernstein for his continued advice and support. He has been an inspiration and a guide for almost six years of both undergraduate and graduate research. His constant zeal and enthusiasm have made him a positive pleasure to work with.

I would also particulary like to acknowledge the friendship of Ingvar Blomqvist, who has always had time to answer a question and tighten a bolt in the middle of the night, in spite of the myriad of activities in which he is constantly immersed.

I should also like to thank J. M. Laget, of the Saclay linear electron accelerator, for his great patience and persistence in our collaboration to calculate neutral pion cross sections. I am also indepted to C. Tzara, N. de Botton, J. L. Faure, E. Vincint, G. Audit, and C. Schull for all that I learned from them about theoretical and experimental physics.

I also warmly appreciate the help of the other graduate students in the photopion group, who have all helped at one time or another to take data or build and maintain the experimental apparatus. I would therefore like to thank Gregg Franklin, Nick Paras, Myron Pauli, Dana Row-

ley, Joe Comuzzi, Bryan Quinn, and Rori Miskiman.

I must also express my thanks to newly arrived Steve Dytman, who plunged into the experiment from the day he got here, and also to John Nelson who built the Cerenkov counters and wrote some of the data analysis progroms.

It would be hard to mention all the people at the Bates Linac who made these experiments possible, but I would escpecially like to acknowledge the untiring efforts of Lyman Stinson in providing research support and Bill Turchinetz in providing support and encouragement. Thanks also go to George Sechen for the huge amount of assistance he has been in the machine shop.

Last but not least there is my family, who has always helped and encouraged me to follow whatever goals I have set for myself. Without the love and support of my true friend Fran Bagenal much of this work may not have been possible.

BIOGRAPHICAL NOTE

The author was born in Lewisberg, Pennsylvania on the 10th of February, 1954. In 1960 his family moved to England for two years, and then to Belgium for three years, where he attended French speaking schools. Junior High School was spent in New Jersey, after which he attended Beverly Hills High School in California for three years. His freshman year was spent at Haverford College, after which he transferred to M.I.T., where he has been ever since except for a one year stay at the C.E.N. Saclay in 1976-1977 where he worked with C. Tzara and J. M. Laget. His main hobbies are music, mountaineering, rock-climbing, caving, skiing, and writing.

Table of Contents

Chapter I

Introduction

The basic purpose of this work is to describe recent experimental measurements involving photopion reactions in the $\Delta(1236)$ energy region. The experimental results will be compared to the available distorted wave impulse approximation (DWIA) calculations, which will be found to give reasonable accounts for the observed total and differential cross sections.

The $^{12}C(\gamma,\pi^-)^{12}N$ total cross section measurement will be described in Chapter Two, the $^{7}Li(\gamma,\pi^-)^{7}Be$ total cross section measurement in Chapter THree, and the differential cross section measurements for $^{10}B(\gamma,\pi^+)^{10}Be$ and $^{16}O(\gamma,\pi^+)^{16}N$ will be described in Chapter Four. Chapter Five will then summarize the results and present an outlook on the future of photopion physics.

The present chapter will attempt to give the reader some of the historical background to (γ,π) reactions, what has made them interesting, what new developments are likely to continue to make them interesting, and to show some of the general features. Considerations of time and space do not permit a great deal of detail; for this the recent (and only) book devoted exclusively to this subject, Photopion Nuclear Physics, P. Stoler Editor, Plenum Press,

N.Y. 1979, is recommended.

After the general features have been described, a more detailed description of the ingredients of DWIA calculations will be given, followed by a review of the experiments most relevent to those described in the present work.

I.1 General Overview

The first photopion experiments were closely tied in with exploring the structure of the nucleon. (BE55) The first measurement was about 30 years ago, and was used to confirm the mass and quantum numbers of the first excited state of the nucleon, known as the $\Delta(1236)$. It is also known as the (3,3) resonance because of its quantum numbers: spin 3/2 and isospin 3/2. The p-wave nature of the delta is seen in the angular distributions which peak at 90 (BE67). Subsequently higher excited states of the nucleon were seen with the (γ,π) reaction. Combined with inelastic electron scattering, $(e,e'\pi)$ coincidence experiments have been useful in giving evidence for the quark nature of the nucleon (FR72).

A. Photopion Reactions in Complex Nuclei.

While the elementary-particle aspects of photopion interactions are still ongoing, the recent impetus for new information has involved complex nuclei. The photopion reaction is of particular interest as it involves the exchange quanta for two of the four known forces, the elec-

tromagnetic and the strong. Since we think we understand the electromagnetic part, pion photoproduction can be used to study the interactions of pions and nucleons in nuclei with real pions. This then provides an intermediate ground between pion scattering, in which the probe does not penetrate very far into the nucleus due to its strongly interacting nature, and electron scattering, in which the effects of virtual pion emission and absorption are reflected in changes in the charge and current distributions in nuclei. In contrast, the photopion reaction can create real pions throughout the nucleus and explore their interactions as they leave.

B. Basic Ingredients.

There are three basic ingredients that enter into photopion reactions: the elementary production vertex, the coupling to the final and initial nuclear states, and the final state interactions of the produced pions. The detailed manner in which these are imbedded in calculations will be discussed later, but it may be useful to review some of their general features first.

The elementary operator for the free nucleon has two basic features. For charged pions, a term proportional to $\vec{\sigma}.\vec{\varepsilon}$ dominates the amplitude, thus giving rise to Gamow-Teller spin flip, isospin flip transitions if discrete final states are involved. For neutral pions, this term is reduced by the order of m_π/m_N, so that momentum

dependent terms play important roles even at threshold. At energies between 100 and 200 MeV pions, the M_{1+} part of the amplitude becomes dominant. This is explained in terms of delta creation and decay, as can be seen in Fig. I-1, where the total cross section for charged pions can be seen to peak near the mass of the delta. Note the large with of the resonance, (about 100 MeV), which is related to its short lifetime (less than $2 \cdot 10^{-23}$ seconds).

The nuclear structure contribution is seen in Gamow-Teller matrix elements near threshold, and analogs of the Fermi matrix elements at higher energies. We also find matrix elements that depend on nuclear derivitives. Although related to the matrix elements found in magnetic electron scattering experiments, the photopion matrix elements occur in different combinations, and some of them are not found at all in electron scattering. Although photopion reactions will probably not be used extensively for spectroscopic purposes, due to the strong final state interactions, they can be useful for investigating giant spin-flip states. This has been done for the 4.5 MeV complex of states in the $^{12}C(\gamma,\pi^+)B$ reaction, and several interesting states of this sort have been observed in radiative pion capture experiments (AL79, PE79).

The last main ingredient is the final state interactions of the outgoing pions. Much of the same information can be learned as from pion scattering. But, as mentioned

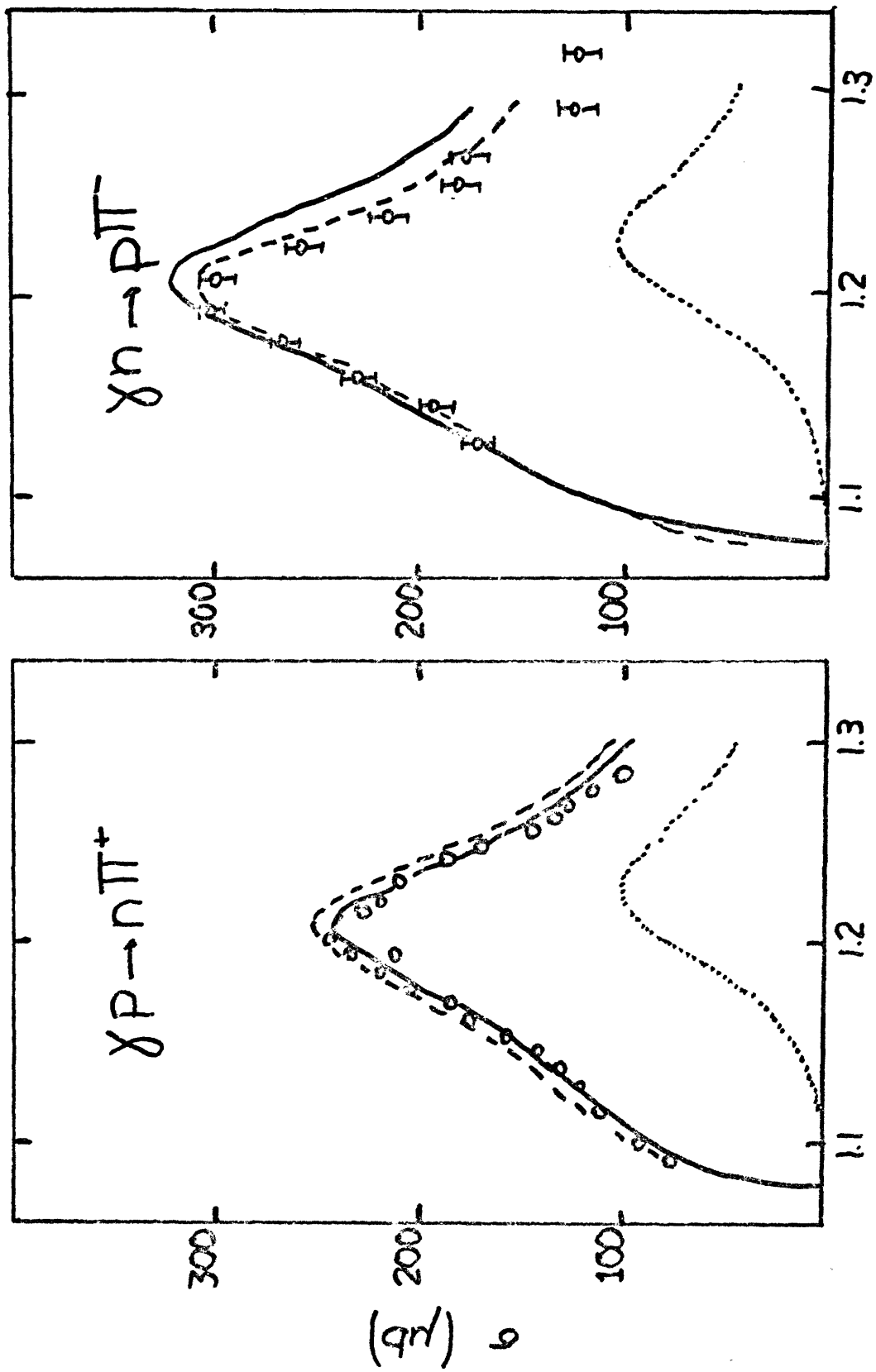

FIGURE I-1

before, pions can now be produced throughout the nuclear volume. In addition, isovector contributions can be explored as the initial and final nuclei differ for charged photopion reactions and do not for neutral pion production. The transition region between pionic atom data and the lowest energy pion scattering experiments can also be made with photopion reactions.

Before we go into how these ingredients are implemented in detailed calculations, it may be of interest to very briefly review the experiments to date involving complex nuclei.

C. Threshold Region.

Recently the basic reaction mechanism for photpion reactions has been put on a firm footing by the measurements of (γ,π^+) reactions with deuteron, ^{3}He, ^{6}Li, ^{9}Be, ^{12}C, and ^{16}O targets in the region a few MeV above threshold. Good agreement with calculations was found in all cases, to which should be added the results for $^{12}C(\gamma,\pi^-)$ and $^6Li(\pi^+_{15},\gamma)^6He$ (see BO79 for a comprehensive review). These measurements have only become possible recently using the high intensity linacs at Bates and Saclay.

Valuable information has been learned from stopped (π,γ) experiments, in particular the $d(\pi^+,\gamma)nn$ reaction in which the scattering length and effective range parameters for the nn system were measured. While many results exist for heavier nucei, in which many bound states are ob-

served, as well as structure in the continuum states, systematic explanations are lacking and quantum numbers have yet to be assigned to many of the observed features.

Experiments to examine (γ,π^0) from light nuclei have also been recently undertaken in the threshold region. While final analysis is not yet complete, it is clear that the impulse approximation is not sufficient to explain the results. This is because of the small size of the elementary amplitude: when rescattering diagrams are included such as ones where a charged pion is created from one nucleon and charge exchange scatters from another, qualitative agreement can be found. Binding effects have also found to be important in the near threshold region.

D. Medium Energy and Delta Regions.

There is presently a great influx of data in the intermediate energy region (about 10 to 50 MeV). In most of these cases differential cross sections for charged pion from complex nuclei are being observed, generally to discrete states of the final nucleus, although quasi-free production is also being examined. Work is presently going on for (γ,π^+) reactions in Japan, Saskatchewan in Canada, and at the Bates Linac (MIT/RPI). While many of the results are still being analyzed, the final results to date seem to be in qualitatively good agreement with DWIA calculations.

In the combined medium energy and delta regions there

are many older total cross section measurements made by detecting the radioactivity of the residual nuclei. The results of these experiments will be discussed in some detail in a later section. There are no differential cross section measurements to discrete states in complex nuclei. However, single and double arm experiments on the deuteron and ^{3}He performed at Saclay have shed valuable light on some of the two-body aspects of photopion reactions in the delta region.

The recent experiments for total photo-absorption in the delta region in light nuclei measured at Mainz have illustrated the strongly interacting nature of the delta. These measurements are being extended to heavier nuclei at Saclay and Bonn. Another reaction that is very sensitive to delta creation and decay is the (γ,p) reaction to discrete states of complex nuclei, where calculations are low by an order of magnitude if the effects of the delta are not included.

This brief introduction to the delta region will be considerably expanded upon in the last chapter of this thesis.

I.2 Theoretical Overview.

In this section we attempt to show some of the important ingredients of photopion calculations performed in the impulse approximation.

This approximation means that the production apmli-

tude is the sum of the free amplitudes applied to the bound nuclei within the nucleus. This approximation implicitly igrores two-body production mechanisms, interactions of propogating particles in the elementary operator with other nucleons in the nuclear medium, Pauli blocking of intermediate states, and binding energy effects. Given that this approximation does not do very well in explaining pion charge exchange reactions, in which the same initial and final states are probed with pions as in charge photopion reactions, it is somewhat surprising how well they have been found to do for photopion reactions. Part of this can be explained by the fact that phenomonological optical potentials fit to pion elastic scattering data have been used to calculate the wave functions of the outgoing pions. These potentials take many of these effects into account phenomonologically. The important distinction is that these effects have not been applied to the elementary operator part of the calculations.

In order to understand the framework for the preceeding discussion, and for useful reference when detailed accounts of the assumptions made in various calculations to which we will later compare our data, it is useful to have a more detailed account of the framework in which the calculations are performed. This is done in the next sections following the derivation of F. Tabakin and co-workers.

A. Basic Formalism

In their notation, one can write the amplitude as $F_{if} = \langle f|F|i\rangle$, where $F(\vec{q},\vec{k},\vec{\lambda})$ is a one body operator in the space of initial and final states given by

I.1 $$F(\vec{q},\vec{k},\vec{\lambda}) = \sum_{\alpha\beta} \langle \alpha|\hat{F}|\beta\rangle\, a_\alpha^\dagger\, a_\beta .$$

For a (γ,π^-) reaction, a_β would destroy a proton and $a_\alpha^\dagger$ would create a neutron. Here α and β define the orbital quantum numbers of the nucleons. The asymtoptic pion momentum is $\vec{q}$, while the photon has momentum $\vec{k}$ and polarization $\vec{\lambda}$. The single nucleon operator $\hat{F}$ is given by

I.2 $$\hat{F} = \Phi(\vec{r},\vec{q})\,(\vec{J}^S\cdot\vec{\Sigma})\,e^{i\vec{k}\cdot\vec{r}}$$

where Φ is the pion distorted wave function, $\vec{J}^S$ is the elementary operator, and $e^{i\vec{k}\cdot\vec{r}}$ is the photon plane wave. A schematic view of the process, ignoring meson exchange currents, is given in Fig. I-2a. A choice is now made to work in coordinate space rather than momentum space. The main advantage is that r-space optical potentials are currently considered to be more reliable below about 150 MeV pion energy. The disadvantage is that the operator will now contain derivatives $\vec{\nabla}_\pi$ and $\vec{\nabla}_N$ acting on the nucleons and pions, and approximations must be made for energies and momenta that appear in denominators in the elementary amplitude.

Defining KQ as the total angular momentum transfer

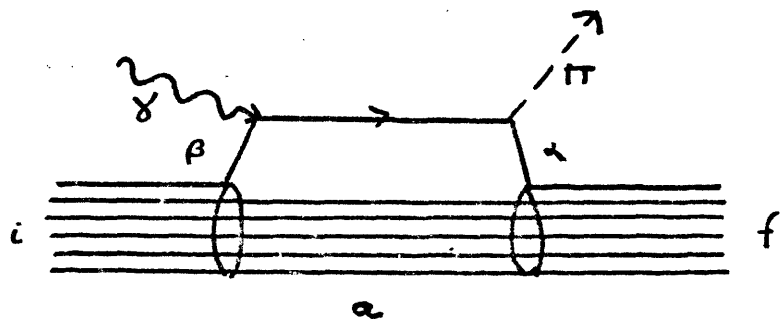

a

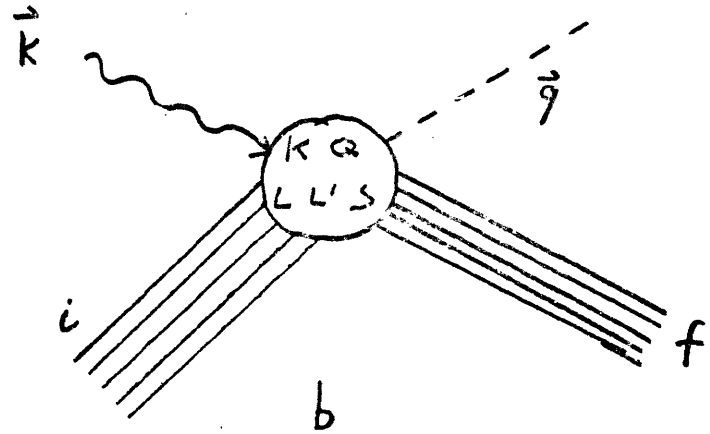

b

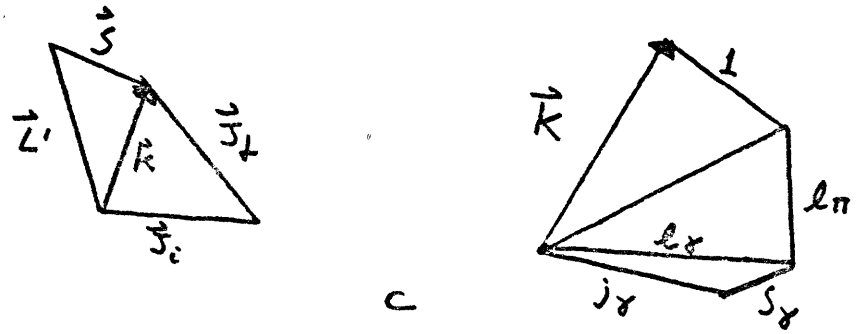

c

FIGURE I-2

from the $\gamma\pi$ to the nuclear system, $\vec{L}'$ as the associated orbital angular momentum transfer, $\vec{S}$ as the spin transfer, and $\vec{L}$ as the coupling of the pion to the photon orbital angular momentum (see Fig. I-2b), the tensor operator structure shown schematically in Fig. I-2c can be arrived at by introducing the diadic

$$\overleftrightarrow{1}_{\Omega} = \sum_{KQL} \int \overleftrightarrow{Y}^{KQ}_{L1}(\hat{r}) \; \overleftrightarrow{Y}^{KQ*}_{L1}(\hat{r}') \; d\Omega_{\hat{r}'} \qquad \text{I.3}$$

into I.2 If $\vec{J}^5$ is expressed as a sum of coefficients times independent combinations of operators, the angle space integrals can be performed. For example, the simplest term in $\vec{J}^5$ will be a constant times $\vec{\sigma}$. $\langle\alpha|\vec{\sigma}\cdot\vec{\varepsilon}\,|\beta\rangle$ can be seperated using the diadic into

$$\int R_{\alpha}(\vec{r}) \, d^3r \, (\vec{\sigma} \cdot \overleftrightarrow{Y}^{KQ}_{L1}(r)) \, R_{\beta}(\vec{r}) \, \chi^{KQ}_{L1\lambda}(r) \qquad \text{I.4}$$

where

$$\chi^{KQ}_{L1\lambda}(r) = \int d\Omega_{\hat{r}'} \, \overleftrightarrow{Y}^{KQ*}_{L1}(\hat{r}') \cdot \vec{\varepsilon}_{\lambda} \, e^{i\vec{k}\cdot\vec{r}'} \, \phi^{(+)}_{-q}(\vec{r}') \begin{cases} \vec{r}' : r\theta'\phi' \\ \vec{r} : r\theta\phi \end{cases}$$

This procedure can be followed for all possible terms in $\vec{J}^5$, leading to three basic types of angle space reduced matrix elements, denoted by ρ^{K}_{LLS}, where two of them have derivatives acting on the nuclear momenta. These can be expressed in terms of single particle operators. For example, for the one with no derivatives, one gets

$$\rho^{K}_{LLS}(r) = \sum_{ab} \langle J_f T_f || (a_a^{+} \times \tilde{a}_b)_{K;1} || J_i T_i \rangle (-1)^{\ell_a+1} [S][j_a][j_b][\ell_a][\ell_b]$$

$$\begin{Bmatrix} j_a & j_b & K \\ \ell_a & \ell_b & L \\ .5 & .5 & S \end{Bmatrix} \begin{pmatrix} \ell_a & \ell_b & L \\ 0 & 0 & 0 \end{pmatrix} R_a(r) R_b(r). \qquad \text{I.5}$$

The other two terms for the nuclear densities will be similar but involve radial derivitives. The advantage of this form is that the same tensor operator forms appear in electron scattering, except for the intermediate pion photon coupling L'. The final result can then be written as

$$\text{I.6} \qquad M_{fi} = \sum_{KQLL'S} G \int \rho^{KQ}_{LL'S}(r)\, r^2 dr\, \chi^{KQ}_{L'\lambda}(r) + \rho' \text{ and } \chi' \text{ terms.}$$

where n is an index over the different forms in $\vec{J}S$.

B. Nuclear Structure Inputs.

Let us first examine what the transition densities look like for a particular case, that of $^{12}C(\gamma,\pi^-)^{12}N$. There exists good quality data for the M1 electron scattering to the analogue state at 15.11 MeV, as shown in Fig. II-3. The transition densities needed for photoproduction have been fit to this data by various authors (HA78, OC72, UB72), who obtain some of the results shown in Fig. I-3. The three results shown all obtain similar values for the non- derivative densities, but small differences in the derivative ρ' terms. In the Helm model (UB72) (not shown), used by Nagl and Überall in their calculations, the terms are all zero. This assumption does not lead to drastic differences between calculations for the $^{12}C(\gamma,\pi^-)$ case, at least up to 100 MeV. The interesting thing to note from the figure is that the ρ terms, which dominate near threshold, are surface peaked, whereas

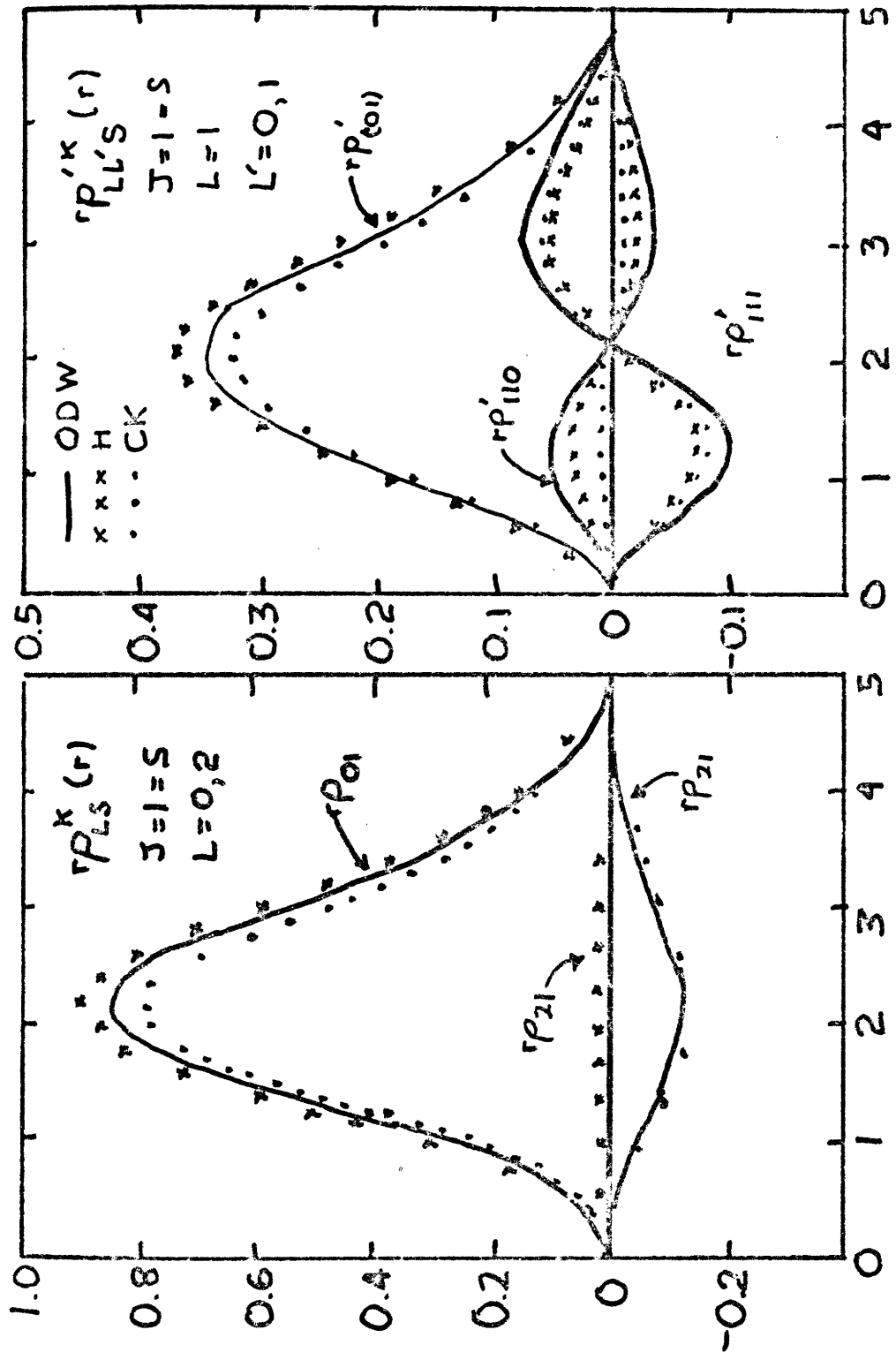
ODW
H
CK
$rP'^{K}_{LL'S}(r)$
J=1=S
L=1
L'=0,1
$rP'_{(01)}$
rP'_{110}
rP'_{111}
$rP^{K}_{LS}(r)$
J=1=S
L=0,2
rP_{01}
rP_{21}
rP_{21}
1.0
0.8
0.6
0.4
0.2
0
-0.2
0.5
0.4
0.3
0.2
0.1
0
-0.1
0
1
2
3
4
5
R(fm)

FIGURE I-3

the ρ' terms have a surface zero, meaning that volume production should become more important at higher energies. Since the pion absorption also increases at higher energies, there should be a net decrease in the cross section in the resonance region, a feature which has been observed in nearly all total cross section measurements.

C. Photoproduction Operator.

The next thing we need to know is the photoproduction operator. A large body of data exists from 15 MeV and upwards at many angles, both from the proton and the deutron, making possible accurate determinations of the $\gamma p \to n\pi^+$ and $\gamma n \to p\pi^-$ amplitudes. (see BE67 for a comprehensive review of the data). The total cross sections, shown in Fig. I-1, clearly show how the broad J=3/2, T=3/2 delta(1236) resonance dominates the cross sections (the dotted curve shows its contribution). The basic amplitude can be written in barycentric frame as

I.8 $$t_{\gamma\pi} = F_1\, i\vec{\sigma}\cdot\hat{\epsilon} + F_2\, \vec{\sigma}\cdot\hat{q}\,(\hat{k}\times\hat{\epsilon})\cdot\vec{\sigma} + F_3\, i\vec{\sigma}\cdot\hat{k}\,\hat{q}\cdot\hat{\epsilon} + F_4\, i\vec{\sigma}\cdot\hat{q}\,\vec{\sigma}\cdot\hat{\epsilon},$$

where $\vec{\sigma}$ is the nucleon spin and $\vec{\epsilon}$ is the photon polarization. The F's are on-shell functions of k and the pion angle and are usually expanded in terms of multipoles. The quantum numbers of the delta make the p-wave M1 multipole dominant in the resonance region.

Chew et al (CH57) first calculated the lowest order multipoles using dispersion relations. The imaginary

parts of the amplitudes can be related to known pion-nucleus scattering phase shifts and the real parts are then obtained using the unitarity of the S-matrix. Berends et al (BE75, Be71, BE67) later made more complete calculations and found good agreement with the existing data, to the level of 5% or better. The problem with the multipole approach is how to apply the amplitude when the nucleons are off their mass shell and how to transform from the pion-nucleon to the pion-nucleus frame.

To give a prescription for one solution to this problem, Blomqvist and Laget (BL77) calculated the amplitude from first principles by evaluating the seven diagrams shown in Fig. I-4. Using the usual Feynman rules and the pion coupling constant g_π, the first order Born terms with PV coupling can be unambiguously evaluated. For computational convenience, only terms up to m_π/m_N (m_π^2/m_N^2 for π^0 production) need be kept if the pion and photon momenta are kept below 350 MeV or so. The delta diagram is not so easy to evaluate as it is not well defined. They choose to use on-shell Rarita- Schwinger spinors, and of the two possible gauge couplings take only the one that contributes to the dominant $M1_+$ magnetic dipole coupling. The amplitude for the delta can be reduced non-relativistically to

$$\text{I.9} \qquad \frac{G_\pi G_3 G_2 G_1}{W^2 - M_\Delta^2 - iM_\Delta\Gamma}\left(\vec{S}\cdot\left(\vec{q} - \frac{q_0}{M_\Delta}\vec{p}_\Delta\right)\right)\left[S^+\left(\vec{k} - \left(\frac{M_N m}{m}\right)\vec{p}_i\right)\cdot\varepsilon\right]$$

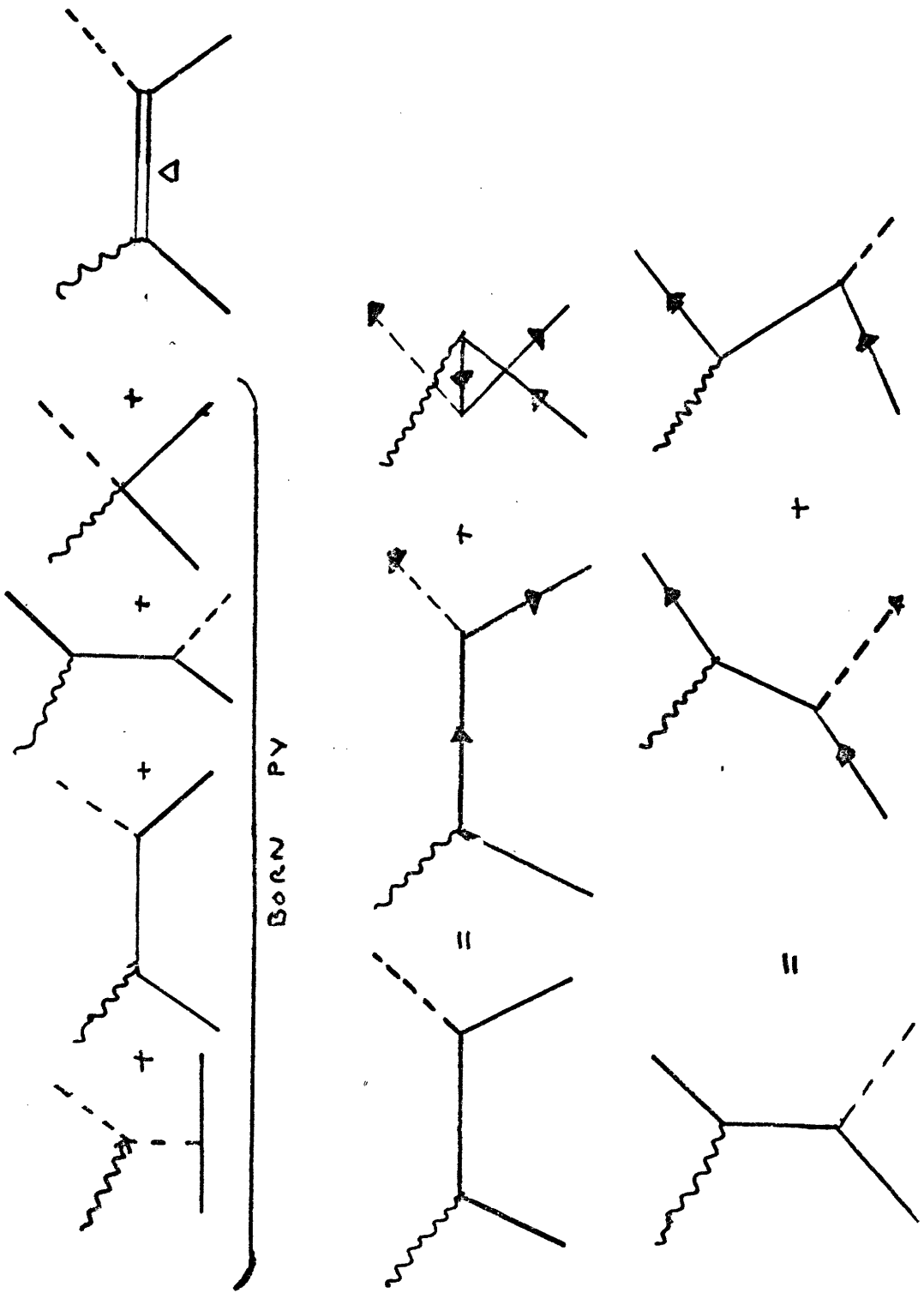

FIGURE I-4

G_3 and Γ are energy dependent functions of g_{π}, R, and $\vec{q}$, with M_3, g_3, and R being fit to the known multipoles.

Fig. I-5 shows the results when the lower order multipoles are extracted from both the relativistic and non-relativistic form of their amplitudes. The fits are quite good for the E_{0+} multipoles, which dominate up to 50 MeV, as well as for the $M_{1+}(3/2)$ multipoles, which dominates in the delta region. Fits to some of the smaller multipoles are not always so good, but are adequate for calculations to the 10% level for nuclear transitions, where their form of the elementary amplitude is particularly useful as it permits an unambiguous extrapolation to a moving frame. Still unsolved are the problems of possible double counting by the introduction of a separate isobar diagram and renormalization and other medium related effects that should, in principle, be taken into account in a full-blown many body dispersion relation calculation. Coupling of the propagating particles to a diagonalized set of intermediate nuclear states should also be taken into account.

D. Pion Distorted Waves

The last principle ingredient in (γ,π) calculations are the pion distorted waves. Most of our information on this subject comes from pion elastic and inelastic scattering. The data is usually fit by solving the Klein-Gordon equation with some form of an effective po-

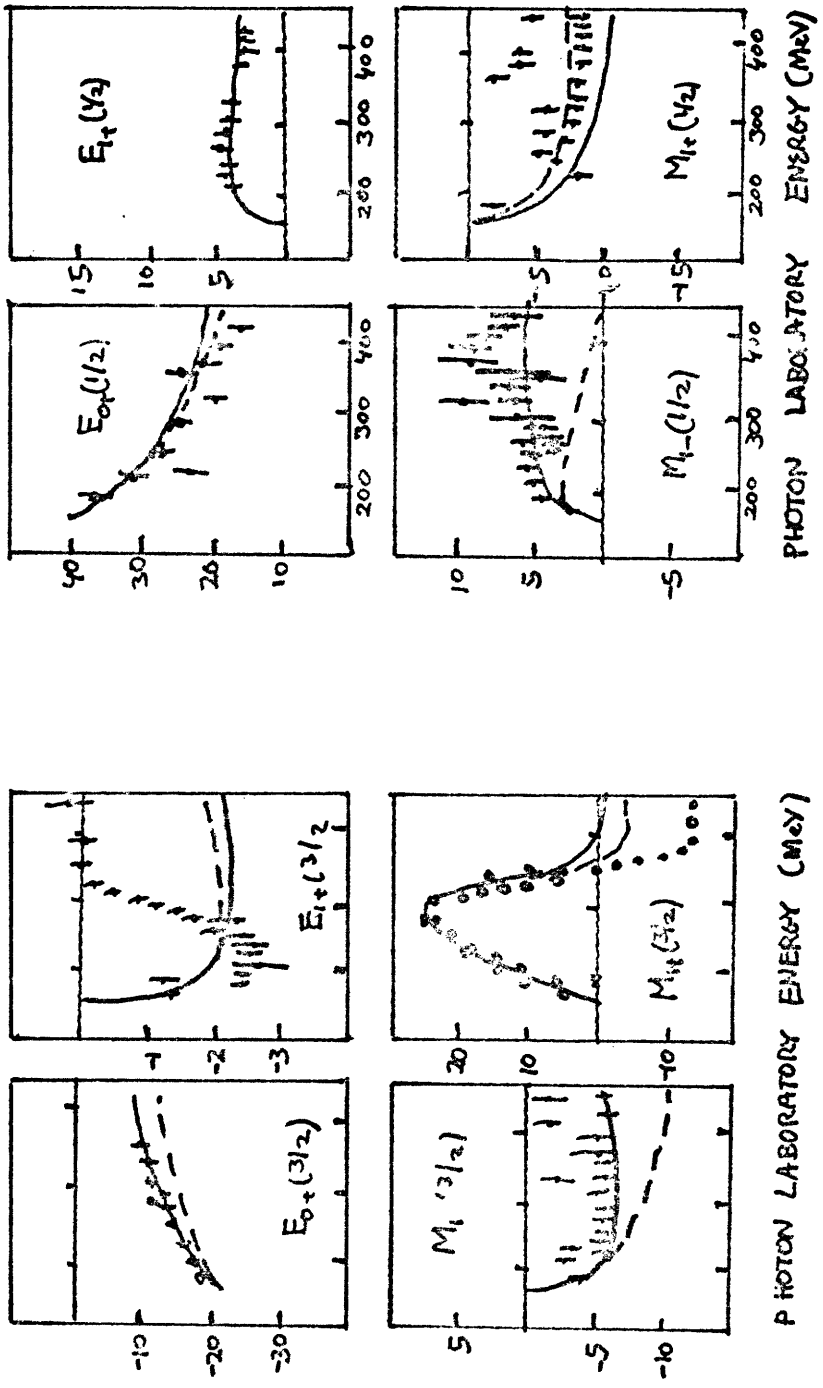
$E_{0+}(3/2)$
$E_{1+}(3/2)$
$M_1(3/2)$
$M_{1+}(3/2)$
$E_{0+}(1/2)$
$E_{1+}(1/2)$
$M_{1-}(1/2)$
$M_{1+}(1/2)$
PHOTON LABORATORY ENERGY (MeV)
PHOTON LABORATORY ENERGY (MeV)

FIGURE I-5

tential, known as the optical potential. The Klein-Gordon equation is obtained from the relativistic energy equation by including the electromagnetic potentials $\vec{A}(r)$ and $\Phi(r)$, which have the same Lorentz transformation properties as $\vec{p}$ and E. Setting $c = \hbar = 1$, one then obtains

I.10 $$(E - e\varphi)^2 - (\vec{p} - e\vec{A})^2 = m^2$$

Since the pion nucleus electromagnetic interaction is dominated by the Coulomb force, it is a good approximation to neglect $\vec{A}(r)$. Since the properties of the strong interaction are not well understood, it is commonly assumed that it can be uncluded with $e\varphi = V_c + V_N$, where V_c is the usual Coulomb interaction and V_N is the optical potential. Replacing $\vec{p}$ with $i\vec{\nabla}_r$ and arbitrarilly dropping the $2V_c V_N$ and V_N^2 terms (these should be kept at very low energies), one obtains

I.11 $$(-\nabla^2 + \ell(\ell+1)/r^2 + m_\pi^2)\Psi = (E^2 - 2V_c E + V_c^2 - 2E V_N)\Psi$$

The form of the optical potential used by Tabakin is that of Stricker et al (ST79) given by

I.12 $$2E_\pi V_{\pi-\eta} = -4\pi[P_1 b_o \rho + P_1 b_1(\rho_n - \rho_p) + b_2 \nabla^2\rho + P_2 B_o \rho^2 - \vec{\nabla}\,\alpha(r)\vec{\nabla}]$$

where

I.13 $$\alpha(r) = \beta(1 + \frac{4\pi}{3}\xi\beta)^{-1}$$

is a term which takes into account the Ericson-Ericson effect (polarization from the p-wave pion field) and higher order multiple scattering effects. $\beta(r)$ is given by

$$\beta(r) = P_1^{-1} c_0 \rho(r) + P_1^{-1} c_1 (\rho_n - \rho_p) + P_2^{-1} C_0 \rho^2(r)$$

P_1 and P_2 are kinematical factors given by $P_1 = 1+m_\pi/m$ and $P_2 = 1+m_\pi/2m$, and ρ and $\Delta\rho$ are the sum and differences of the proton and neutron densities (assumed to be spherically symetric) normalized to Z and N. The resulting radial equations for each partial wave can then be solved numerically.

The parameters b_0, c_0, b_1 and c_1 are energy dependent and can be related to the basic pion-nucleus amplitudes. In tne simplest picture, b_0 gives the πN s-waves (b_1 giving the isovector part) and c_0 the πN p-waves (c_1 again giving the isospin dependence). The ρ^2 terms are a somewhat ad-hoc way of accounting for pion absroption. Thus B_0 and C_0 are complex. Quasi-elastic absorbtion will come into play, causing the b's and c's to become complex above threshold, where they are purely real. Pionic aton studies (BA78) show the ρ^2 terms to be complex even at threshold, thus leading to exothermic behavior in the abscence of a Coublom potential.

As an example of how the rapidly improving elastic scattering data can be used to determine the isoscalar coefficients for the A=12 system, the results from π^+ scattering from ^{12}C at relatively low energies are compared in Fig. I-6 with curves calculated using a slightly modified version of the parameters determined by

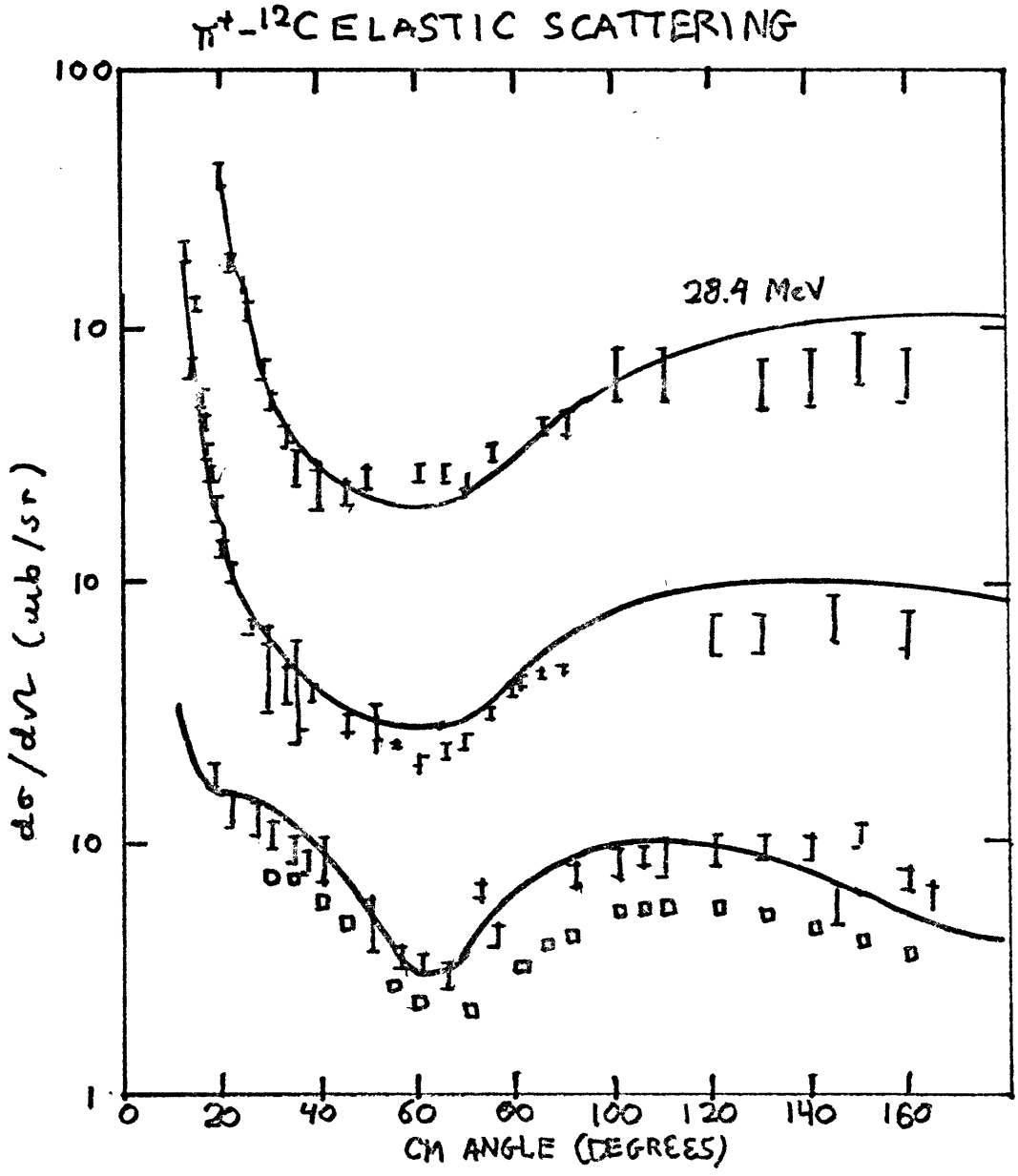
π+-12C ELASTIC SCATTERING
28.9 MeV
dσ/dΩ (μb/sr)
100
10
1
0
20
40
60
80
100
120
140
160
CM ANGLE (DEGREES)

FIGURE I-6

Stricker et al to fit this data (ST79).

One last point is that (δ,π) reactions may be sensitive to different phase-shift equivalent potentials (PSEPs). These involve short range unitary transformations to modify the scattering waves without affecting their asymptotic values, or hence elastic scattering results. Short range effects can thus be probed since different PSEPs dramatically affect inelastic scattering predictions (KE79). Tabakin (TA79) has not found much sensitivity to PSEPs for $^{12}C(\delta,\pi^-)$, but other cases should be investigated before any conclusions can be drawn.

I.3 Total Cross Section Measurements

In this section we shall review the existing data for total cross sections to discrete states in the final nuclei in the delta region. As mentioned before, this is primarly with a view towards understanding why the experiments described in the next two Chapters were chosen, as well as to see why better measurements for other cases are needed (this is gone into further in Chapter Five).

A. How the Measurements are Done.

In all cases, the radioactivity of the residual nucleus was used to determine the yield (pion cross section folded with the bremmstrahlung flux) as a function of endpoint energy (determined by the energy of the electron beam). If the efficiency is constant, the yield is given by

I, 14 $$Y(E_0) = \int_{E_{THRESHOLD}}^{E_0} \sigma(E)\, \Phi(E, E_0)\, dE$$

where σ is the cross section, Φ is the photon flux, and E_0 is the electron energy. The cross section is then found by deconvoluting the yield curve using the known shape of the photon spectrum. The principal competitor to the photopion reaction is a two-step process where a nucleon knocked out of one of the target nuclei by a low energy photon then charge exchanges by bouncing off one of the other target nuclei. Fortunately, this can be corrected for by measuring the yield below the pion threshold (around 150 MeV) and extrapolating to higher energies. Since the (γ,N) cross section is insensitive to high energy photons, the extrapolation can be done quite accurately, and the resulting subtraction is in any case generally not more than 30% of the pion yield in the resonance region. The other feature of activation measurements, as they are known, is that all the particle stable states in the final nucleus are summed over. Clearly the more states there are, the more difficult it is to interpert the experimental results.

B. $^{27}Al(\gamma,\pi^+)^{27}Mg$ and $^{51}V(\gamma,\pi^+)^{51}Ti$

This is just the problem for the first two cases I would like to discuss, $^{27}Al(\gamma,\pi^+)^{27}Mg$, and $^{51}V(\gamma,\pi^+)^{51}Ti$. Both have been measured several times by various groups (BL77), with the results for the latest and most reliable

measurements shown as the cross hatched areas in Fig. I-7. The previous experiments had not done as careful a job of subtracting the two-step background, which was measured directly in this case at each energy by using a stack of ten very thin target slices and using the thickness dependences of the different processes. (This method does not work for (γ,π^-) reactions due to the much shorter range of the proton). The dashed lines show the calculations by the same authors without final state interactions for various choices as to the number of final states, which are not well known for these cases. The dotted lines show the results when the final state pion interaction using various optical potentials are turned on. It can be seen that the predictions peak much too soon compared to the data, with too large a magnitude. It would appear that the total integrated strength might not do too badly if the yield curve were compared to directly, but the strength is at too low an energy. Whether there are problems with the data (these are difficult experiments) or the nuclear structure or pion distorted wave inputs to the calculations is not yet known. Interpretation will always be somewhat difficult due to the large unknown number of final states involved.

C. Heavier Nuclei.

The same group has, in fact, looked at several heavier nuclei (BL71), but they only took a few yield points

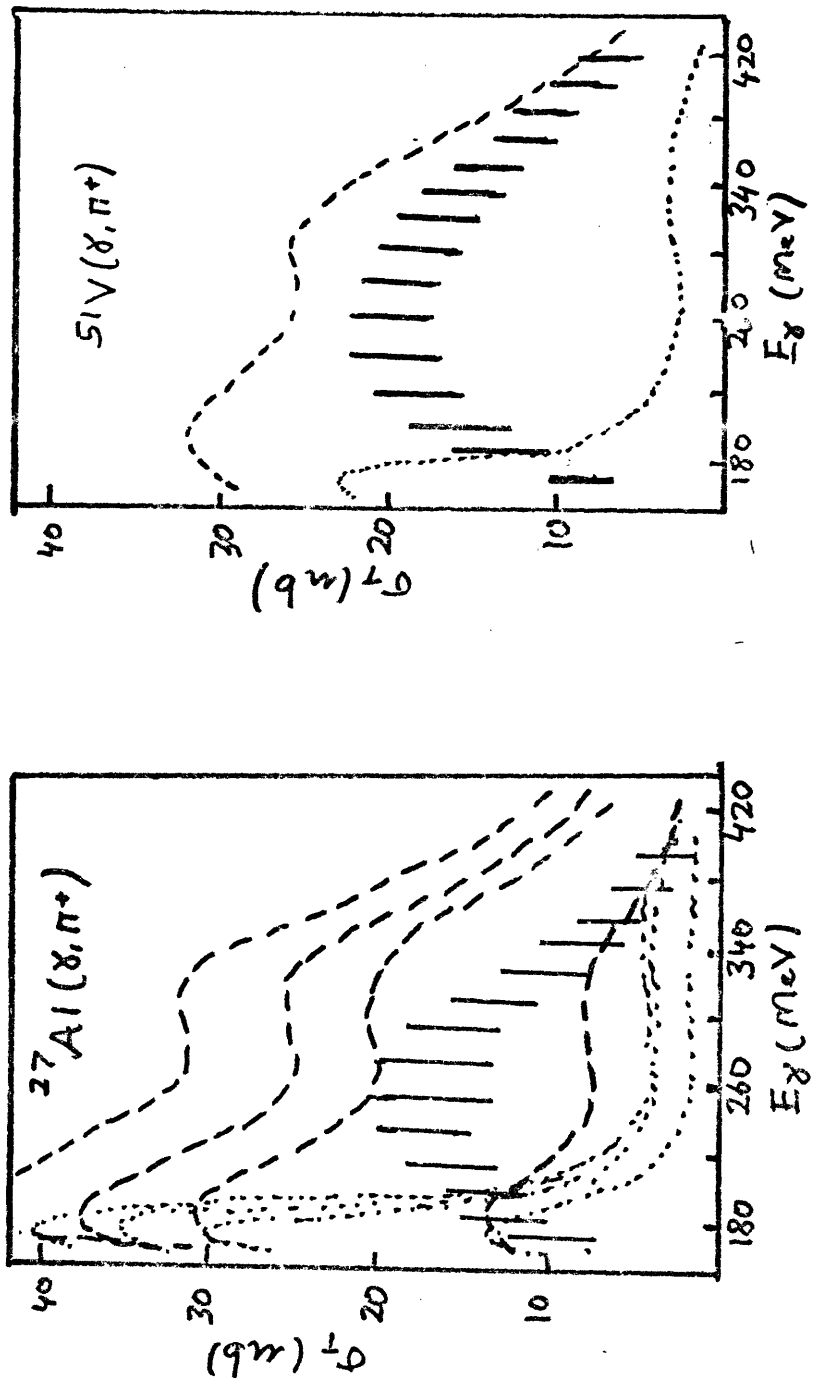
$^{27}Al(\gamma,\pi^+)$
$^{51}V(\gamma,\pi^+)$
σ_T (mb)
E_γ (MeV)
40
30
20
10
180
260
340
420

FIGURE I-7

with large error bars in each case. Since the data were not accurate enough to unfold directly, they simply took the ratio to their 1970 aluminium measurement (without the more accurate two-step subtraction). The number of particle stable final states was, in general, very large. The results for these ratios are shown in Table I-1. It can be seen that they are, in general, quite close to one, suggesting that it may be more interesting to measure one case accurately than a large number of different nuclei.

Reaction	Ratio
$^{11}B(\gamma,\pi^-)^{11}C$	1.2+0.1
$^{27}27Al(\gamma,\pi^+)^{27}Mg$	1.0
$^{41}K(\gamma,\pi^+)^{41}Ar$	0.6+0.1
$^{51}V(\gamma,\pi^+)Ti^{51}$	0.8+0.1
$^{68}Cu(\gamma,\pi^+)^{68}Ni$	0.8+0.2
$^{88}Sr(\gamma,\pi^+)^{88}Rb$	0.8+0.2
$^{138}Ba(\gamma,\pi^+)^{138}Cs$	0.5+0.1

Table I.1 Ratios of yield curves for various reactions to that from Al.

D. The $^{16}O(\gamma,\pi^+)^{16}N$ Reaction.

Moving on to lighter nuclei, we next come to the $^{16}O(\gamma,\pi^+)$ measurement of Meyer et al (ME65). There are four closely spaced final states in this case. The nuclear structure aspects of this case are fairly well constrained since the transverse form factor for the analog states in oxygen has been measured by electron scattering (the four states could not be distinguished). (DO75) The data is shown in Fig. I-8a compared with the calculations of Nagl (NA79) and Devenathan (DE79). It can be seen that

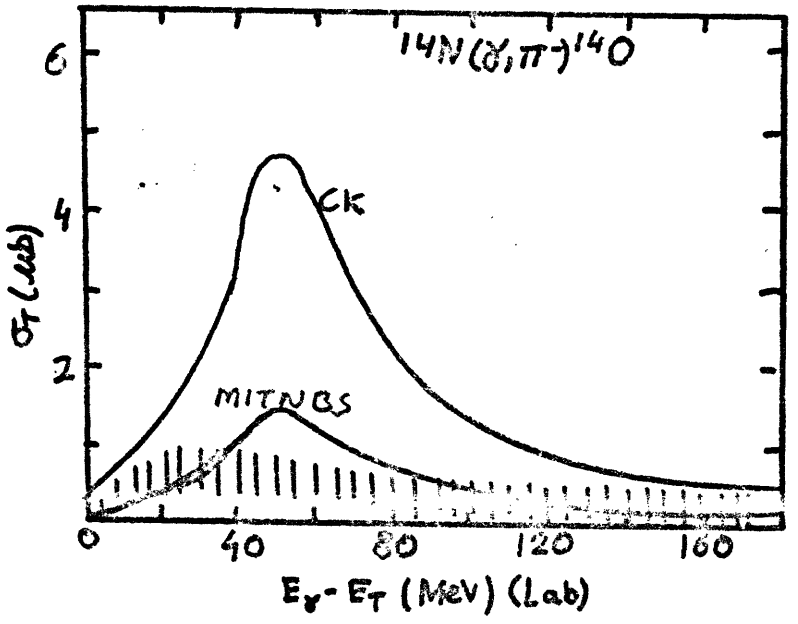
$^{14}N(\gamma,\pi^+)^{14}O$
CK
MITNBS
σ_T (mb)
6
4
2
0
40
80
120
160
$E_\gamma - E_T$ (MeV) (Lab)

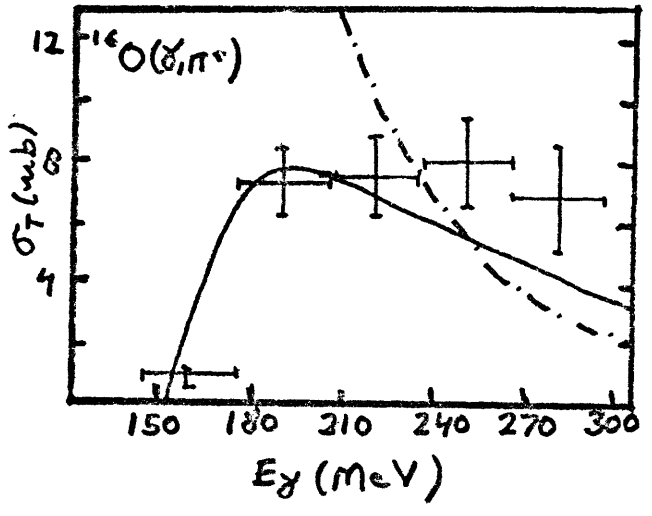
$^{16}O(\gamma,\pi^+)$
σ_T (mb)
12
8
4
150
180
210
240
270
300
E_γ (MeV)

FIGURE I-8

the results of Nagl, which use the Helm model (UB72) to fit the form factor, are much closer to the data than that of Devenathan, who used Rho's wave functions (RH69), which are not constrained to fit the known transverse form factor, and an asymptotic approximation to the pion gradient terms in the elementary operator, which explains why his cross section blows up at low energies. Unfortunatly, one does not know how much to trust the data, which is quite old and suffers from the fact that ordinary water was used as a target and large subtractions from $^{17}O(\gamma,p)$ and $^{18}O(\gamma,np)$ were necessary to extract the pion yield. A better measurement of this reaction would be helpful, particularly in view our recent differential cross section measurements for this case (se Chapter Four).

E. The $^{14}N(\gamma,\pi^-)^{14}O$ Reaction.

Another interesting reaction is $^{14}N(\gamma,\pi^-)$, which has only one particle stable final state and has recently been measured (DE79). The data are shown as the cross hatched area in Fig.I-8b. The first thing one notices is the extremely small size of the cross section, as one may have guessed from the stronly suppressed beta decay matrix element for this transition (AJ70). The low intensity of the Lund cyclotron made it impossible for the experimenters to obtain better than an order of magnitude measurement of this cross section. A calculation by N. Freed (DE79) used nuclear transition densities obtained from the

Cohen-Kurath (CC65) shell model code and was considerably higher than the data. The calculation of Singham (SI79) used MIT-NBS wave functions (which give a better magnetic form factor prediction) and is almost consistent with experiment. They also found great sensitivity in this case to the momentum dependent terms in the operator. It appears that the Kroll-Rudeman term is suppressed and that momentum dependent terms significantly reduce the cross section even right near threshold. Again, this would be a good candidate for a more accurate measurement.

F. Summary

The results for the experiments just described are impressive when the low average currents of the machines with which they were taken are considered, but with the much higher currents now available at Bates, Saclay, and elsewhere, it is now possible to improve the accuracy of total cross section photopion measurements by the activation method in reasonable amounts of running time (see Chapter Five for future plans regarding total cross section measurements). The measurements described in the next chapters are the first step in this direction, which was also accompanied by new inputs on the part of theorists, who have begun to examine these reactions with increasing care.

Figure Captions

I-1. The elementary total cross sections for $p(\gamma,\pi^+)n$ and $n(\gamma,\pi^-)p$. The data for the proton is from the multipoles of BE71 and BE75 while the neutron data comes from GU75 ano references therin. The solid line is the PV non-rel. calculation fo BL77, the dashed line is relativistc and the dotted line shows the effect of the non. rel. delta only.

I-2. Fig. a is a schematic representation of a nuclear photopion calculation. Fig. b shows how the calculation can be seperated with tensor couplings. Figure c defines some of the kinematic relations used in the text.

I-3. Transition densities for $^{12}C(\gamma,\pi^-)^{12}N$ reaction. Fits to electron scattering data of DU78 and FL79 by OC72, HA78 and of CO65 code.

I-4. The Feynman diagrams evaluated in the non-relativistic form of the elementary amplitude useful for nuclear calculations derived by Blomqvist and Laget (BL77).

I-5. Experimental multiploes for the elementary (γ,π) cross sections of BE72 and BE75 compared to prediction from BL77 with PV coupling. Dashed line is full relativistic prediction and solid line is non-relativistic reduction.

I-6. Elastic scattering data for ^{12}C at 30, 40, and 50 MeV of DO76, JO78, and DY77 compared with optical model fits of ST79.

I-7. The $^{27}Al(\gamma,\pi^+)$ and $^{51}V(\gamma,\pi^+)$ reactions from BL79. Hatched areas are experimental cross sections, while dashed (dotted) curves are their calculations without (and with) final state interactions.

I-8. Fig. a shows data for $^{14}N(\gamma,\pi^-)$ (hatched zone) of DE79 compared with calculations of SI79. CK means CO65 wave functions while MITNBS means M.I.T.-N.B.S. wave functions. Fig. b shows data for $^{16}O(\gamma,\pi^+)$ of ME65 compared with calculations of NA79 (solid curve) and DE79 (dashed curve).

Chapter 2

Total Cross Section for $^{12}C(\gamma,\pi^-)^{12}N$

II.1 Introduction

This chapter describes the measurement of the total cross section for $^{12}C(\gamma,\pi^-)^{12}N$ in the delta region. The reasons for doing this particular experiment are reviewed in the context of the previously existing data. The experimental setup is then described, with emphasis on the techniques particular to this experiment. The method by which the relative yields were extracted and converted to absolute yields and cross sections is described, and finally detailed comparison is made with the results of distorted wave impulse approximation (DWIA) calculations.

A. Experimental Motivation

There are several motivations for studying the $^{12}C(\gamma,\pi^-)^{12}N$ reaction in the reasonance region by the activation method. The first is that the residual nucleus has only one particle stable final state, facilitating comparison with calculations. The second is the fact that the two-step background arising from (γ,p) followed by (p,n) is strongly suppressed due to the large Q values for both reactions (AJ75). Unlike all other activation measurements that have been performed to date (see Chapter One for a review), where the yield from the two-step processes have been observed to be of the same order of magnitude as the photopion

Fig II-1

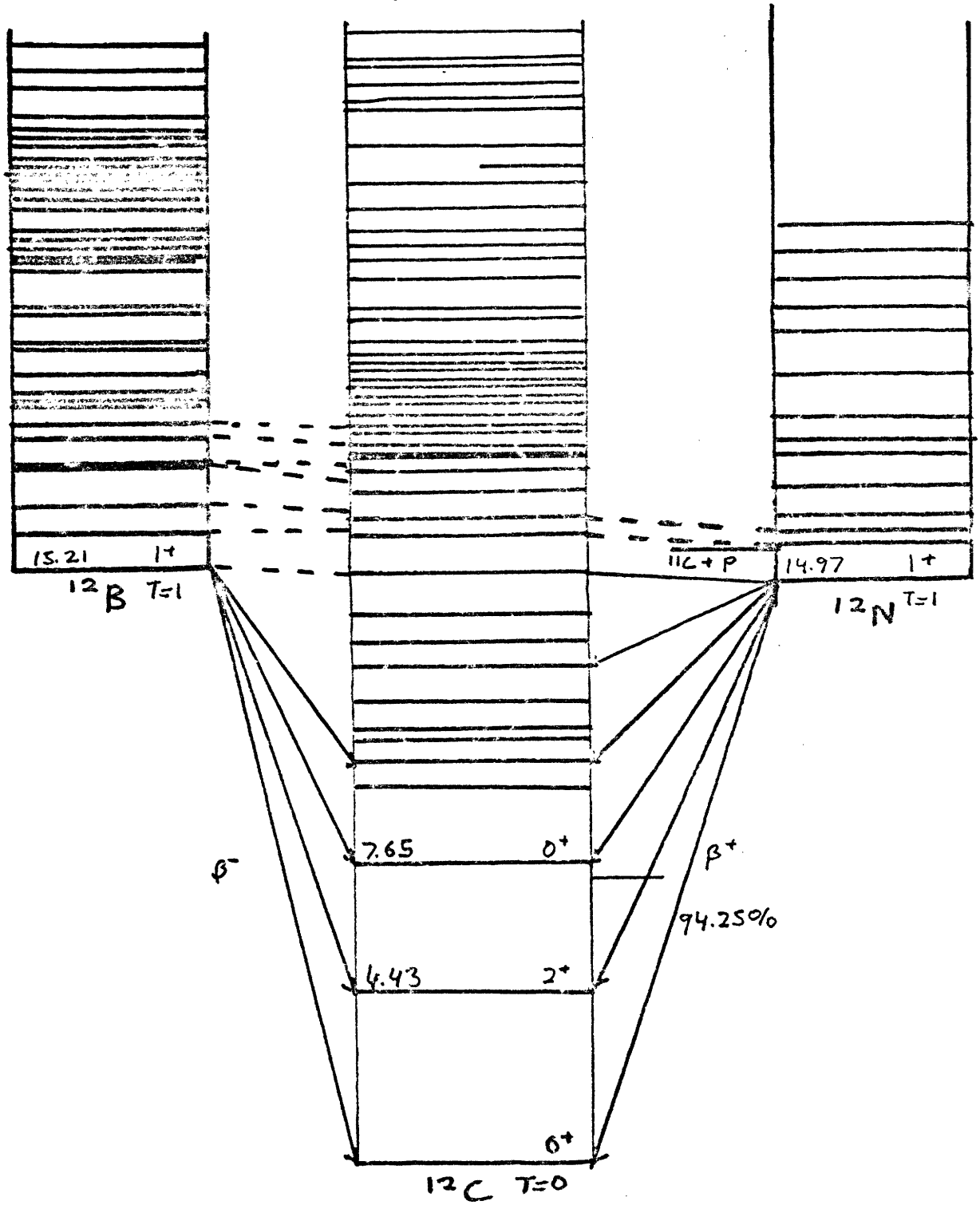

yield in the delta region, the relative contribution to the $^{12}C(\gamma,\pi^-)^{12}N$ yield is less than 5% at 50 MeV above the pion threshold. This means that systematic errors arising from the extrapolation of the two-step background will be minimized.

The third reason is the readily identifiable decay product of ^{12}N, which can than be used to determine how many ^{12}N nuclei were produced by the photopion reaction. This is a 16.34 MeV endpoint energy positron with a branching ratio of 94.25% and a half-life of 10.97 msec. (AJ75). The high endpoint energy facilitates separation from other, undesired, particles, and the lifetime is short enough that the decays can be detected between the beam bursts of the accelerator, yet long enough that background from neutron capture gamma rays has had time to die down. The principal backgrounds that then remain are from the positron decays of ^{12}B and ^{9}C,. Since their half-lives are much longer than for ^{12}N (774 msec and 127 msec respectively), they can be separated out on this basis. In a later section other methods used to reduce their contribution will be examined.

One last experimental advantage of carbon is the ease with which a target can be constructed. Due to the high melting point for this element, it is possible to allow an electron beam to pass directly through the target and thus measure both the photoproduction reaction $^{12}C(\gamma,\pi^-)$ and the electroproduction cross section $^{12}C(e,e'\pi^-)$ by placing suit-

able radiators in front of the target.

B. Theoretical Motivation

From the point of view of performing accurate calculations, the large body of static and dynamic information on carbon is useful in calibrating the nuclear structure and pion distorted wave inputs . The availability of high quality elastic pion scattering data is illustrated in Fig. I-6. This data provides some constraints on the optical potential parameters that can be used, but does not uniquely determine them. The same is true in the threshold region, where the pionic atom information can be used (BA78). Some information of the isovector part of the optical potential can be had from the recent comparisons of pion scattering from ^{12}C and ^{13}C of Dytman et al (DY78).

Recent measurements of the magnetic electron scattering to the 15.11 MeV level in carbon, which is the isobaric analog state to the ground state of ^{12}N (see Fig. II-1), have been useful in extracting the transition densities needed for the photopion calculations (DU78, FL79). A compilation of the data is shown in Fig. II-2, along with the phenomonological fit of Haxton (HA78). Notice the deep mininum at about 1.3 fm^{-1}. This strong falloff of the form factor will make the total cross sections dominated by the production at forward angles, where the momentum transfer is close to the pion mass of .71 fm^{-1}.

These constraints on the nuclear structure and pion

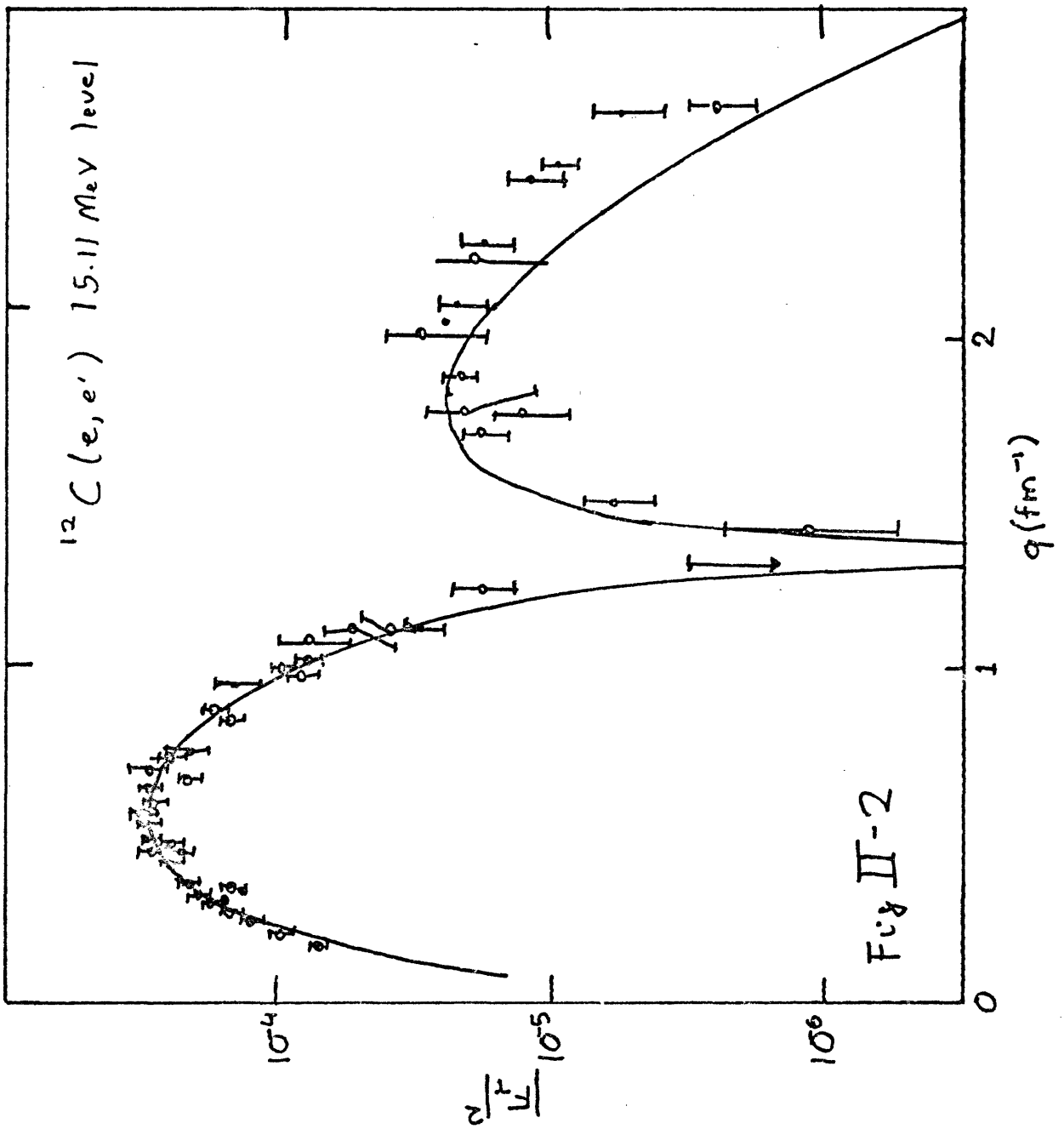

Fig II-2

distorted wave inputs make the $^{12}C(\gamma,\pi^-)$ reaction a good test case to study the validity of the impluse approximation in the delta energy region.

This summarizes the motivations for performing this experiment. The previously existing experimental data will now be reviewed, with emphasis placed on what has been learned from them and what improvements would be necessary to obtain new information.

II-2 Previous Experimental Results

Two previously existing experimental results have been obtained, one in the near threshold region (from 0 to 12 MeV above threshold) at the Bates Linac (BE76), the other in the delta region (from 0 to 200 MeV energy pions) at the Tomsk synchrotron in the USSR (EP74).

A. Threshold Region

The threshold experiment was performed by a Boston University / MIT collaboration in 1975. The yield points were obatained by detecting the residual radioactivity from ^{12}N with a small magnetic spectrometer. The half-life information was used to separate the signal from various backgrounds. The absolute normalization was obtained by measuring all points relative to the smoothly varying yield from $^{14}N(\gamma,2n)^{12}N$ and then measuring this monitor reaction absolutely in a separate experiment. This was found to be very useful in eliminating systematic errors. A complete description of the experiment is given in the thesis of N.

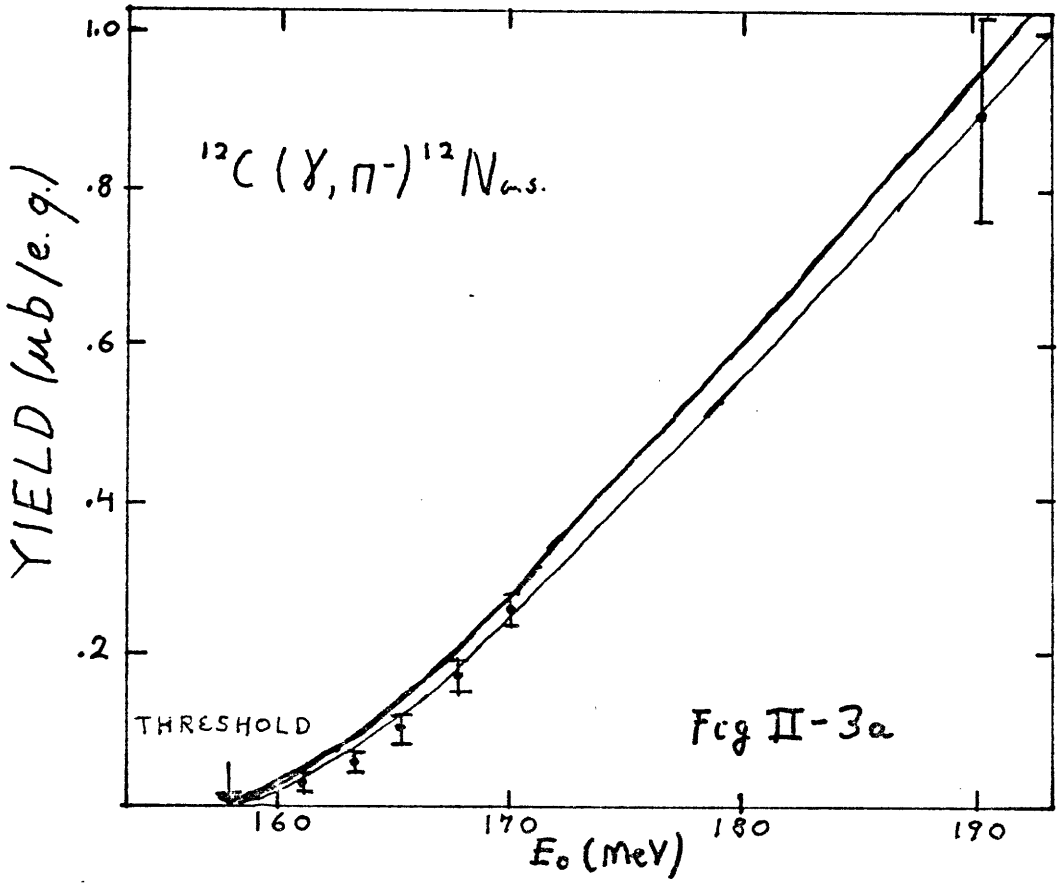

Fig II-3a

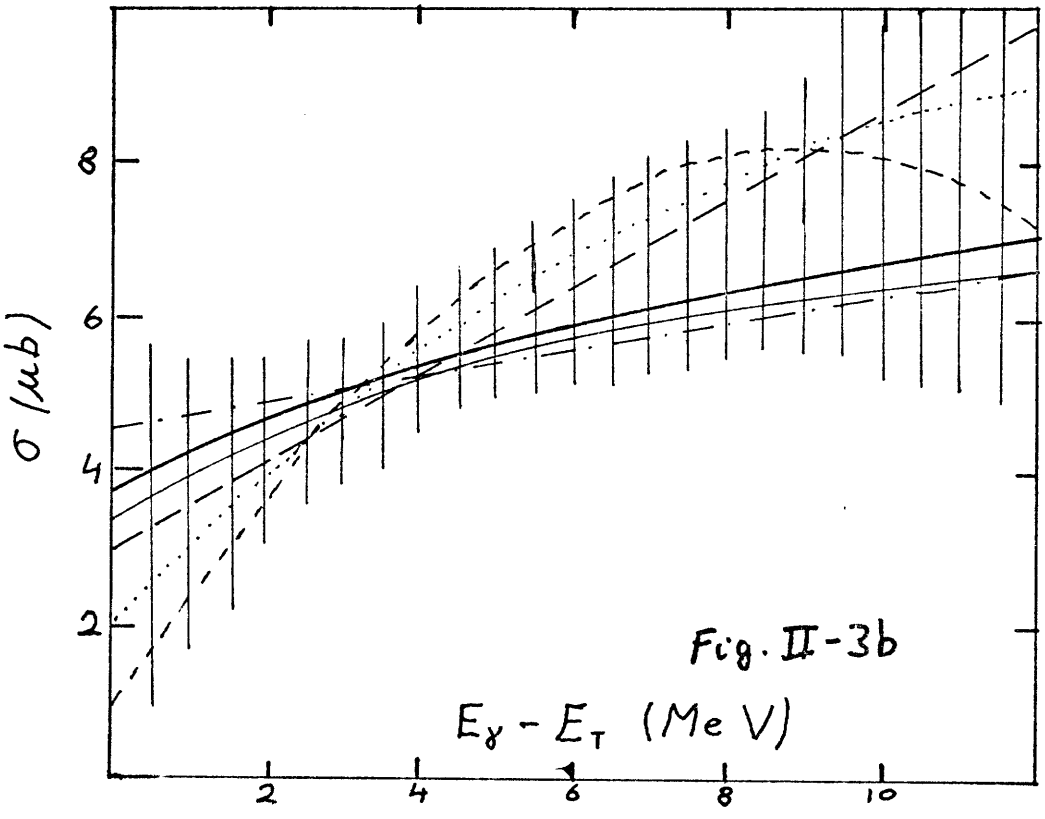

Fig. II-3b

Paras (PA79). Much of the experience gained in setting up this comparatively difficult experiment was extremely valuable in planning to extend the measurements to higher energies.

The results from this experiment are shown in Fig. II-3. The upper plot shows the yield points (see EQ. I-14) as a function of maximum photon energy after the two-step background from $^{12}C(\gamma,p)$ followed by $^{11}C(p,n)$ has been subtracted. The solid lines have been obtained by folding the theoretical cross sections of Nagl et al (NA79) (thin line) and Epstein et al (EP78) (heavy line) with the bremsstrahlung flux corresponding to the appropriate incident electron energies. It can be seen that the agreement is very good, but it is perhaps more revealing to compare directly to the cross sections deduced from the experimental yields.

This is exactly what was done to obtain the results shown in the lower half of the figure. The unfolding was done using the methods described in Appendix 1 with both a linear form and a parabolic form for the cross section assumed. Fits were made both with and without the yield point at 190 MeV, and the cross hatched area encloses the results of all these different paramatrizations. Notice the constraining power of the 190 MeV point in moderating the deduced slope of the cross section. This illustrates a more general feature: to obtain accurate cross sections at a given energy it is necessary to measure yield points at much

higher energies.

As in the graph of the yield curves, the thick and thin solid lines correspond to the calculations of NA79 and EP78. The good agreement with experiment marks a success for the impulse approximation in the threshold region to the twenty percent level. Earlier calculations which did not include momentum dependent terms in the elementary operator or a sufficient number of partial waves in the expansion of the pion distorted waves were found to be too small compared to experiment, but no major problems are found to remain when these effects are treated correctly. This is in spite of the fact that the Coulomb attraction pulls in the pion wave function very strongly compared to (γ,π^+) reactions, where the results of several experiments in the threshold region are also found to be in good agreement with DWIA calculations. (BO79)

B. Resonance Region

The previously existing data for $^{12}C(\gamma,\pi^-)$ in the delta region was measured in 1973 by Epaniskolov et al in the U.S.S.R. Their published yield points and deduced cross sections are shown as the solid points in Fig. II-4. For comparison, their yield curve was unfolded using the methods described in Appendix 1 to obtain the envelope enclosed by the cross hatched area. It can be seen that the two methods of unfolding the yields are basically compatible, but are in sharp disagreement with the calculations of NA79 and EP78,

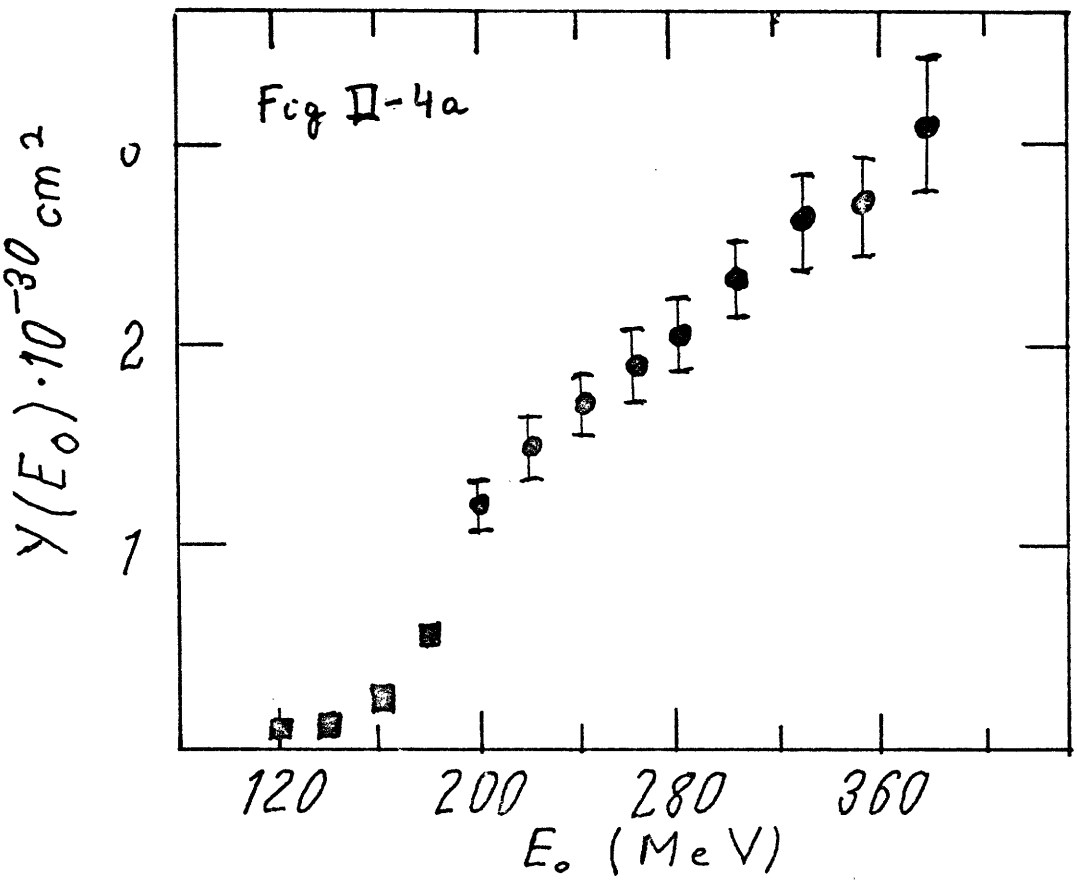
Fig II-4a
$Y(E_0)\cdot 10^{-30}$ cm^2
0
1
2
120
200
280
360
E_0 (MeV)

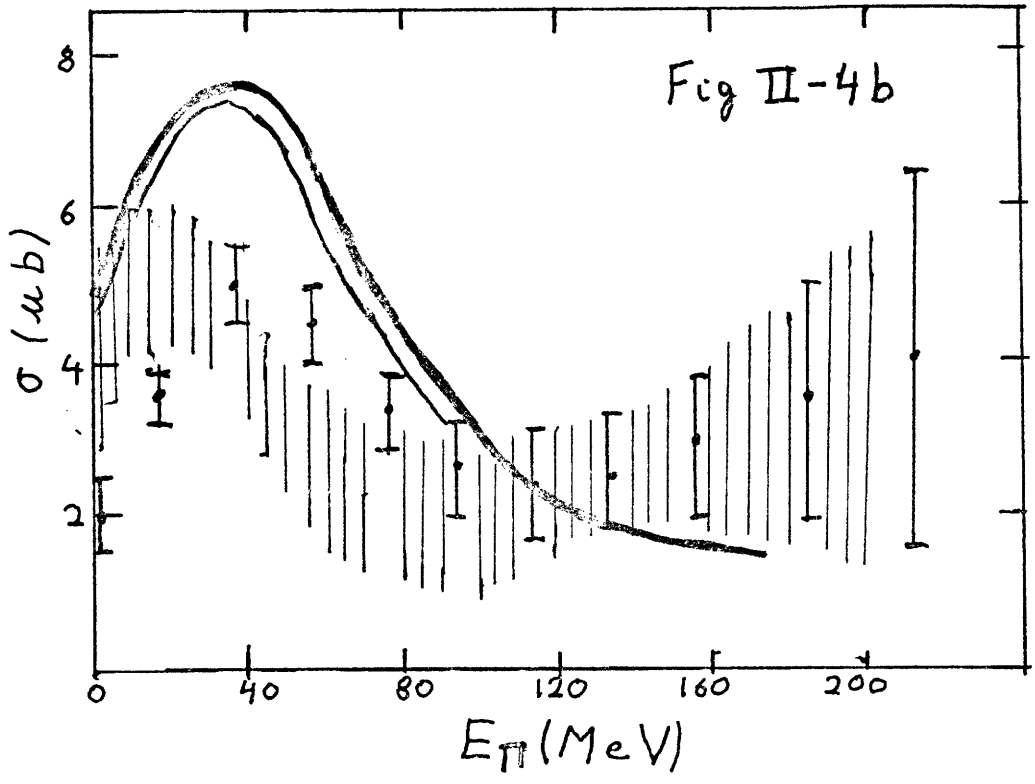
Fig II-4b
σ (μb)
2
4
6
8
0
40
80
120
160
200
E_π (MeV)

shown as the thin and thick solid lines, particularly in describing the shape and magnitude of the peak at approximately 50 MeV above the pion threshold.

There are several reasons to suspect that the problem may have been with the data rather than with the calculations. The first is that they did not use a magnetic spectrometer to separate electrons and positrons, but relied on the half-life information to extract the ^{12}N contribution using a plastic scintillator. Although some checks were made by measuring the annihilation gamma rays from the stopped positrons with a NaI detector, a calculation was still required to evaluate the energy dependent efficiency of their detection system. Another problem with their data was that no attempt was made to evaluate the contribution from the two-step background. The greatest problem with making a precise comparison with calculations was the large spacing and relatively large error bars on the yield points, making it necessary to use a large smoothing factor in extracting the cross section. This may be the principal reason for which the peak at 50 MeV is underestimated.

In order to make a more precise test of the DWIA calculations of total cross sections in the 0 to 140 MeV range of energy above threshold, it was decided to repeat the Epaniskolov experiment with the following improvements: more closely spaced yield points with much smaller error bars, a magnetic element to eliminate competition from electron de-

cays from ^{12}B (which has a half life of 20 msec, very close to that for ^{12}N), careful measurement of the two-step background, and finally careful control on the absolute normalization. The following sections describe the manner in which all of these goals were achieved.

II.3 Experimental Setup

This section describes the physical layout of the apparatus that was used to perform the experiment. Details concerning the types of detectors that were used, target construction, electronics, and data aquisition are given, as well as some of the procedure used to optimize the detection efficiency.

A. Physical Layout

The previous experience gained in the threshold experiment was useful in planning to extend the measurements to higher energies. Especially important would be shielding the detectors from random background events arising principally from pair production from neutron capture gamma rays. Another important aspect would be having a magnetic element to separate the 16.4 MeV endpoint positrons from the sea of other particles coming from the target. The pion spectrometer fixed at 90° in the 14° area of the Bates Linear Accelerator, was a device already in place that satisfied both of these requirements. Fig. II-5 shows the layout of the device. Heavy iron blocks shielded a magnet followed by a wire chamber and three 1.58 mm thick plastic scintillators. The

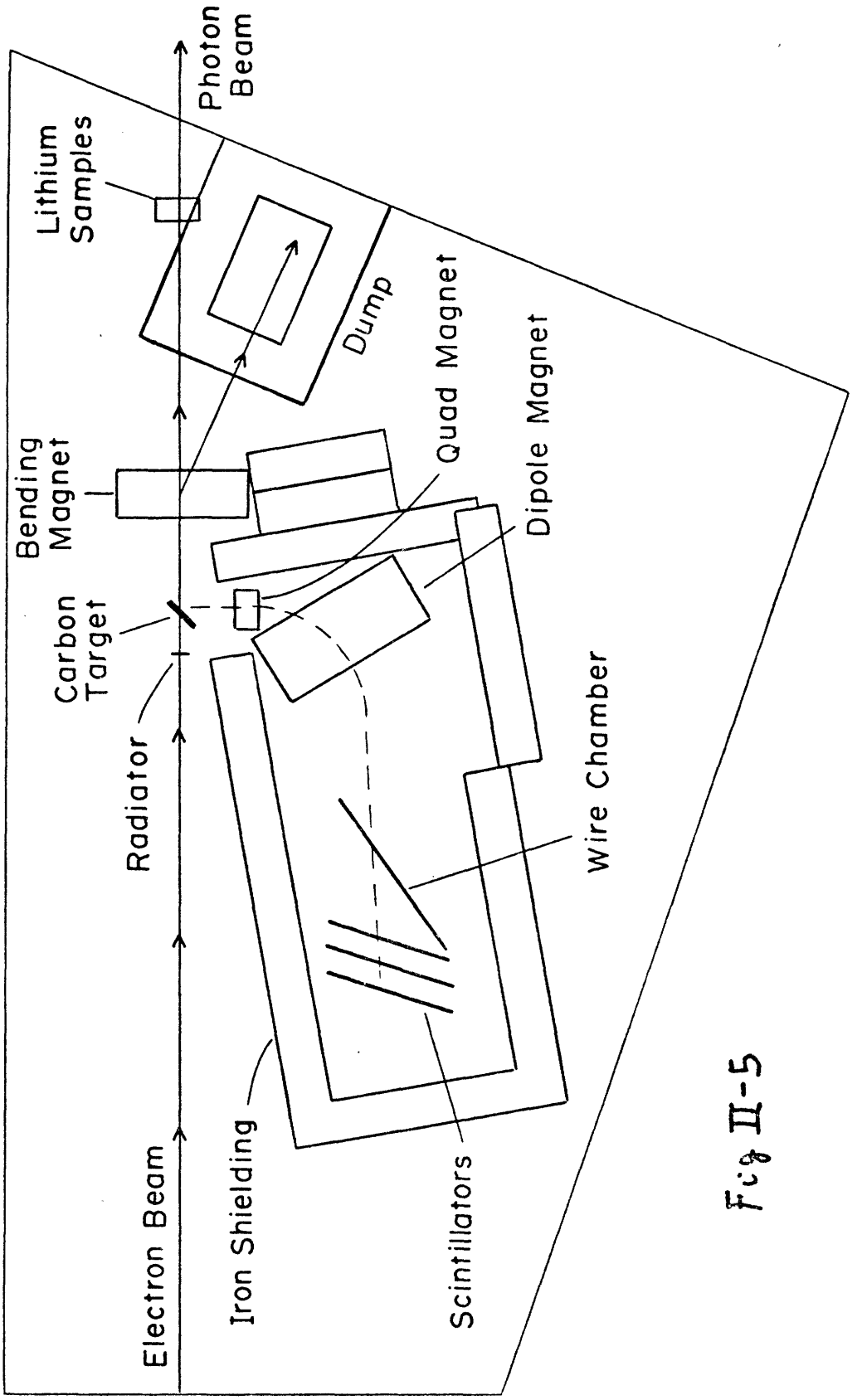
Photon Beam
Lithium Samples
Dump
Quad Magnet
Dipole Magnet
Bending Magnet
Carbon Target
Radiator
Wire Chamber
Electron Beam
Iron Shielding
Scintillators

Fig II-5

electron beam passed through the target chamber before being dumped into a graphite block two meters away. A remotely controlled ladder placed 10 cm in front of the target made it possible to run both with and without Ta radiators of various thicknesses.

The close proximity of the dump made for a larger background than is found in most experimental areas of this type. Three other disadvantages to using this set-up were: a) the small solid angle of 15.1 msr, b) the small momentum acceptance of 14%, and c) the fact that the wire chamber had been designed to be most efficient for 20 to 40 MeV pions and had an efficiency of only 30% to 50% for detecting electrons.

In spite of these limitations, count rate calculations showed that several hundred counts per hour could be expected with the repetition rate set at 15 Hz, 12 μsec long pulses and 10mA peak current. From the threshold experiment, large amounts of long-lived high endpoint energy positron decays from ^{8}B and ^{9}C were expected. In order to partially alleviate this problem, a rotating target was built. A 6.35 cm diameter and 3.05 mm thick carbon disc with a gear mounted around its circumferance was rotated by a motor past an 8 mm slit at one revolution per second. A drawing is shown in Fig. II-6. The beam was positioned near the edge of the target, so that the active area moved about 4 mm during each 40 msec counting period after every

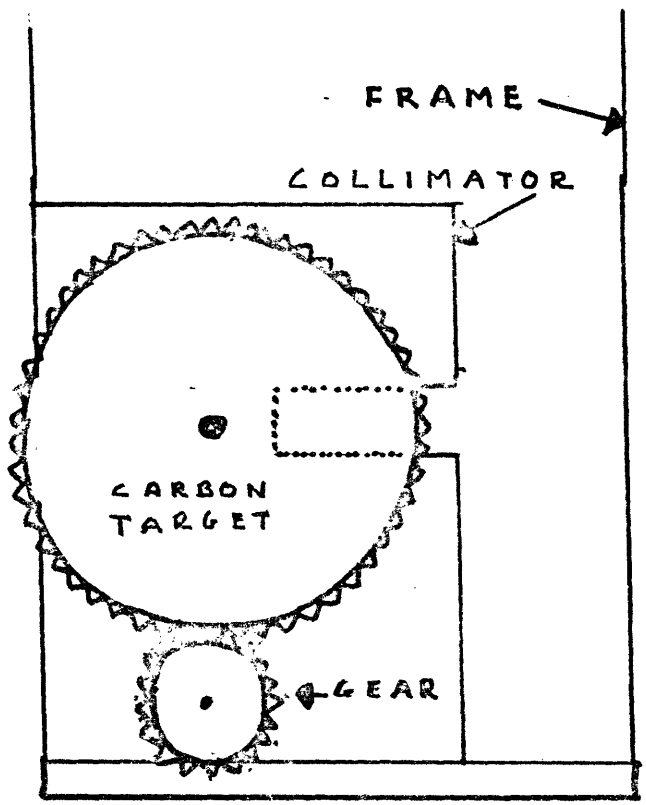

Fig II-6

beam burst. The rotating target reduced the amount of 127 msec activity by a factor of 2.93 and the amount of 770 msec activity by a factor of 15.3 when the beam was pulsed at 15Hz. The target assembly was mounted at 45° to minimize the energy losses of both the incident electron and the beta decay positrons. It was mounted on a remotely controlled actuator so that target out runs could also be taken.

The last important detail concerning the functioning of the physical apparatus was the setting of the magnetic field. Tests were made to determine the field setting that would give the greatest number of 16.4 MeV endpoint positrons, and the value found was that corresponding to a momentum of 9.2 MeV/c.

B. Electronics

The electronics for this experiment are shown in Fig. II-7. The three scintillators were each divided into two halves, right and left. The pulses from each set of three passed through discriminators and delay boxes and were then placed in coincidence. A pulse was sent to a memory buffer to remember which side fired, then the coincidences from right and left were "or"ed together to provide the master trigger signal. A bin gate which comes on 3.5 msec after the beam burst and lasts for 40 msec prevented triggers from occuring outside its range. The trigger opened the gates to the CAMAC TDCs and ADCs , which were computer readable time-to-digital and analog-to-digital converters, in order to re-

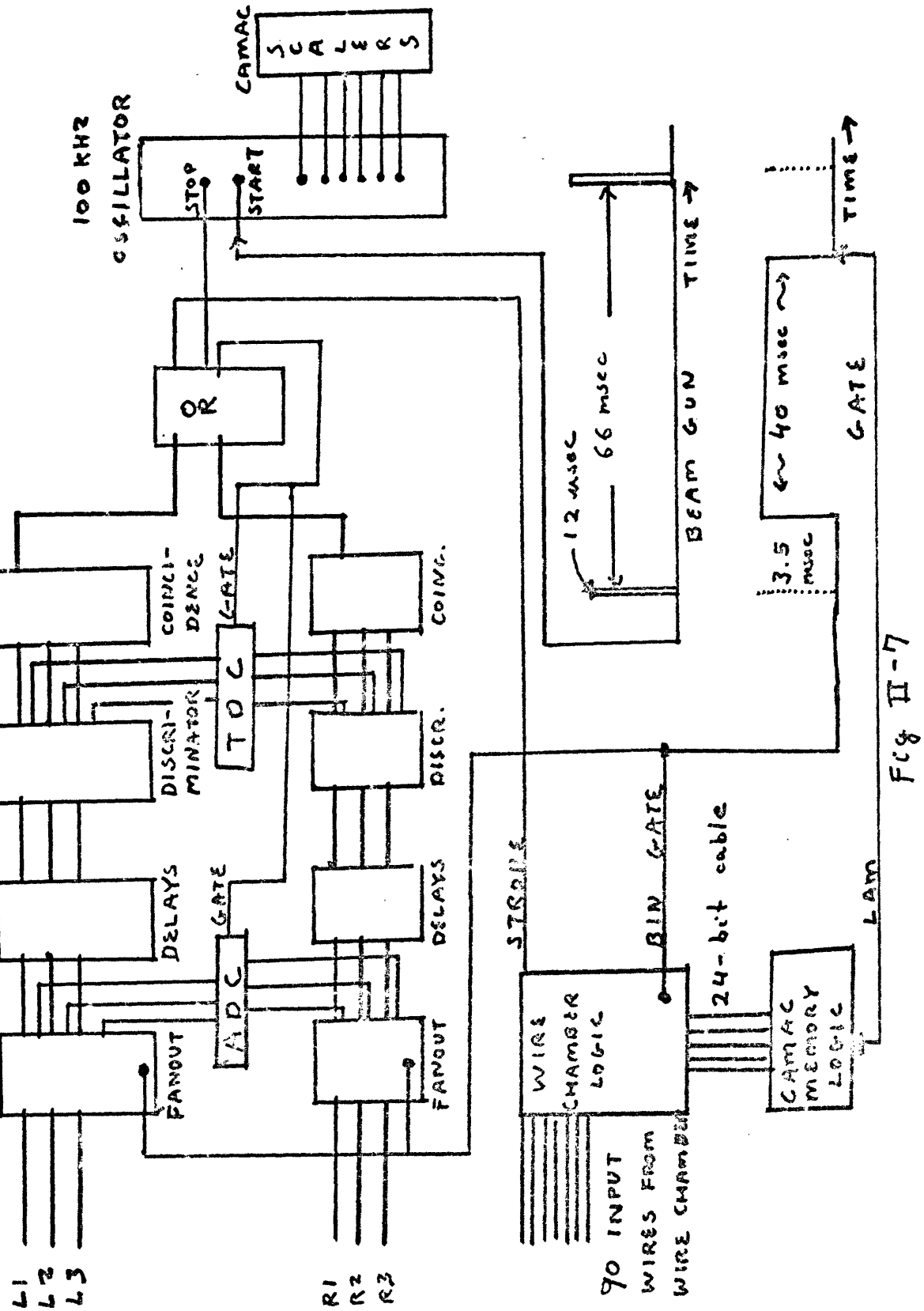
100 KHz
OSCILLATOR
CAMAC
SCALERS
STOP
START
OR
COINCI-
DENCE
GATE
TDC
DISCRI-
MINATOR
DELAYS
GATE
ADC
FANOUT
COINC.
DISCR.
DELAYS
FANOUT
L1
L2
L3
R1
R2
R3
12 msec
66 msec
BEAM GUN
TIME
~40 msec
GATE
TIME
3.5 msec
STROBE
BIN GATE
24-bit cable
WIRE CHAMBER LOGIC
70 INPUT WIRES FROM WIRE CHAMBER
CAMAC MEMORY LOGIC
LAM

Fig II-7

cord the pulse heights and relative timing for each of the six scintillators for the first event after each burst. The trigger also had the wire chamber logic look for channels that had triggered. Since the electrons pass through the chamber at roughly 60^{o}, they generally triggered two or three adjacent channels, so the logic only looked for events of this type in order to reduce the amount of random background. The trigger also stopped a 100 MHz pulser which had been started by the beam burst and whose output was fed into a computer readable scaler in order to tell how long after the beam burst the event occured. Both the wire chamber logic and the timing scalers could multiplex up to five events per counting period between beam bursts. The average number of events per beam burst was approximately one.

C. Data Aquisition

As soon as the bin gate was over, the wire chamber information, along with the right or left side information, was strobed into a computer readable memory buffer unit and the information was sorted by the computer code. For each event, the code first checked that an event had been found in the wire chamber channels. This only happened about one out of five times as often the triggers were caused by randomly oriented events that didn't pass through the chamber or by particles that didn't pass through with the correct angle to trigger two or mare adjacent channels. If this test was passed, a multichannel scaling spectrum (mcs) of

the time distribution of the events after the beam burst was made. Separate spectra were made for the right and left sides as well as for the sum so that checks on the stability of the system could be made.

If the event was the first one in that counting bin, and the wire chamber test was passed, the pulse heights and relative timing information for the relevant scintillators were sorted into spectra. The CAMAC modules were then cleared and made ready for the next beam burst. Meanwhile, computer scalers also recorded the output of the two beam-monitoring toroids, the singles rates from each counter, the number of beam pulses, the number of triggers from each side and their sum, and the number of triggers actually processed by the wire chamber logic.

D. Optimization of Efficiency

The ADC and TDC spectra were useful for tuning the apparatus to run at maximum efficiency. Typical examples are shown in figure II-8. First, the discriminators were set at 50 mV and the widths of their outputs to 8 nsec. Then the high voltages were increased until the discriminators were no longer cutting into the electron peaks. Increasing the high voltages on the phototubes to the scintillators past this point only increased the accidental rate without affecting the number of true events. The wire chamber high voltage and timing relative to the triggers were adjusted for maximum efficiency as well.

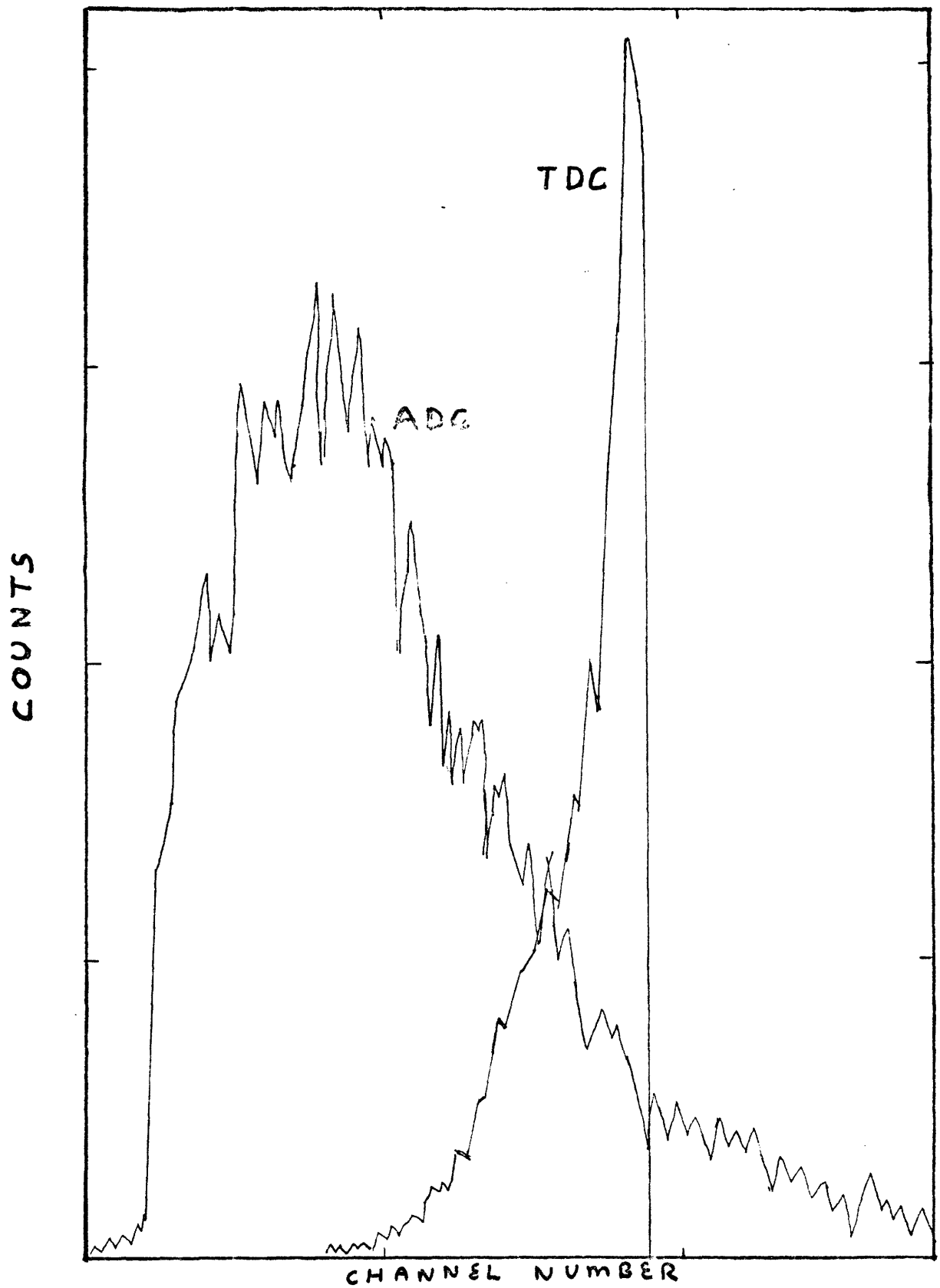

Fig II-8

The relative timing between the three scintillators on each side was then adjusted by matching the TDC spectra. If one counter is consistently coming late, the spectrum would be a spike with no singles in front of it, since it is always the last counter that determines the start pulse to the TDC's. If one counter is coming consistently earlier its peak will be considerably broadened and ragged looking due to the timing jitter. When the times are all correctly adjusted, each counter will have a narrow peak from the real coincidences plus a range of counts in front of it in time from singles which happen to occur in that counter just before the coincidence is made. This procedure of matching the time spectra so that each counter is equally likely to be the one that determined the coincidence time permits rapid tuning of the timing with an accuracy of .5 nsec.

It should be noted that the resolving time for the trigger from the three plastic scintillators in coincidence was about 10 nsec. Since the counting period was between beam bursts, the singles rates were relatively low and accidental coincidences could be neglected. Thin sheets of aluminium placed between the counters helped to reduce the rate from very low energy background electrons.

II.4 Extraction of Relative Yields

This section describes the manner in which data was taken and the procedures used to obtain yields at each energy relative to a convenient monitor reaction, $^{13}C(\delta,p)^{12}B$.

A. Use of a Monitor Reaction

In order to minimize systematic fluctuations due to changes in detection efficiencies, the monitor reaction $^{13}C(\gamma,p)^{12}B$ was measured at the begining of each beam energy. This was done by using the natural 1.11% abundance of the carbon target and simply reversing the magnetic field to detect the 14.1 MeV endpoint energy 20 msec half-life beta decay of ^{12}B. Since the yield from this reaction is large and a slowly varying function of energy, it was well suited as a monitor. The yield from $^{12}C(\gamma,\pi^-)$ was then measured at each energy, both with and without the Ta radiators. Finally, at the end of each energy, the monitor reaction was remeasured to check the stability of the apparatus. Occasionally the radiators were used for the monitor reaction as well in order to separate the electroproduction and photoproduction relative contributions (see next section). In addition, target out runs were taken periodically in order to subtract the contributions of various residual backgrounds.

B. Use of Half-Life Information

The half-life information was very useful in removing unwanted backgrounds from the data. Figure II-9 shows a typical time spectrum for the ^{12}N 11-msec decay. The average of all target-out runs, normalized to the number of incident electrons in this run, has already been subtracted. Most of the target-out counts come from neutron capture

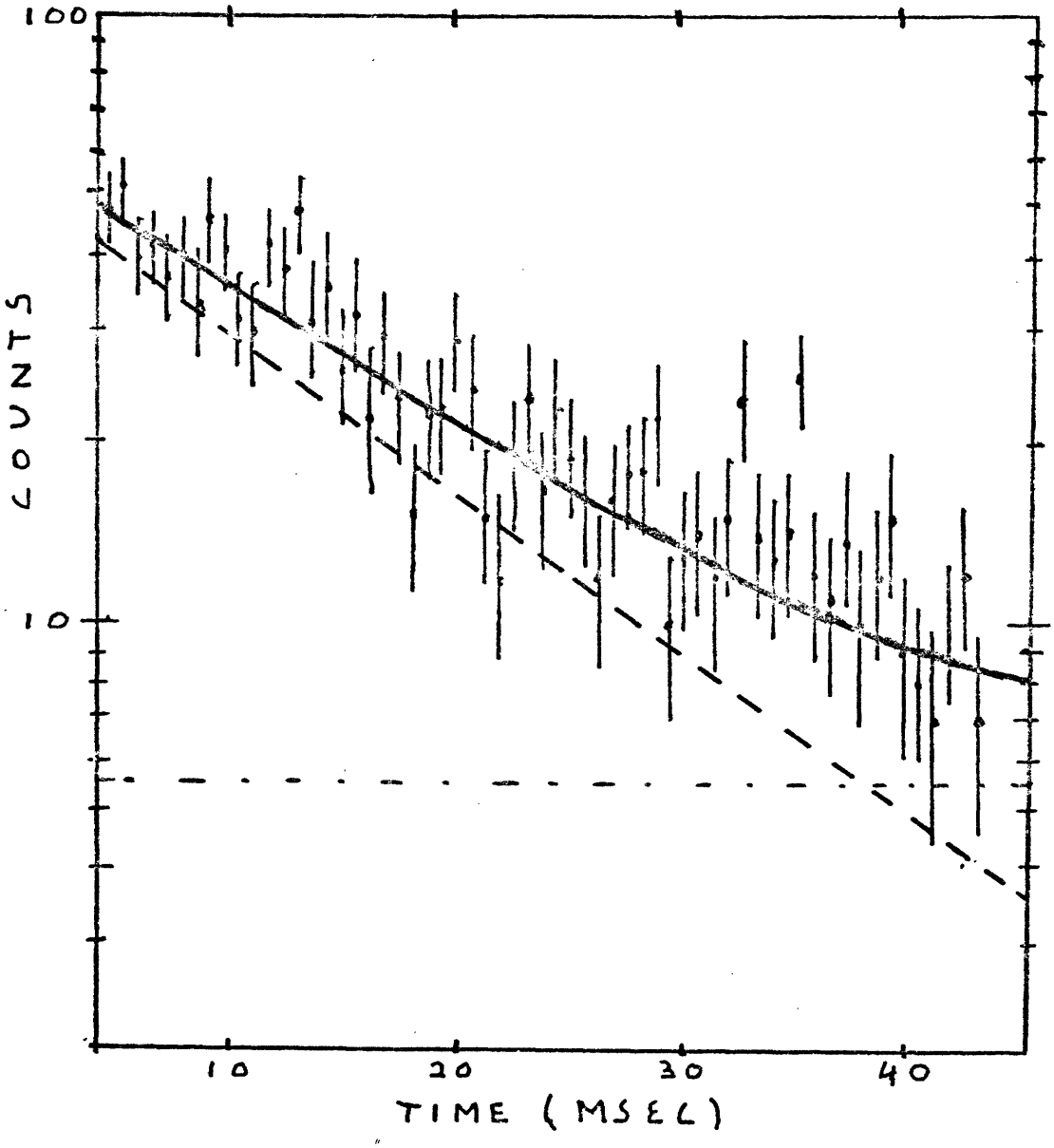

Fig II-9

gamma rays and seem to decay with an apparant half-life of 1.2 msec, leaving only a small residual flat background coming from cosmic rays. The background was thus comparable to the signal only in the first few milliseconds after each beam burst. The dead time due to more events arriving during a particular bin gate than could be handled by the electronic system was less than 1%. The spectrum was fit using the program CURFIT described by Bevington (BE69) with a function of the form

$$Y(t) = a + b\, e^{-t \ln 2 / t_o} \qquad \text{II.1}$$

where t_o is the half life (10.97 msec for ^{12}N and 20 msec for ^{12}B), and the variable a represents the flat background. The value of b gives the strength of the decay of half life t_o. The two components found to give the best fit in this typical spectrum are shown as the dashed lines in Fig. II-9, and the solid line represents their sum.

C. Relative Yields

The relative yield at a particular energy was found by taking the ratio of the 11 msec components from ^{12}N to the 20 msec components from ^{12}B and correcting for the relative number of incident electrons as measured by a toroid close to the target chamber. Dead time corrections were also applied, and were typically on the order of 10%.

A summary of the ratios thus obtained is presented in Table II-1 for the three major periods during which data were taken. Although the efficiency was known to have changed

A energy	B Nov 1st	C Nov 6th	D August	weighted average
120.			.016±52.%	.016±52.%
140.			.024 50.	.024 50.
160.			.051 15.	.051 15.
170.		.125±17.%	.104 8.0	.108 7.8
180.		.112 28.	.150 9.4	.150 9.4
190.	.247±13.%	.214 9.8	.240 5.8	.234 5.8
200.		.359 8.4	.310 6.1	.326 5.2
210.		.396 8.4	.441 4.3	.424 4.3
220.	.436 6.6	.446 7.2	.428 6.4	.436 4.0
230.		.487 8.4	.529 4.3	.521 4.3
240.	.450 6.2	.574 10.		.512 6.2
250.	.582 6.7	.612 6.2	.678 4.8	.624 3.3
260.	.598 4.9	.608 7.8	.590 5.8	.598 3.7
270.	.705 6.2		.592 4.9	.637 4.0
280.	.562 5.7	.549 5.8		.556 4.1
290.	.616 7.0			.616 7.0
300.	.618 4.5			.618 4.5
310.	.708 4.2	.650 6.0		.685 5.0
320.	.642 4.5			.642 4.5
330.	.656 6.1			.656 6.1
340.	.692 4.8	.681 7.2		.687 4.3
350.	.700 5.8			.700 5.8
360.	.629 5.5			.629 5.8

Table II-1. Ratios of yields from $^{12}C(\gamma,\pi^-)^{12}N$ with .184 mg/cm^2 radiator to those from $^{13}C(\gamma,p)^{12}B$ with no radiator. The errors are in percent.

from running period to running period and even during some of the running periods, it can be seen that by forming the ratios to the monitor reaction the data from the different runs are in good agreement with each other when points taken at the same energies are compared.

The ratios shown in Table II-1 are for the case of the .184 mg/cm^2 Ta radiator used for the $^{12}C(\gamma,\pi^-)$ reaction and no radiator used for the monitor reaction. Similar sets of ratios were formed for the cases when no radiator was used for the photopion reaction and when the thicker .324 mg/cm^2 Ta radiator was used. Since the electron beam always passed through the target, this information was essential in finding the relative contributions from electroproduction and photoproduction. The exact manner in which this was done is described in the next section.

II-5 Real-to-Virtual Ratios

In this section the manner in which the relative contributions of $^{12}C(\gamma,\pi^-)$ and $^{12}C(e,e'\pi^-)$ are extracted from the data is described and the results are compared to a simple model and to the results found from other total cross section measurements in the delta region.

A. Definition of Real-to Virtual Ratio

The definition of the real-to-virtual ratio is illustrated in Fig. II-10a. The three data points shown are the relative yields when no radiator, a .184 mg/cm^2, and a .324 mg/cm^2 Ta radiator respectively were placed in front of the

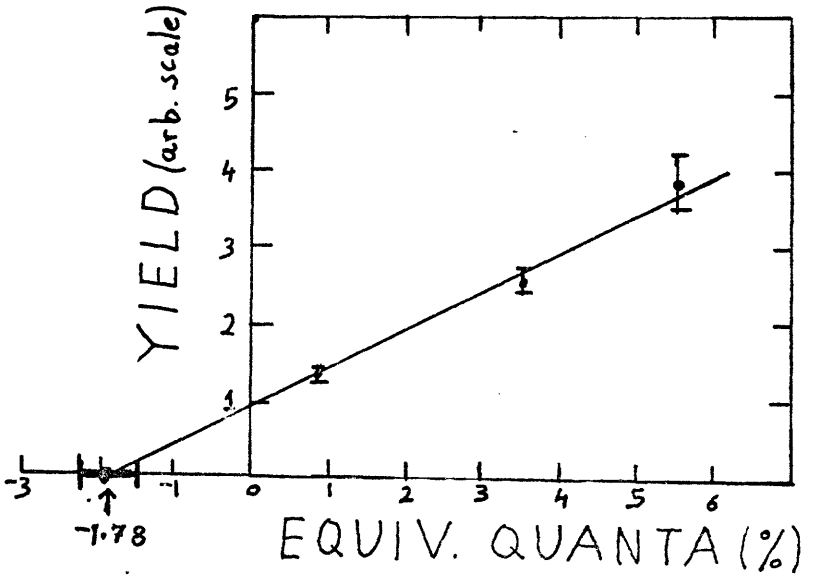

Fig II-10a

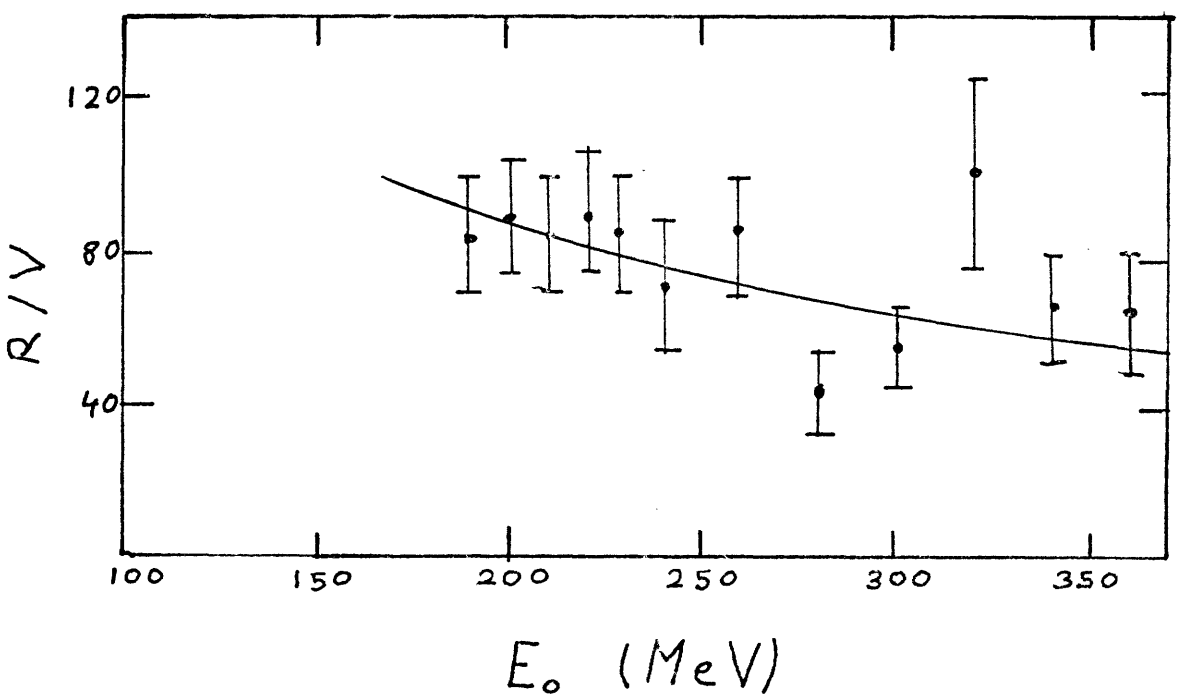

Fig II-10b

target. The number of equivalent quanta for each situation is a measure of the number of photons produced by each radiator and is closely related to the corresponding radiation lengths. The exact definition is given by

$$\text{II.2} \qquad e.q.(e_o) = e_o^{-1} \int_0^{e_o} \Phi(e_o, e)\, e\, de ,$$

where $\Phi(e_o,e)$ is the bremsstrahlung flux calculated from the formula of Bethe-Heitler as modified by Jabbur and Pratt (MA73). Notice that even with no Ta radiator the number of equivalent quanta is nonzero: the target itself acts as a radiator since some of the photons produced in the target can interact as they continue through.

It can be seen that the points lie on a straight line, as expected, since the yield should simply be proportional to the number of photons, but that the intercept is not zero. By extrapolating the line to intercept the horizontal axis, the effective number of equivalent quanta to which the virtual photons from the $^{12}C(e,e\pi^-)$ reaction correspond can be found. For purely historical reasons, the real to virtual ratio is defined as the inverse of this number expressed in percent. Thus, a real to virtual ratio of 50 would mean that the virtual photons have the same effect as a 2% equivalent quanta (or radiation length) radiator.

B. Results for $^{12}C(\gamma,\pi^-)^{12}N$

The definitions described in the last subsection were used to obtain the final results for $^{12}C(\gamma,\pi^-)^{12}N$ shown in Fig. II-10b. For several of the points, no run was taken

with the .324 mg/cm^2 Ta radiator, so they tend to have large error bars. Note that in general the error bars on the real-to-virtual ratios are larger than the errors on the individual points, since the real to virtual ratio is essentially an extrapolation. The solid line shows the result of a calculation using the E1 form of the virtual spectrum of Dalitz and Yennie (DA57). The M1 form gives a result about 3% uniformly lower. These forms of the spectra ignore nuclear size effects and use only plane waves for the incoming and outgoing electrons. Given that these aprroximations are only expected to be good to the 20% level, the agreement with experiment is surprisingly good.

In calculating the theorectical yields needed to make the extraction of the real-to-virtual ratio, a cross section for the $^{12}C(\gamma,\pi^-)^{12}N$ had to be assumed. Naturally, only the energy dependence is of importance, as the magnitude cancels out in forming the ratio. This being the case, the cross section calculated by Singham et al (see comparison with experimental results) was used, as its shape is very close to the one determined by this experiment. (SI79)

Since the prediction does a good job in describing the data, the DA57 spectrum was used to take all the data that was obtained and extract that part that corresponds to production from real photons. Thus, it should be understood that the results described in the next sections are in fact for pure photoproduction and thus can be compared directly

to the available calculations.

C. Comparison with Other Experiments

It is also possible to compare the present results with other experiments, in particular those from the total cross section measurements of $^{27}Al(\gamma,\pi^+)$ and $^{51}V(\gamma,\pi^+)$. (BL77) Their results for the real-to-virtual ratios are shown in Fig. II-11 , and it can be seen that the present results are quite similar to theirs. The two curves in each case come from the folding of the virtual spectrum with theoretical (γ,π) cross sections with and without final-state pion interactions (see Fig. I-7). It can be seen that although the cross sections used are very different, the real-to-virtual ratios are not strongly affected (see Chapter I for more discussion of these cases). Again the agreement with the Dalitz-Yennie predictions is surprisingly good.

II.6 Determination of Absolute Yield

In order to convert the ratios obtained in the last sections to a photopion yield curve, the results must be multiplied by a shape for the $^{13}C(\gamma,p)$ reaction. Once this is done, the absolute normalization is obtained by matching to the absolute yields measured previously in the threshold experiment (BE76).

A. Expected Shape for the $^{13}C(\gamma,p)$ Yield Curve.

The first question to be adressed is what would be expected for the shape of a (γ,p) yield curve. Below pion threshold the solution is easy, since the (γ,p) cross sec-

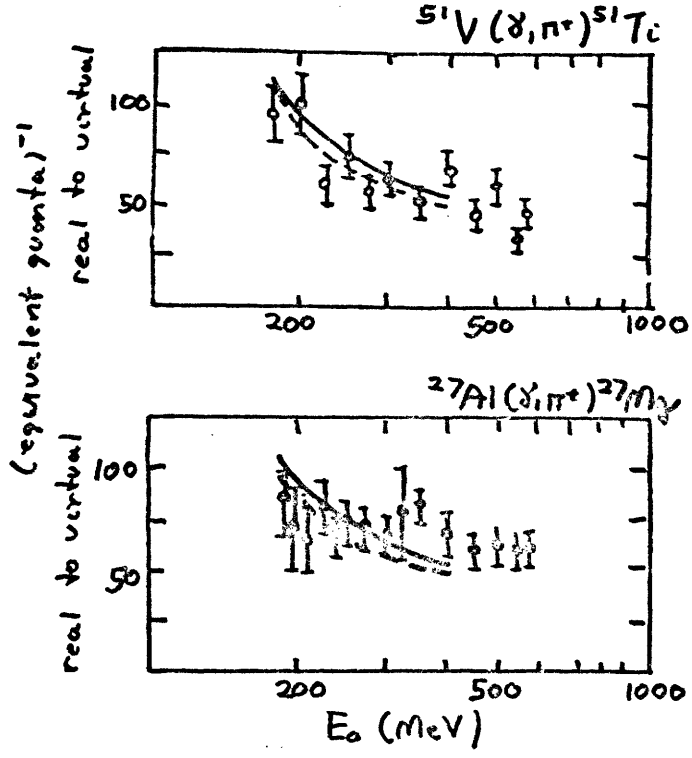
$^{51}V(\gamma,\pi^+)^{51}Ti$
$^{27}Al(\gamma,\pi^+)^{27}Mg$
(equivalent quanta)$^{-1}$
real to virtual
100
50
200
500
1000
E_0 (MeV)
NO FSI
WITH FSI

FIGURE II-11

tion has been measured at low energies (DE64). It is found to peak at around 30 MeV photon energy and falls off rapidly thereafter. Since the yield is only sensitive to the low energy photons, the results should become almost independent of energy above 100 MeV electrons. However, above pion threshold the (γ,pπ^0) and (γ,nπ^+) reactions will also contribute to give the same final state, so they must also be taken into account. Since these are quasi-free processes, they are expected to follow the shape of the total cross section from the free nucleon.

Both these features can be clearly seen in the data for the ^{12}C(γ,n) reaction of Hylthen (HY70). The dashed line is exactly the shape of the yield curve one would expect in the absence of pion production, and it can be seen that it gives a very good fit to the data below threshold. Above threshold, the solid curve is obtained when the yield curve from the free nucleon multiplied by an effective number of nucleons of approximately two is added in.

B. Extraction of Experimental Shape

The next question is how to combine together the data of different runs with different efficiencies to obtain a master experimental shape for the ^{13}C(γ,p) yield. Once this has been done, the results can be compared to what we would expect based on the arguments given in the previous paragraph.

All of the data points are plotted in Fig. II-12.

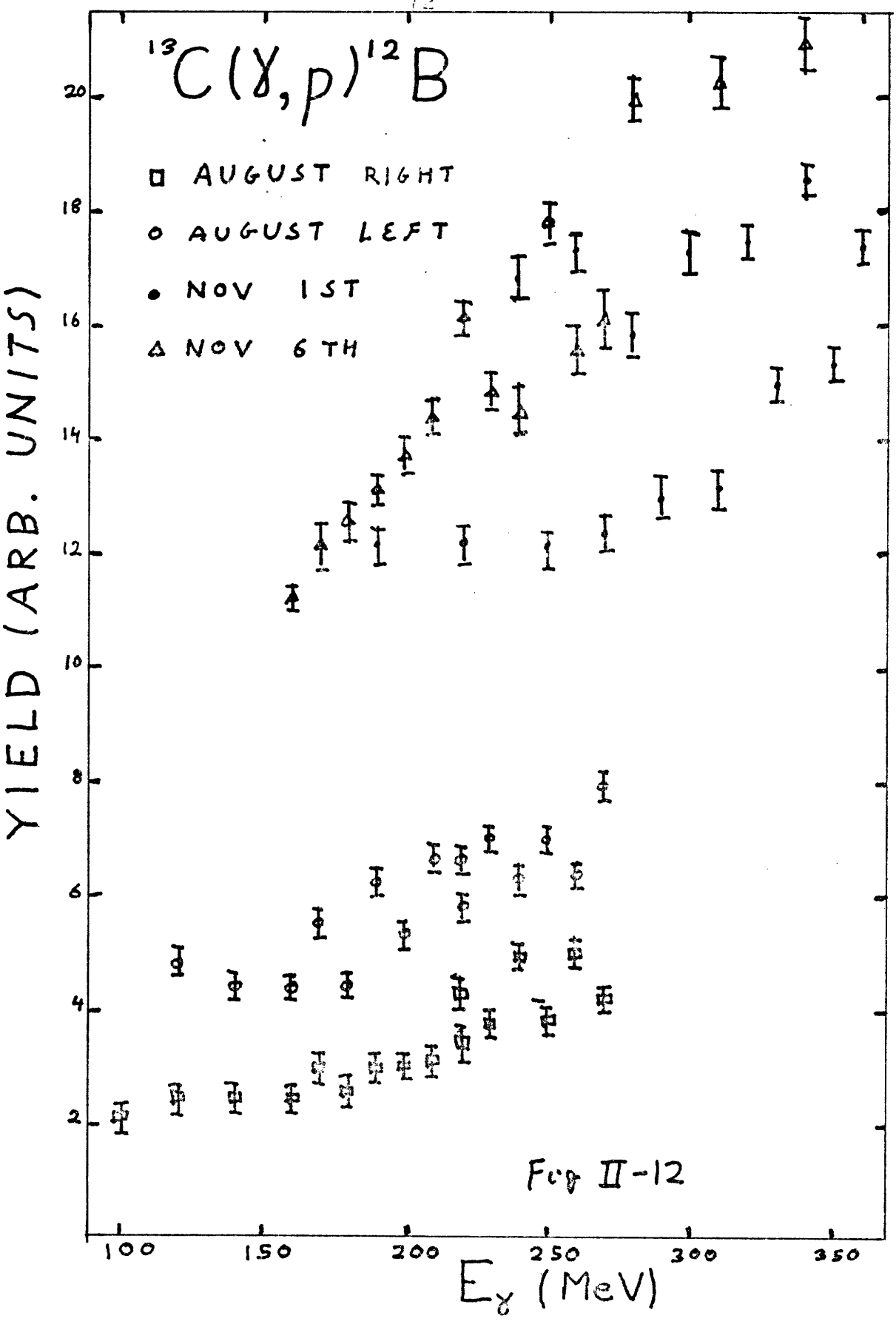
$^{13}C(\gamma,p)^{12}B$
AUGUST RIGHT
AUGUST LEFT
NOV 1ST
NOV 6TH
YIELD (ARB. UNITS)
E_γ (MeV)
2
4
6
8
10
12
14
16
18
20
100
150
200
250
300
350

Fig II-12

While at first sight the task looks difficult, in practice the job was not as hard as might have been guessed. In the August runs, the data for the left side taken at odd energies was higher than for the even energies due to a change in the tube base response for one of the scintillators. The first three runs taken on the right side (at 260, 240, and 220 MeV) are seen to be high due to a shift in an analog fanout level. If the data for August are divided into four groups based on these observations, the shapes are found to be in good agreement which each other. They were also found to be in good agreement with the shape of the yield curve obtained in the Nov 1st run. The points taken at the even energies during the Nov 6th run are also found to be consistent with the same yield curve as all the other groups, but the points taken at the odd energies present some difficulty. It would appear that the efficiency suddenly dropped and slowly regained its initial value. This can be correlated with the changing of the gas supply to the wire chamber. It was cold at first, causing a poorer response, but as the gas warmed up the efficiency was regained. Since the efficiency was changing, these points were not used in the analysis. The rest of the groups of data were fit together with one independent efficiency parameter for each group of data points. When this was done, the final shape for the yield curve shown in Fig. II-13a was obtained.

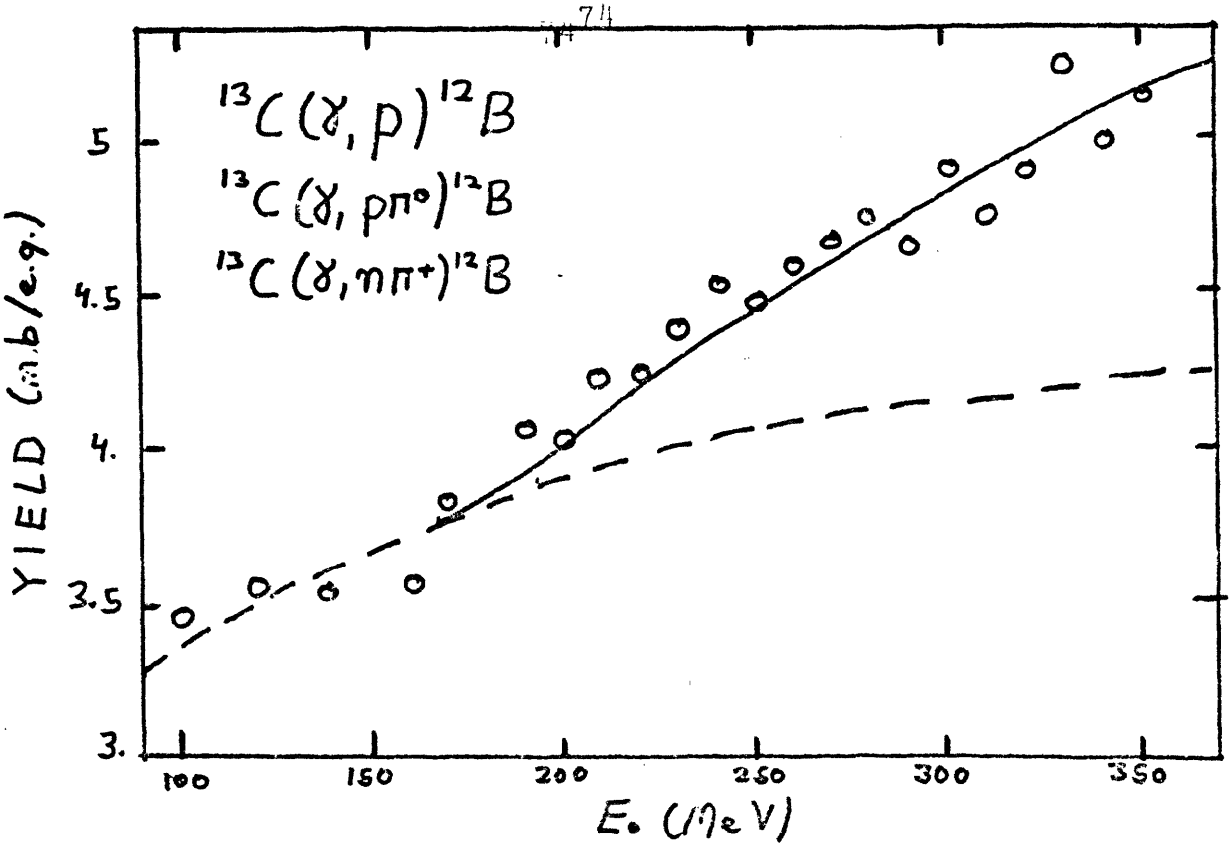

Fig II-13a

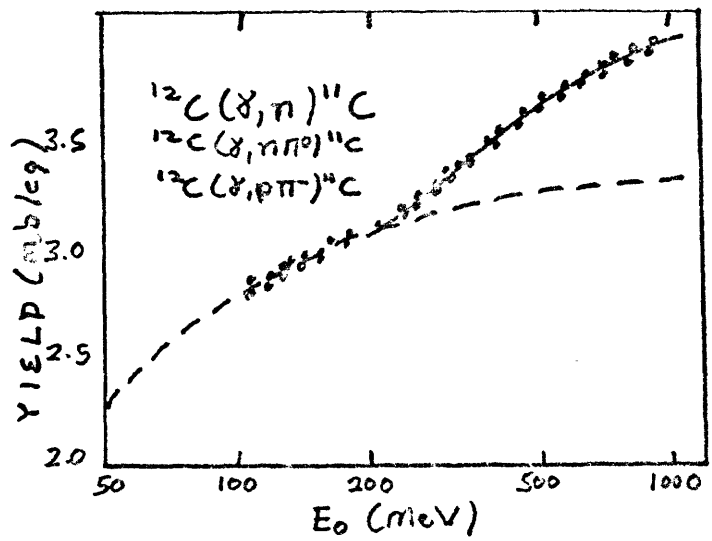

Fig II-13b

C. Comparison with Expected Shape

In order to compare the yield with the expected shapes, the results were first converted from electroproduction to photoproduction using the radiator in / radiator out information in the same manner as was done for the photopion yields. The technique used was the same as was described in a previous section. The absolute normalization was done by fitting the below pion threshold points to the yield curve calculated from the low energy data of DE64. It can be seen from the figure that the fit is quite good. Since the error bars on their data points are quite large, a large systematic error of 35% should be understood for the absolute normalization. Above threshold the yield is seen to increase significantly. The shape of the additional yield is found to be the same as that for the yield from the free nucleon, and the magnitude is that corresponding to an effective number of nucleons of approximately four. When the error bars on the absolute normalization are taken into account, this is consistent with the value found by Hylthen for a case in which the same numbers of participating nucleons are involved. Since the data follow the expected shape, a smooth line was fit through the electroproduction yields and used to multiply the photopion to (γ,p) yields that were derived in the previous sections.

D. Conversion to Absolute Yields

Once the shape of the photopion yield curve had been obtained as described in the previous subsection, all that

remained was to compare the yields at 170 and 190 MeV with those previously measured absolutely in the threshold experiment. Before this could be done, the contribution from the two-step background had to be subtracted. This was done by fitting a yield shape expected from a (γ,p) reaction to the below threshold points and extrapolating to higher energies. As can be seen in Fig. II-14, where the best fit is plotted as the dashed line, the correction is relatively minor. Once this was done, the final absolute yields shown in the figure were obtained. Not included in the error bars is an overall 14.5% normalization error. It can be seen that the results are considerably more precise than the previous measurement of EP74, and show a significant deviation from their results at higher energies. Furthermore, the present results are in good agreement with the calculations of NA79 and SI79 folded with the photon flux and shown as the dashed and solid lines respectively in the figure (the dotted curve is the result when only plane wave pions are used). More detailed comparisons will be made in the next section when the deduced cross section is compared to directly.

II.7 Final Cross Section for $^{12}C(\gamma,\pi^-)$ and Comparison with Theory.

In this section the method by which the yield curve was unfolded is described, after which comparison is made with the best available calculations. The implications of the results are discussed and suggestions for furthur improve-

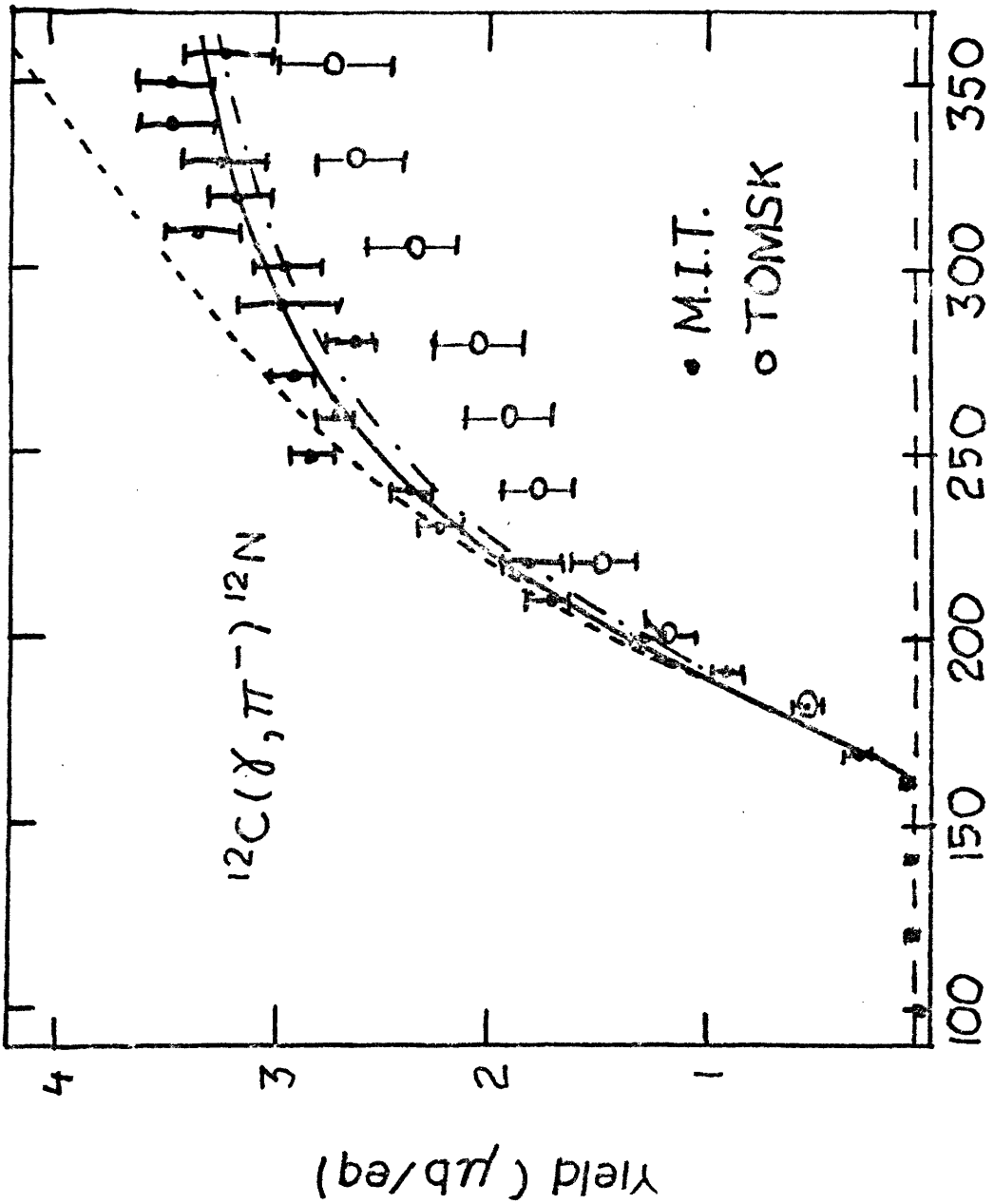
Yield (μb/eq)
4
3
2
1
100
150
200
250
300
350
E_0 (MeV)
$^{12}C(\gamma,\pi^-)^{12}N$
• M.I.T.
o TOMSK

Fig. II-14

ments are made.

A. Unfolding

Now that the yield curve has been obtained, the cross section can be determined using the methods explained in Appendix 1. The data obtained from the threshold experiment were included in the unfolding in order to have a better determination of the threshold behavior. The results for various paramatrizations of the cross section, either in terms of polynomials in powers of the energy above threshold or as a sum of equally spaced gaussians, are shown in Fig. II-15a. Only results for which the χ^2 per degree of freedom is reasonable (less than 1.3) are shown. The number of free parameters for the cases illustrated was between five and ten. It can be seen that the curves all lie within a zone which is about the same size as the error bars for the sixth degree polynomials, which are also shown in the figure. Therefore this zone was used as the final description of the cross section that had been obtained for $^{12}C(\gamma,\pi^-)^{12}N$ reaction.

B. Comparison with Theory

Comparison with theory is made in Fig. II-15b. The hatched zone encloses the results of the various parametrizations shown in Fig. II-15a. The solid line is the result of the calculation of Singham, Epstein, and Tabakin. (SI79) The dashed line shows their results when all except the Coulomb final state interactions are turned off. Two principal

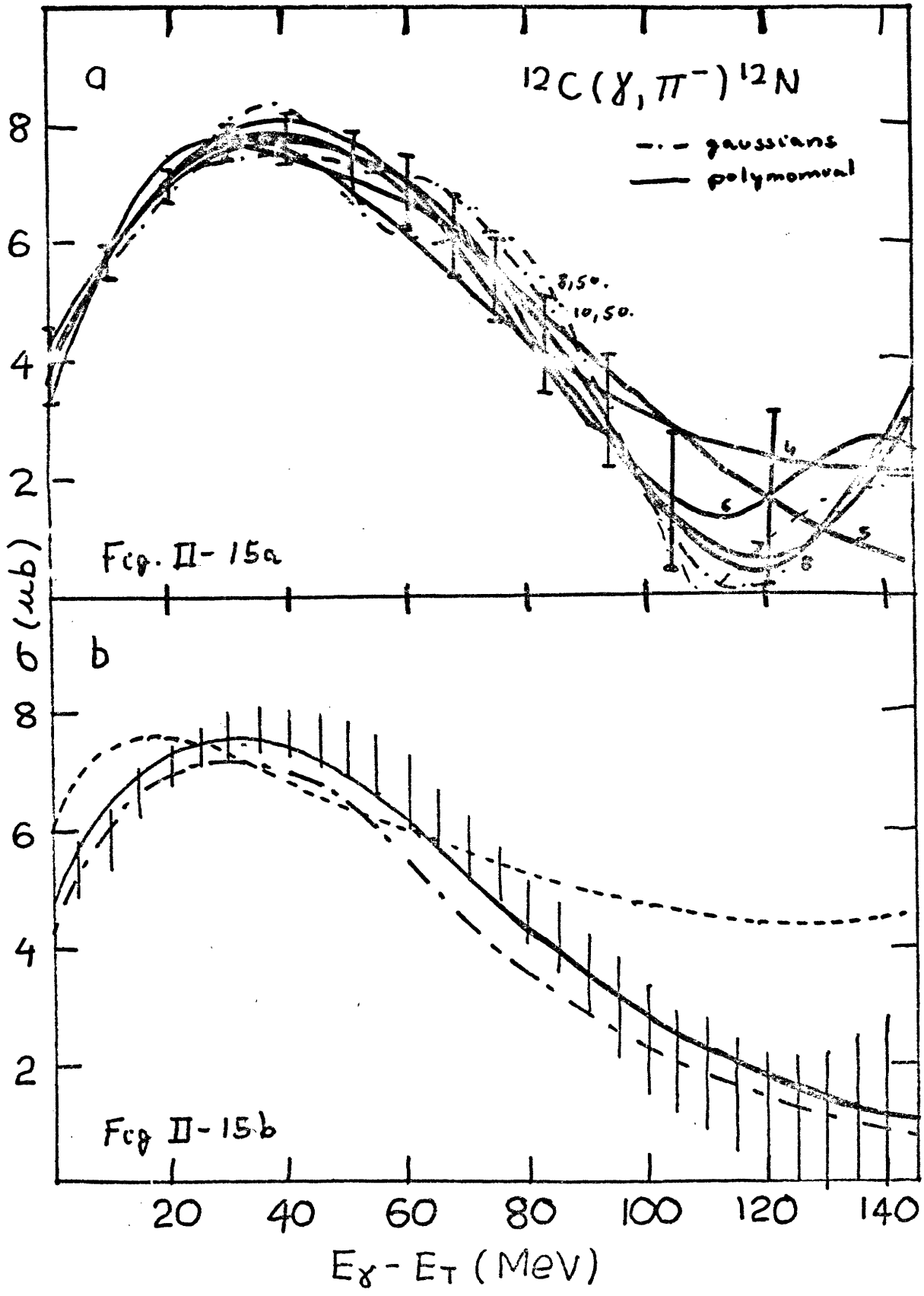
a
$^{12}C(\gamma,\pi^-)^{12}N$
gaussians
polymomial
8,50.
10,50.
Fig. II-15a
b
Fig II-15b
σ (μb)
8
6
4
2
20
40
60
80
100
120
140
$E_\gamma - E_T$ (MeV)

effects can immediately be noted. First, the decreasing overlap between initial and final states pulls the cross section down considerably with increasing energy from the shape of the free cross section (see Fig. I-3). Thus, instead of peaking at 150 MeV above threshold, the form factor for this specific transition forces the peak down to much lower energies. Turning on the strong final state interactions (the Coulomb potential only affects the cross section significantly in the first 20 MeV) then pulls down the cross section by as much as factor of three at 150 MeV due to the strong delta p-wave absorption.

Their method of calculation was discussed in some detail in Chapter I. They used the optical potential parameters of Stricker et al (ST79) with some slight adjustments to give better fits to the elastic pion scattering data currently available at 30, 40, 50, 116, and 180 MeV. Linear extraplolations of these empirically determined parameters were made between these energies. Due to their use of the coordinate space version of the Blomqvist-Laget elementary amplitude (BL77), their results should be treated with caution above 100 MeV, where this approximation begins to show significant deviations from the known elementrary multipoles.

The transition densities used were those shown in Fig. I-2. The choice of using the densities derived by Haxton (HA78), or O'Connell (OC72) made little difference to the

final result. This implies that this reaction is not sensitive to the second maximum in the form factor, where significant differences between the wave functions are noticed. It would be particularly interesting to investigate this kinematic region directly, by measuring differential cross sections, since the large increase in the form factor in the second maximum over that expected from shell model calculations may be due to critical opalescence, where pions are condensed within the nuclear medium.

Also shown, as the dot-dashed line, is the calculation of Nagl and Überall (Na79). They used the Berends amplitudes (BE71 and BE75) and similar optical potential parameters. For their nuclear wave functions they used the Helm model (UB72) to fit the M1 electron scattering data (DU78). In this model the derivitive densities are zero. Considering that substantially different approximations are made in the details of the two calculations (although the major approximations remain the same), the good agreement between the two lends confidence to the methods used in their derivation.

C. Summary and Conclusions

In summary, the experimental results for the $^{12}C(\gamma,\pi^-)^{12}N$ total cross section to the ground state of the residual nucleus are in remarkably good agreement with two independent DWIA calculations in the energy region from 0 to 140 MeV above pion threshold. As will be discussed in more

detail in Chapter Five, this is somewhat surprising since the impulse approximation has not worked well for the analogous pion charge exchange reactions, where nuclear medium effects are seen to be of great importance (AL79).

It should be very interesting to extend the present measurement to higher energies when the recirculator at the Bates Linac is completed. This will permit measurements up to beam energies of 700 MeV, which when unfolded will give much more accurate information on the cross section in the heart of the delta region, namely 100 to 200 MeV pions. Of all the total cross section measurements by the activation method, this case should be the best to extend to higher energies due to the relatively small contribution from the two step-background. It will be interesting to see if the impulse approximation can hold up even at very high energies.

Figure Captions

1. Level diagram of the A=12 system

2. Summary of data for the M1 form factor for the 15.11 MeV level in ^{12}C. Curve is from HA78.

3. Threshold data for $^{12}C(\gamma,\pi^-)^{12}N$. (BE76) Solid line is calculation of Epstein (EP78), thin line that of Nagl (NA79). Hatched zone shows envelope of unfolded cross sections. Long dashed curve is linear form without 190 MeV point, short dashed is parabolic. Dashed-dot is linear with 190 MeV point, and dotted is parabolic.

4. High energy data for $^{12}C(\gamma,\pi^-)^{12}N$ of EP74. Top curve is the yield, bottom the unfolded cross section. Points with error bars are their cross section; the hatched zone was deduced from their data using methods described in Appendix 1. Theoretical curves are as in previous figure.

5. Layout of experimental apparatus.

6. Drawing of rotating target wheel.

7. Diagram of electronics used in experiment.

8. Typical pulse height and timing histograms.

9. Time spectrum showing relative contributions of flat background and 10.97 msec decay of ^{12}N.

10. Top curve shows how real-to-virtual ratio is extracted from data points. Bottom curve shows real-to-virtual ratios for $^{12}C(\gamma,\pi^-)^{12}N$ compared to prediction using E1 form of Dalitz-Yennie spectrum (DA57)

11. Real-to-virtual ratios taken from BL77.

12. Raw data for $^{13}C(\gamma,p)^{13}B$ from all runs.

13. Yields for $^{13}C(\gamma,p)$ of this author and $^{12}C(\gamma,n)$ of HY70 showing increase over giant dipole cross section (dashed lines) due to quasi-free pion production (solid lines).

14. Final photoproduction yield for $^{12}C(\gamma,\pi^-)^{12}N$. Open circles data of EP74. Curves are those of the next figure folded with the photon spectrum and with the two-step background (dashed line) added back in.

15. Final cross section for $^{12}C(\gamma,\pi^-)^{12}N$. Top curve results from unfolding with different paramatrizations as described in Appendix 1. Hatched area in bottom curve encloses the above curves. Solid line is calculation of SI79 with full fsi, dashed curve is with Coulomb only fsi. Dot-dashed curve is calculation of NA79.

Chapter 3

Total Cross Sections for $^{7}Li(\gamma,\pi^{-})^{7}Be$ and $^{9}Be(\gamma,2n)^{7}Be$

III.1 Introduction

This chapter describes some of the motivations for measuring the total cross sections for $^{7}Li(\gamma,\pi^{-})^{7}Be$ and $^{9}Be(\gamma,2n)^{7}Be$ in the resonance region, followed by details of the experimental procedures used to obtain accurate results. Comparison of the photopion results is made with DWIA calculations, where as in the case of $^{12}C(\gamma,\pi^{-})^{12}N$ good agreement is found over the energy range spanned. The influence of the delta on the $(\gamma,2n)$ reaction is observed, and an accurate measurement of the real to virtual ratio for this reaction provides a precision test of virtual photon theory.

A. Motivations

There are several motivations for measuring the $^{7}Li(\gamma,\pi^{-})^{7}Be$ total cross section through the resonance region. One is that ^{7}Be has only two particle stable bound states, which facilitates comparison with theoretical calculations (see Fig. III-1). Another is the long half life (53 days) for emission of 478 KeV photons from the 10.4% electron capture to the first exited state of ^{7}Li (see Fig. III-1) (AJ74). This permits a clean separation from 511 KeV photons arising from the decay of other nuclei produced in the target. Finally, this same analog transition has been

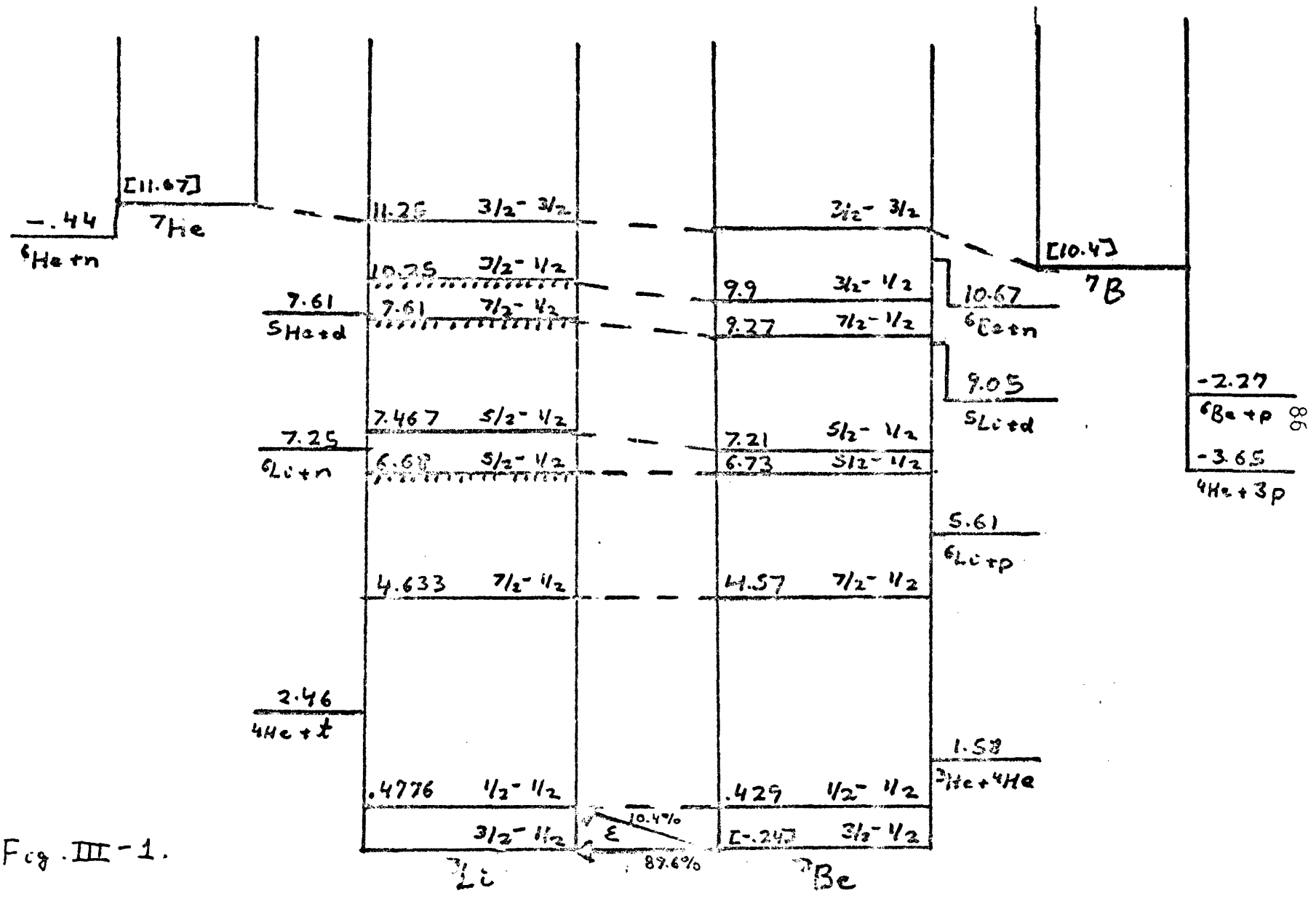
[11.67]
-.44
7He
6He+n
11.28 3/2- 3/2
10.75 3/2- 1/2
7.61
5He+d
7.61 7/2- 1/2
7.467 5/2- 1/2
7.25
6Li+n
6.68 5/2- 1/2
4.633 7/2- 1/2
2.46
4He+t
.4776 1/2- 1/2
3/2- 1/2
7Li
10.4%
ε
89.6%
3/2- 3/2
9.9 3/2- 1/2
9.27 7/2- 1/2
7.21 5/2- 1/2
6.73 5/2- 1/2
4.57 7/2- 1/2
.429 1/2- 1/2
[-.24] 3/2- 1/2
7Be
[10.4]
7B
10.67
6Be+n
9.05
5Li+d
5.61
6Li+p
1.58
3He+4He
-2.27
6Be+p
-3.65
4He+3p

Fig. III-1.

seen previously in $^{7}Li(\pi^{+},\pi^{0})^{7}Be$, where the experimental total cross section in the resonance region is found to be a factor of two larger than the best available calculations. (AL79)

From the point of view of performing calculations, some information on the pion optical is provided by total elastic cross section measurements, while elastic differential cross sections for pion scattering on nearby nuclei also provide valuable constraints. Information of the relative pion scattering from ^{7}Li and ^{6}Li of DY77 provides information on the isovector components. From the nuclear structure point of view, ^{7}Li is a good shell model nucleus, so that the wave function of Cohen and Kurath (CC65) should provide a good description of the relevant particle-hole states in the p shell.

Finally, the motivation for studying the $^{9}Be(\gamma,2n)$ reaction is to see if the influence of the delta can be seen as was the case in similar experiments on carbon and oxygen (JO76). The yields from these experiments are shown in Fig. III-2, where the additional yields from pion production (solid lines) can be clearly seen rising above the below threshold contributions(dashed lines). Since the number of particle stable final states is small in both cases, they should be directly comparable to the results for the $^{9}Be(\gamma,2n)$ Be reaction.

Since the same final state is reached by the

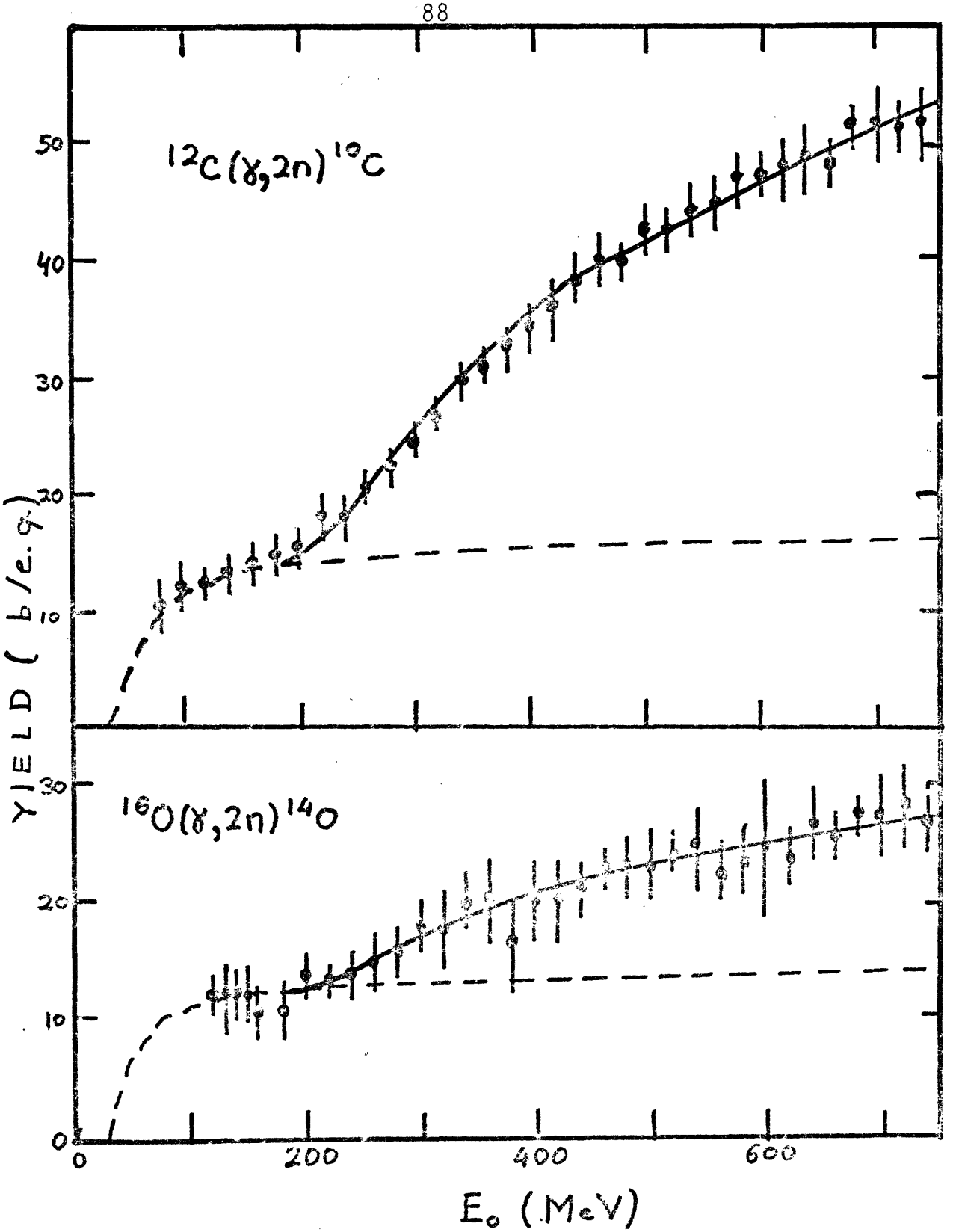
$^{12}C(\gamma,2n)^{10}C$
$^{16}O(\gamma,2n)^{14}O$
YIELD (b/e.g.)
E_0 (MeV)
0
10
20
30
40
50
200
400
600

Fig. III-2.

$^{9}Be(\gamma,2n)^{7}Be$ reaction as in the photopion experiment, this measurement could be easily performed by simultaneously irradiating beryllium samples with the lithium samples and counting the ^{7}Be activity at leisure to determine the yield.

B. Previous Measurements

The first measurement of this cross section was made by V. Noga et al using the Kharkov Linear Accelerator in the Ukraine. (NO71) They measured 12 data points from 100 MeV to 1.18 Gev with typical error bars of 30% by irradiating 1.0 cm thick lithium targets with the bremsstrahlung photon beam. While this data was useful in determining the order of magnitude of the cross section, it is of such poor quality that only a guess could be made as to the contribution of the two-step background, and any attempt to unfold their data to obtain a cross section would probably be meaningless. It should furthur be noted that, due to two misprints, the data presented in the reference is too low by a factor of ten (private communication from V. Noga). Only after the present data was measured was this error discovered.

The first effort to measure this cross section at the MIT Bates Linear Accelerator was done in 1974, when interest was primarily concentrated in the threshold region. Several samples of LiH were irradiated with a photon beam whose maximum energy was varied between 130 and 190 MeV. Polyethylene targets were simultaneously irradiated at each

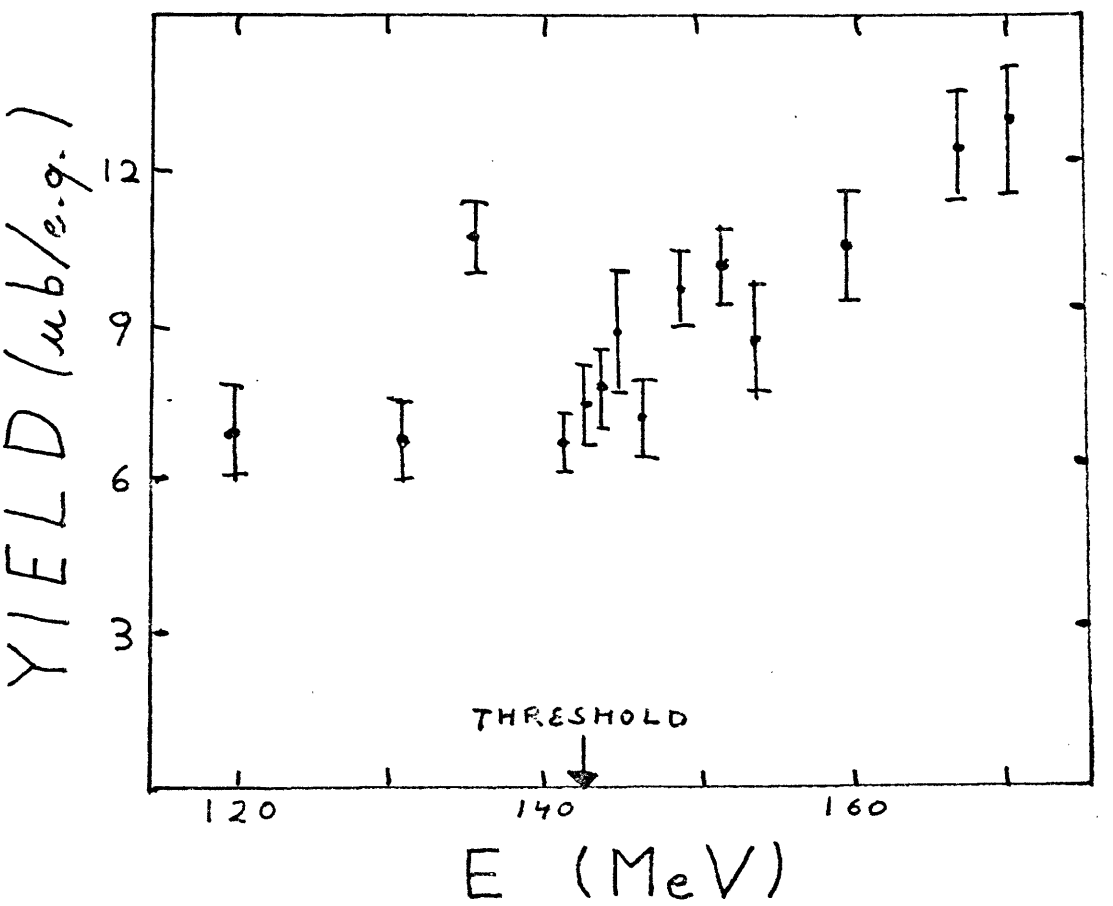

Fig III-3

energy in order to use the well known $^{12}C(\gamma,2n3p)^{7}Be$ reaction as an absolute monitor. (see Fig. III-5) (LU79,NO71, DI71). After transferring the LiH powder to uncontaminated cans, the activity from each sample was counted with a Ge(Li) detector.

The results are shown in Fig. III-3. Not included in the error bars is an estimated 30% overall normalization uncertainty arising from the lack of knowledge of the different geometrical detection efficiencies for the lithium and carbon samples. Note the much larger two-step background than in the $^{12}C(\gamma,\pi^{-})^{12}N$ reaction. These preliminary results will be found to be in reasonable agreement with the final experiment.

III.2 Experimental Setup

A. Targets

The previous experience was useful in planning to redo the experiment in the resonance region. The principal improvement to be made was in the selection of targets. Pure natural lithium metal cylinders 3.78 cm in diameter and 1.27 cm long were placed in aluminium rings and sealed in an argon atmosphere with thin foils on each end. Lithium metal is much easier to handle than LiH powder, which is extremely poisonous, tends to absorb moisture from the atmosphere in alarming quantities, and for which it is difficult to control geometrical effects, as the powder shifts in position when being transferred from one container to another.

Graphite cylinders of the same dimensions were used for the monitor reaction $^{12}C(\gamma,2n3p)^{7}Be$. In addition, thin cylinders 3.78 cm diameter and .127 cm long of Be were also irradiated at several energies in order to observe the $^{9}Be(\gamma,2n)$ Be reaction.

A rotating remotely controlled target wheel, capable of holding six sets of targets, was built so that targets could be changed between energies without having to open up the irradiation area. This also permitted us to irradiate targets on parasite time. Figure II-5 shows the location of the target wheel. The beam passed through the pion spectrometer target chamber, through an additional BeO radiator, and then was swept away into the beam dump, leaving only the photon beam to hit the targets approximatly 155 cm from the radiators. At electron energies between 100 and 340 MeV, the photon beam then had an average diameter of 1.7 cm, close to the size of the targets.

After the samples were irradiated, they were brought upstairs to cool off for at least a week. The lithium samples were then transfered, inside an argon dry box, to unirradiated aluminium holders, as the original holders now contained an appreciable amount of Be produced by spallation as well as large amounts of ^{24}Na, whose 2.1 year half-life positron decay produces .511 MeV annihilation gamma rays close to the ^{7}Be gamma peak.

B. Detection System

The samples were then counted by placing them on top of a NaI crystal 5.8 cm in diameter by 5.8 cm long shielded by a 4 cm thick copper wall. Typical counting times were several hours for the lithium samples and five to ten minutes for the carbon and beryllium samples. With these counting times, the statistics on the number of counts in the 478 keV peak were no longer the limiting factor in the accuracy of the experiment. Systematic fluctuations between samples irradiated at the same energy were on the order of 4.5%, while the statistical error on the ratio of the peaks obtained from the carbon and lithium samples was typically on the order of one percent. Samples in each group were counted on the same day so that the half life correction in forming the ratios would not be of importance. Each group was recounted several weeks later as a check. It was found that these later counts were in agreement with the original ones within the error bars. The observed half-life for all runs with good statistics was very close to the accepted value of 53 days (AJ74).

III.3 Data Analysis

A typical lithium spectrum obtained with the NaI crystal is shown in Fig. III-4. The two curves shown under the data points are empirical data obtained from very high statistics runs. The flatter curve is from a two day room background run. The small 511 keV peak is indicated with an arrow. The curve with the large peak was obtained from a

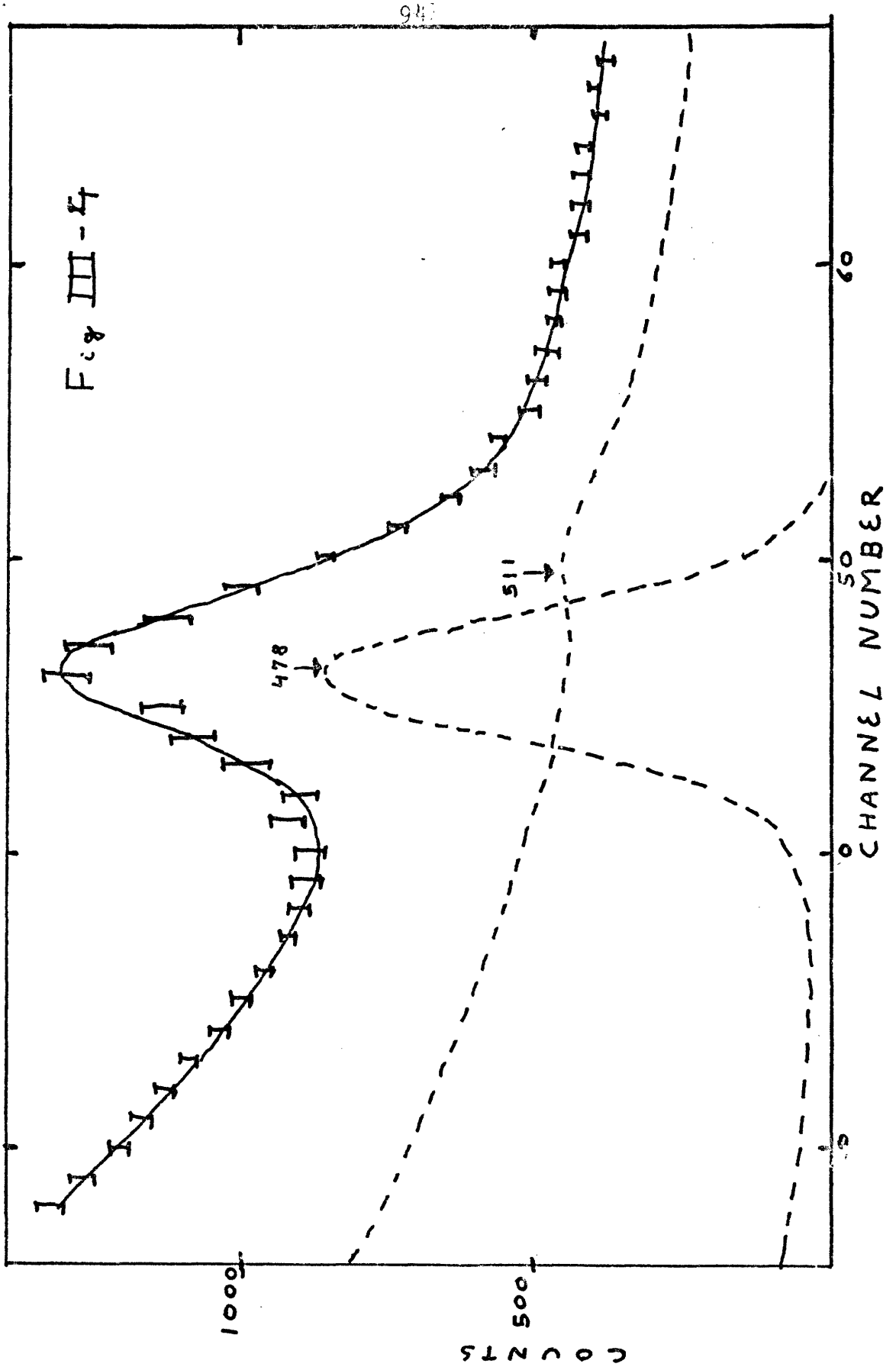
Fig III-4
478
511
0
50
60
CHANNEL NUMBER
500
1000
COUNTS

carbon disc that had received a large dose of photons, and is essentially a pure 478 KeV photon energy peak. Note the Compton tail on the low energy side, which makes it hard to paramatrize this function by a polynomial plus a gaussian shape, which was the method used at first to fit the data. Since this method did not give good χ^2 for the fits, a three parameter fit using these two empirical curves was used instead. Each curve was multiplied by a constant factor, and a third constant allowed for small shifts in the energy calibration of the multichannel analyzer. The nonlinear fitting program CURFIT described by Bevington (BE69) was used to make the fits.

For groups of data taken within a time span in which the analyzer was not touched by other users, the peak shifting constant was found to stay the same to within a few tenths of a percent. Since the peak obtained from the lithium samples was often not large enough to determine this constant well, the value obatined from carbon samples counted on the same day was sometimes used to reduce the error bar on the value of the lithium peak.

The solid line passing through the typical spectrum shown in Fig. III-4 represents the result of the best three parameter fit to the data. The χ^2 per degree of freedom is 1.23. The limiting factor on acheiving a better fit was slight variations in the shape on the background level, an effect that was taken into account by analyzing the data

with several different background runs and averaging the results.

III.4 Absolute Normalization

A. Normalization to Monitor Reaction.

Once the peak area for the 478 KeV photons has been determined for all three targets, (lithium carbon, and beryllium), irradiated at the same energy, the ratios of these peak areas can be used to determine the absolute yields by normalizing to the known spallation yield from carbon. All the available data for this reaction has been plotted in Fig. III-5 (Lu79, NO71, DI71). It can be seen that between 100 and 360 MeV the data is well represented by a straight line on a plot where the y-axis is linear and the x-axis is logarithmic. A 2 parameter least squares fit of this form gives

$$Y(E) = 151.5 \ln(E/28.53), \qquad \text{III-1}$$

where E is in Mev and the yield is in microbarns per equivalent quanta. This is shown as the solid line in Fig. III-5, where it can be seen that the fit reproduces the data with an accuracy of better than 5%, on the same order as the scatter between the points.

B. Relative Correction Factors

The next step is to determine the numbers of atoms in each target. This is found to be the product of Avagadro's number divided by the atomic weight of the target in grams with the purity of the sample, the weight in grams per cubic

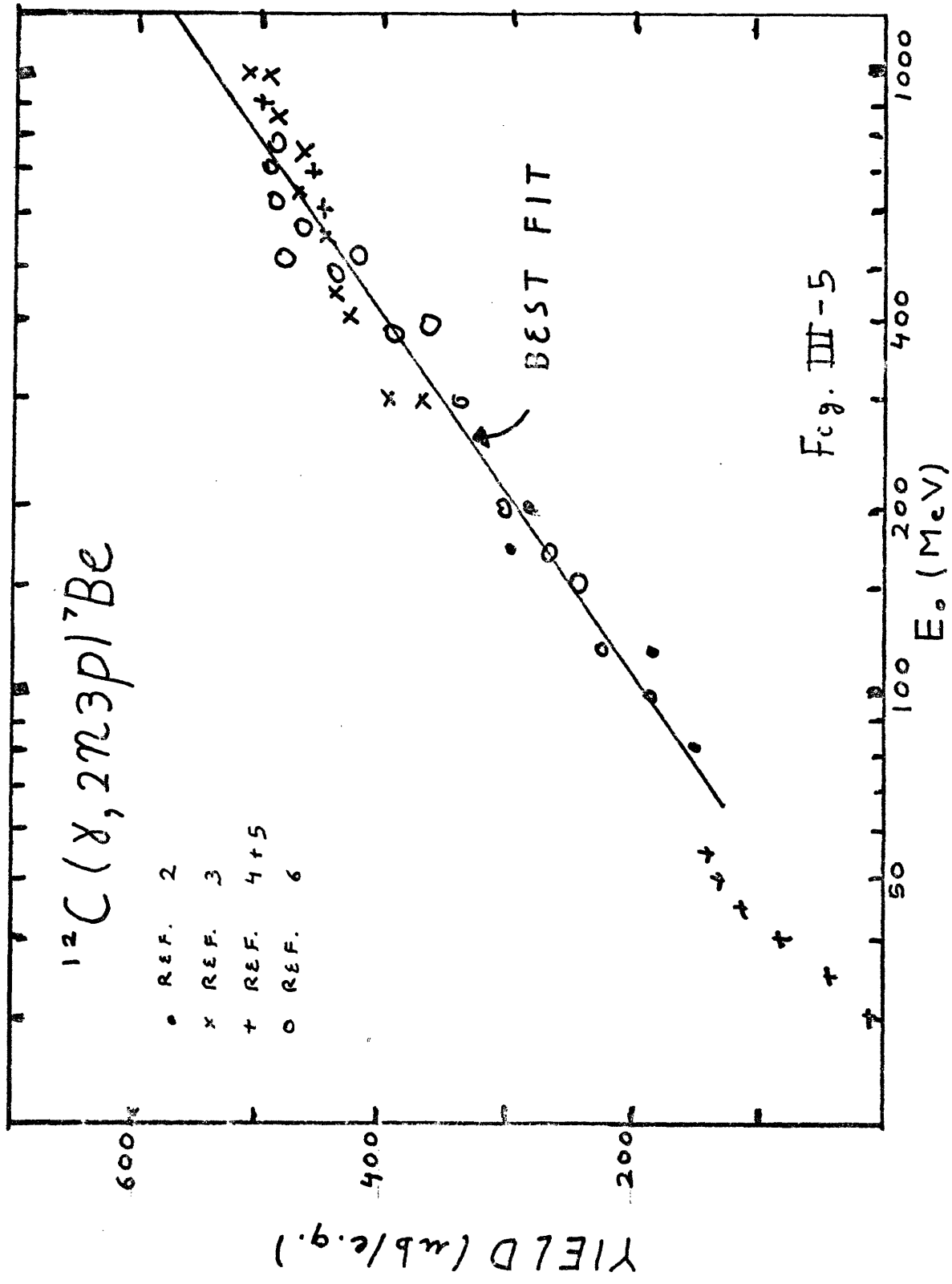
$^{12}C(\gamma, 2n3p)^{7}Be$
• REF. 2
x REF. 3
+ REF. 4+5
o REF. 6
BEST FIT
YIELD (mb/e.q.)
600
400
200
50
100
200
400
1000
E_0 (MeV)

Fig. III-5

centimeter, and the thickness in centimeters. The purity of the targets is 99% for carbon, 92.6% for the lithium targets, and 100% for the beryllium targets. The densities were found to be 1.804 gm/cm^3 for carbon, .534 gm/cm^3 for lithium, and 1.848 gm/cm^3 for beryllium. The respective atomic weights are 12.000, 6.940, and 9.010, and the respective thicknesses are 1.27 cm, 1.27 cm , and .127 cm. Putting these factors together, one finds, in units of Avagadro's number, the number of atoms/cm^2 to be 19.06 for the carbon samples, 9.03 for the lithium samples, and 2.604 for the beryllium samples.

A further correction comes from the average transmittance for 478 KeV photons passing through the different samples. The absorbtion coefficients are found to be .100 cm^2/g for lithium, .097 cm^2/g for beryllium, and .087 cm^2/g for carbon. Using the densities and thicknesses of the targets given above, one finds the average transmittances to be .965, .983, and .911 respectively.

The last correction comes from the different geometries for detection. Since the beryllium samples are considerably thinner than the carbon samples, their yields must be scaled down to be that which would have been counted had the samples been half the carbon samples thickness away from the detector. This was measured by simply moving the beryllium sample .62 cm from the NaI detector and measuring the reduction in yield, which was found to be a factor of .808.

Combining all these factors together, one finds that the lithium absolute yield can be found by multipliing the ratio of the areas of the peaks from lithium and carbon normalized to the same counting time by the yield for carbon at that energy and and by the normalization factor 2.231. The corresponding factor for beryllium is found to be 6.36.

C. Systematic Errors

Since as many as seven groups of targets were irradiated at different times at the same energy, the results were averaged together. Systematic variations in the yields at the same energies were on the order of 4.5%, significantly greater than the statictical errors, so this value was used in assinging error bars to the points. Table III-1 shows the number of targets taken at each energy for which there was more than one target along with the percentage statistical errror and the mean deviation for that group. The weighted average of the mean deviations is also given.

In the case of beryllium, only one sample was irradiated at each energy due to the high cost of obtaining targets, so that only the statistical errors were used.

III.5 Absolute Yield for $^{7}Li(\gamma,\pi^{-})^{7}Be$

When the corrections described in the last section are applied to the ratios for $^{7}Li(\gamma,\pi^{-})^{7}Be$ to $^{12}C(\gamma,x)^{7}Be$, the final absolute yields shown in Fig. III-6 are obtained. Several features of the yield curve will now be discussed, including the contribution of the two-step background, com-

energy	number targets	statistical error	standard deviation
100.	4	.045	.083
140.	4	.024	.083
160.	4	.015	.050
170.	4	.016	.030
190.	4	.012	.020
200.	4	.014	.040
210.	4	.011	.035
220.	8	.007	.061
230.	5	.005	.031
240.	7	.012	.044
250.	5	.008	.083
260.	2	.008	.059
270.	5	.012	.059
280.	2	.023	.028
310.	4	.022	.036
330.	2	.028	.046
350.	2	.027	.001
average			.044

Table III-1. Comparison of statistical and systematic errors for energies at which many lithium targets were sampled.

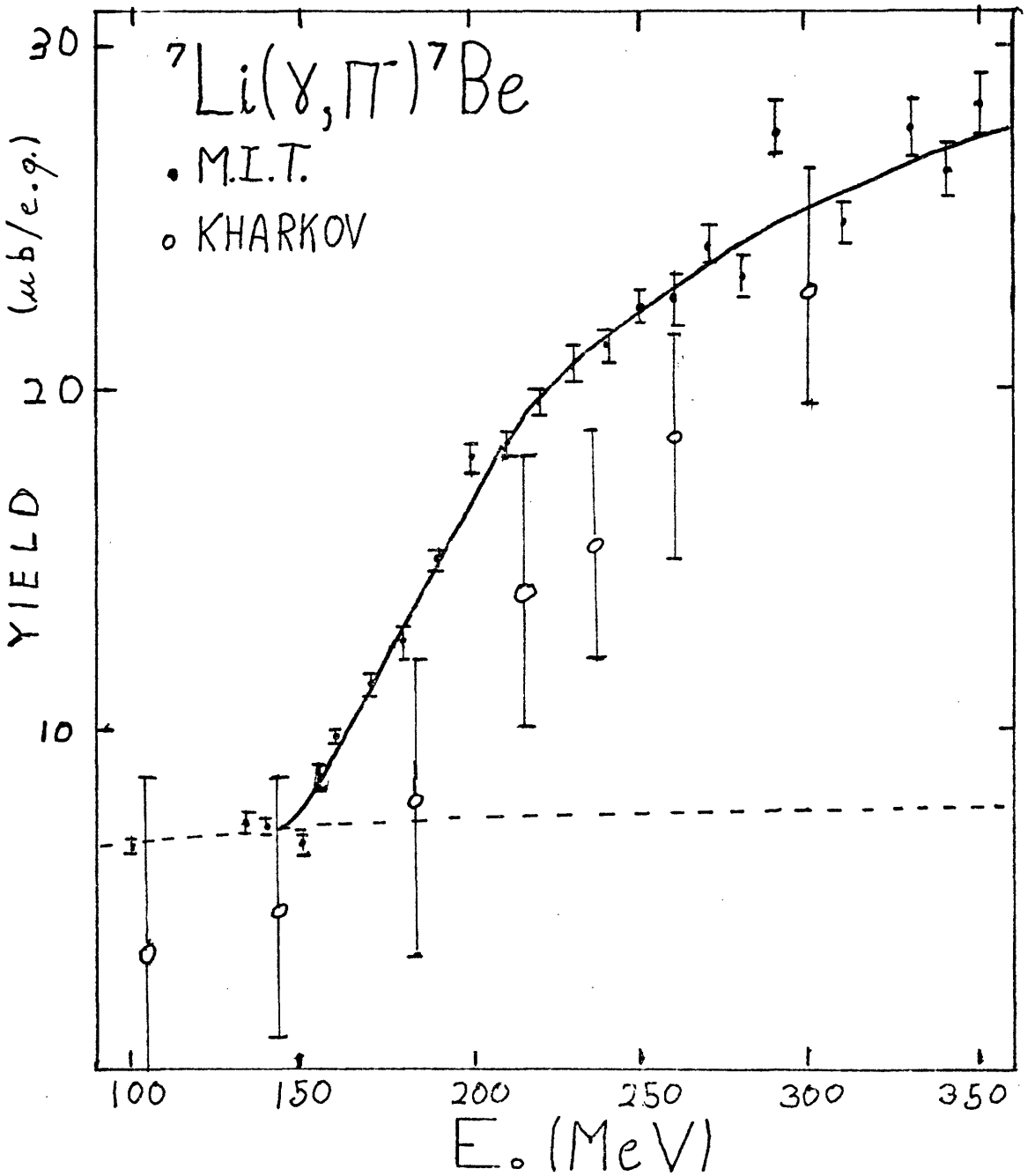
$^7Li(\gamma,\pi^-)^7Be$
• M.I.T.
o KHARKOV
YIELD (μb/e.g.)
30
20
10
100
150
200
250
300
350
E_γ (MeV)

Fig III-6

parison with the Kharkov results, and the checks that were made to ensure the reliability of the present data.

A. Two-step Background

It can be seen that the below-threshold two-step background arising from $^{7}Li(\gamma,p)^{6}He$ followed by $^{7}Li(p,n)^{7}Be$ is relatively quite large. Since the (γ,p) cross section peaks at around 20 MeV and falls off exponentially thereafter, one would expect this background to vary quite gradually with energy in the delta region. A yield curve calculated from a typical (γ,p) cross section was fit to the below-threshold points and continued to higher energies. It is shown as the dashed curve in figure III-6. Unfortunatly this does not take into account the proton production from $^{7}Li(\gamma,p\pi^{o})$, which should become significant at around 165MeV photon energy. Since this cross section is generally about 10 times smaller than the (γ,p) cross section, and since there are many less available photons of the needed energies, this effect is assumed to be small and is neglected for the time being.

An attempt was made to measure the two-step background directly using very thin (.8 mm) lithium foils from which a substantial fraction of the protons would escape. The attempt was unsuccesful for two reasons. The first was that the counting rate was very small, making it difficult to distinguish the 478 KeV peak from the room background. The second was that the foils tended to curl up inside their

containers, thus changing their effective thicknesses.

In order to be able to correct the yields if a more accurate two-step background becomes available, the numerical values of the raw yields and the values of the background used in the present subtraction are tabulated in Table III-2.

B. Comparison with Other Experiments

Comparison with the Kharkov points shows that while we are in agreement for the overall shape, particularly as regards the ratio of two-step yield to pion yield, the difference in absolute magnitude is off by a factor of 30%.

In order to resolve this discrepancy, several tests were made. First, several groups of targets were counted with both a NaI crystal and a Ge(Li) detector. Although the Ge(Li) detector has a much lower efficiency, it has a much better resolution and if we had accidentally been including a nearby peak in the lithium results, we may not have seen it with the NaI crystal. Since both detectors gave the same yields, this possibility could be ruled out.

Another possibility is that the ^{7}Be we were counting in the lithium samples was produced by spallation from impurities in the metal. The main impurity was known to be ^{14}N, which was only guaranteed by the manufacturers to be less than 1%. Since the yield from impurities follows the same general shape as that for the two-step background, most of the possible effects from target impurities were taken care

Energy	Yield	Error	Bkgrnd	Error	Result	Error
100.	6.55	.15	6.68	.14		
135.	7.29	.24	7.00	.14		
140.	7.18	.16	7.07	.15		
150.	6.60	.22	7.12	.15	-.52	.30
155.	8.61	.39	7.16	.15	1.45	.42
160.	9.77	.21	7.20	.15	2.57	.26
170.	11.3	.26	7.23	.15	4.07	.30
180.	12.5	.57	7.27	.15	5.2	.59
190.	14.9	.34	7.30	.15	7.6	.37
200.	17.9	.41	7.34	.15	10.5	.44
210.	18.3	.42	7.23	.15	10.9	.44
220.	19.6	.40	7.40	.16	12.2	.43
230.	20.7	.47	7.43	.16	13.3	.50
240.	21.2	.45	7.45	.16	13.8	.48
250.	22.4	.51	7.47	.16	14.9	.53
260.	22.5	.81	7.51	.16	15.0	.82
270.	24.2	.55	7.57	.16	16.6	.57
280.	23.2	.74	7.61	.16	15.6	.75
290.	27.4	.89	7.66	.16	19.7	.90
310.	24.8	.57	7.69	.16	17.1	.59
330.	27.6	.89	7.72	.16	19.8	.87
340.	26.4	.86	7.74	.16	18.6	.87
350.	28.3	.92	7.76	.16	20.6	.93

Table III-2. Final absolute yields for $^{7}Li(\gamma,\pi^{-})^{7}Be$ showing relative contribution of the two-step background. Units are in μb.

of automatically when this subtraction was made.

Taking all the possible errors into account, it is believed that the overall systematic errors should not be greater than 10% for the yields and final cross sections for the $^{7}Li(\gamma,\pi^{-})^{7}Be$ reaction.

III.6 Cross Section for $^{7}Li(\gamma,\pi^{-})^{7}Be$ and Comparison with Theory

A. Unfolding

The final total cross section for $^{7}Li(\gamma,\pi^{-})^{7}Be$ was obtained by subtracting the two-step background from the yield curve and then using the unfolding method described in appendix 1. Shown in Fig. III-7 are several representative fits. The four solid lines are the results when the cross section is paramatrized in terms of polynomials in powers of the energy above threshold of maximum degrees three, four, five, and six. The two dashed curves are the cross sections when the paramatrization is assumed to be a sum of eight equally spaced gaussians with widths of 30 or 50 MeV. It can be seen that all these curves are in good agreement within the error bars, which are only shown for the sixth degree polynomial. Therefore, this zone was used as the description for the final cross section for the $^{7}Li(\gamma,\pi^{-})^{7}Be$ total cross section in the delta region.

B. Comparison with Theory

The only available calculation is that of Singham and Tabakin (SI79). They used the form of the elementary ampli-

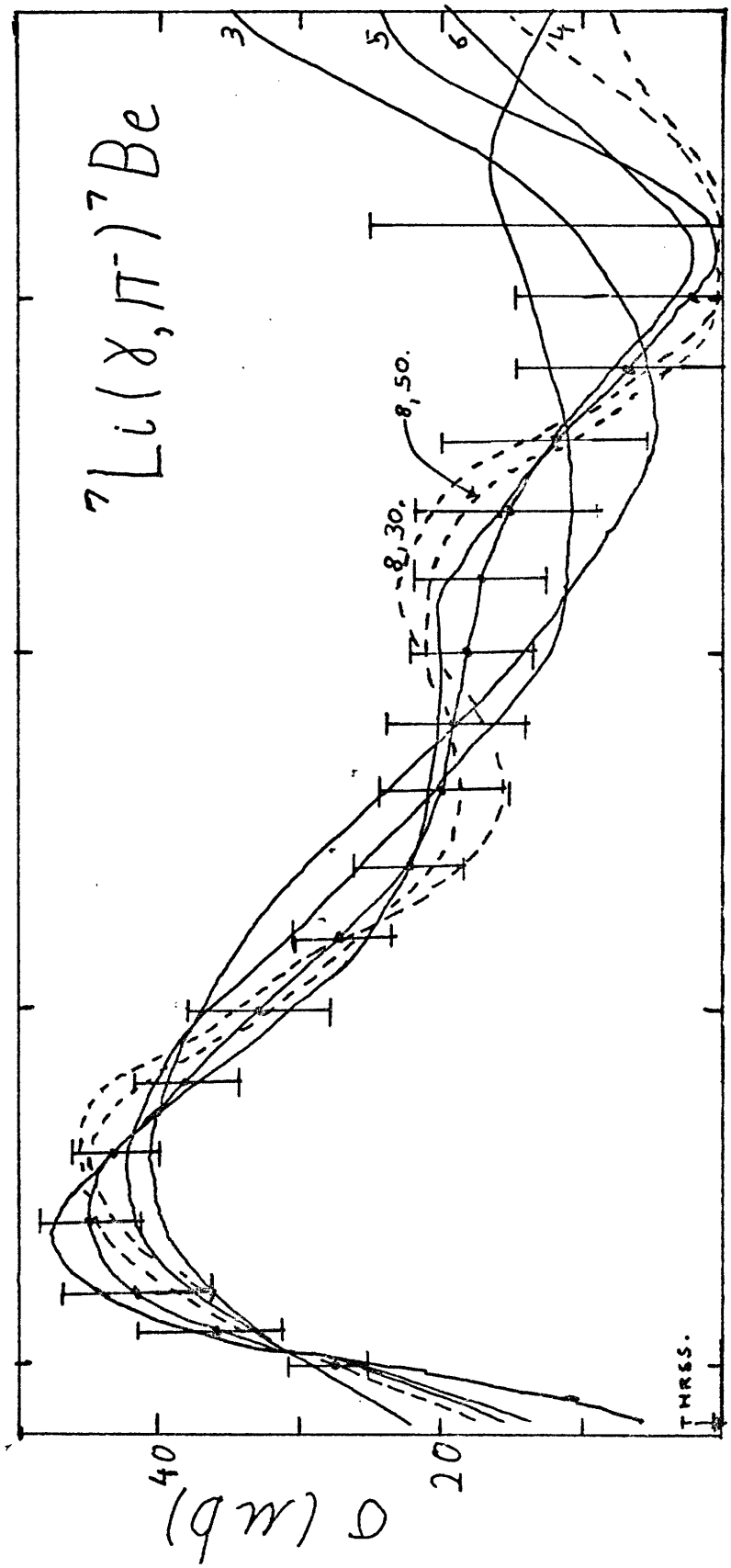
$^7Li(\gamma,\pi^-)^7Be$
3
5
6
14
8,50.
8,30.
THRES.
150
200
250
300
20
40
E_γ (MeV)
σ (mb)

Fig. III-7

tude of Blomqvist and Laget (BL77), and the nuclear wave functions generated by the shell model code of Cohen and Kurath (C065) to generate the 24 different transition densities needed to connect the 3/2- ground state of ^{7}Li with the 3/2- and 1/2- ground and first excited states of ^{7}Be. These wave functions give accurate predictions of the static properties of ^{7}Be, such as the beta decay matrix elements. Although the transverse electron scattering data is not available for the analog states in lithium, the shell model based on particle hole states in the p-shell does a good job in describing the charge form factors that have been measured, and hence can be used with confidence.

The pionic atom data was used to obtain the pion optical potential parameters up to 10 MeV, after which the increasing importance of the energy dependent terms makes it necessary to use an optical potential fit to differential elastic pion scattering data. They used the parameters of Stricker et al (ST79) modified slightly to agree with the total pion cross sections measured by Clough (CL74). To fit the lithium data at low energies (DY78) the Stricker parameters had to be modified by increasing the s-wave repulsion and increasing the p-wave πN attraction in the potential.

The results of their calculations, as well as the hatched area enclosing the experimental cross section, are shown in Fig. III-8. For plane waves and the full operator (dash-dot curve) one sees that the decreasing overlap of the

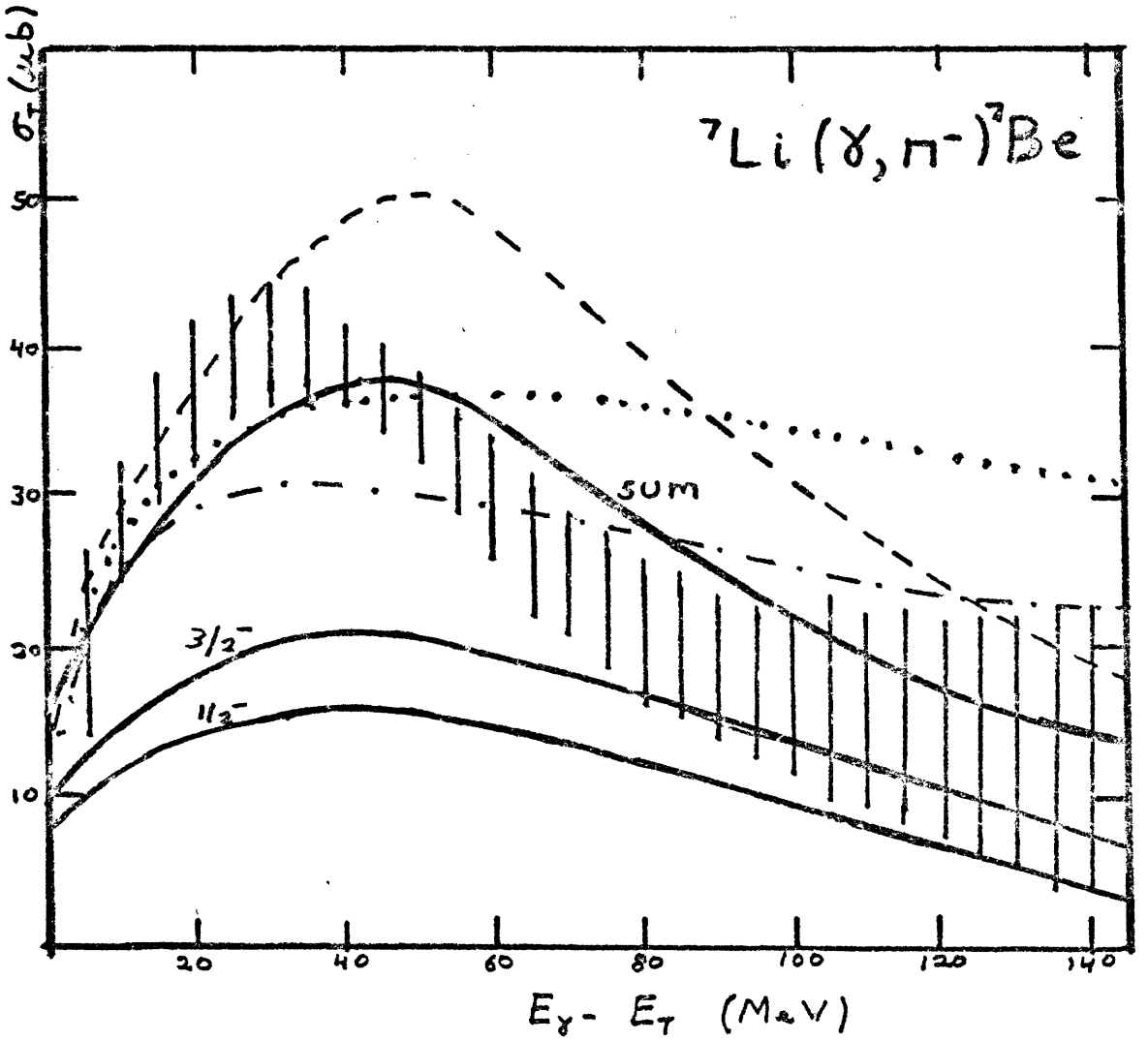
σ_T (μb)
$^7Li(\gamma, n^-)^7Be$
50
40
30
20
10
SUM
$3/2^-$
$1/2^-$
20
40
60
80
100
120
140
$E_\gamma - E_T$ (MeV)

Fig III-8

nuclear wave functions with increasing energy has the effect of damping out the peak of the delta resonance. Turning off the momentum dependent terms in the operator (dotted curve) increases the magnitude slightly while leaving the shape basically the same. Turning on the full pion distortions raises the cross section at threshold from zero to the finite value of 15μb due to the increased overlap of the nucleus with the pion wave function (solid curve). This effect is felt up to about 60 MeV, after which the ever increasing p-wave absorption begins to pull the cross section below that of the plane wave version (dashed curve).

C. Summary and Conclusions

As in the case of the total cross section for $^{12}C(\gamma,\pi^-)$ described in the previous chapter, the results of the present experiment to measure the total cross section for $^{7}Li(\gamma,\pi^-)^{7}Be$ from 0 to 150 MeV energy pions is found to be in very good agreement with the results of a distorted wave impulse approximation calculation in which the nuclear structure and pion distorted wave inputs were constrained to fit known static and dynamic properties. As will be discussed in more detail in Chapter Five, this is somewhat surprising in view of the large discrepancies found in the analogous $^{7}Li(\pi^+,\pi^0)^{7}Be$ reaction, which probes the same initial and final states with pions and was also measured by the activation method (AL79). In this case, large corrections to the impulse approximation are found to be needed to

account for the large cross sections observed.

We have now seen good agreement with DWIA calculations for two cases, an analog and a non-analog total photopion cross section in the 0 to 150 MeV range. The number of final states in both cases is very small, permitting accurate comparison with calculations, unlike the problems encountered in accounting for the total cross sections for $^{27}Al(\gamma,\pi^+)$ and $^{51}V(\gamma,\pi^+)$ of BL77, where the number of final states is large and unknown. In Chapter Five several possiblities for obtaining more information from total photopion cross sections will be given. We note that the present measurement on lithium could be improved in the energy region above 300 MeV, where better statistics points should be taken and the range extended to higher energies. This will be done in the near future by parasiting off other planned total cross section measurements.

III.7 Results for the $^{9}Be(\gamma,2n)^{7}Be$ Reaction.

A. Yield and Total Cross Section.

Figure III-9 shows the yields obtained for the $^{9}Be(\gamma,2n)^{7}Be$ reaction using the normalizations described in section III.5. Also shown are the data obtained by the Kharkov group and others in 1971 (NO71). It can be seen that in this case, in contrast to the lithium measurement, we are in fairly good agreement. Unfortuantly, there is no good data available below 120 MeV. Among the data points that do exist there seems to be a large dispersion. Therefore, aver-

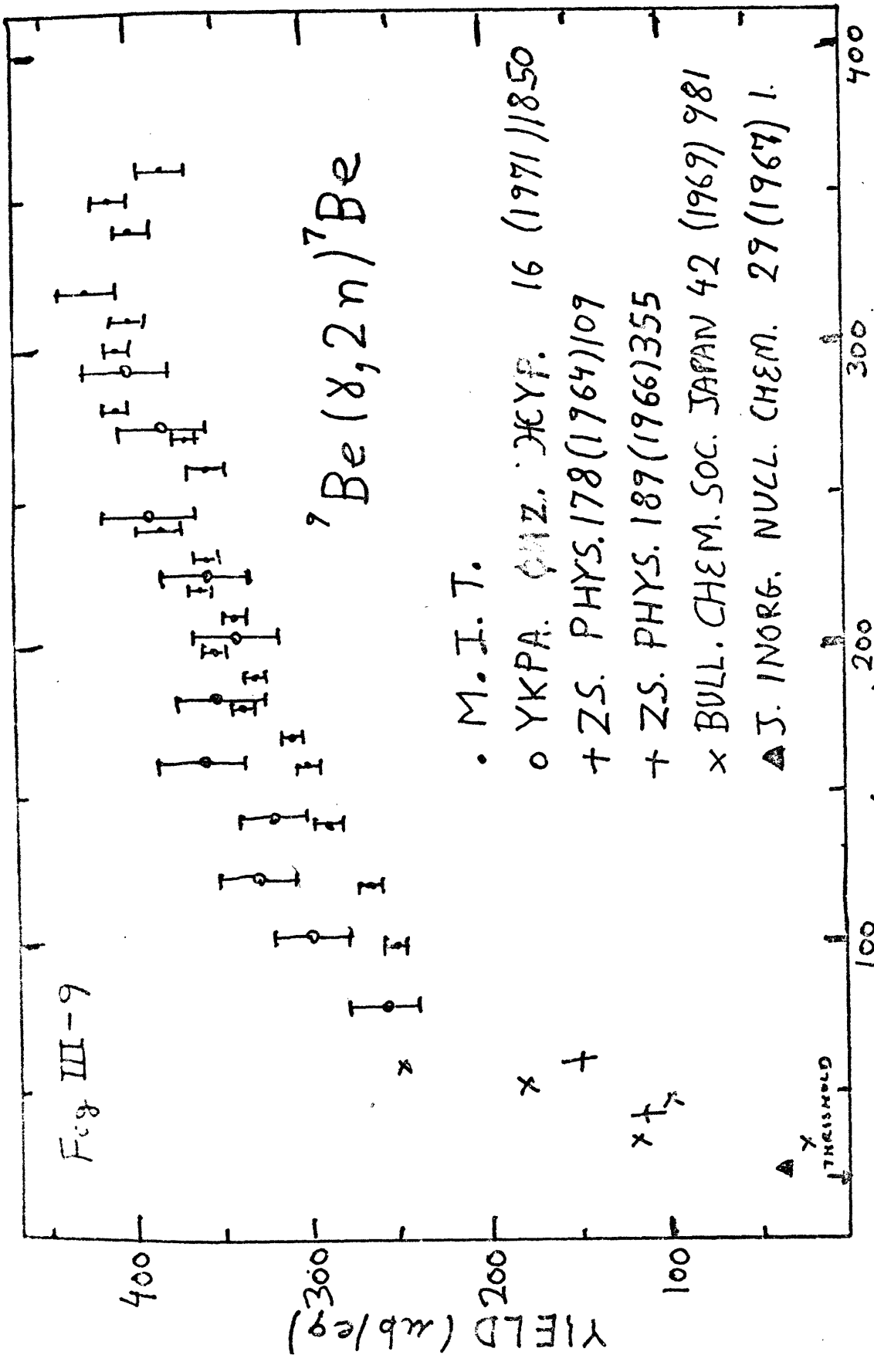
$^9Be(\gamma,2n)^7Be$
• M.I.T.
o YKPA. ФИЗ. ЖЭТФ. 16 (1971) 1850
+ ZS. PHYS. 178 (1964) 109
+ ZS. PHYS. 189 (1966) 355
× BULL. CHEM. SOC. JAPAN 42 (1969) 981
▲ J. INORG. NUCL. CHEM. 29 (1967) 1.
THRESHOLD
YIELD (μb/eq)
E_0 (MeV)
100
200
300
400

Fig III-9

age values at 25, 50, 75, and 100 MeV were taken when unfolding the data.

The results for the resulting cross section are shown in Fig. III-10a. The cross hatched area encloses polynomials of third, forth, and fifth degrees, with the value at the threshold of 21.2 MeV fixed to be zero.

B. Comparison with Other Experiments

For comparison, the results of Johnsson et al (JO76) for $^{12}C(\gamma,2n)^{10}C$ and $^{16}O(\gamma,2n)^{14}O$ are shown in figures III-10b dnd III-10c. The shape of their cross sections is readily interpreted as a giant-resonance interaction at low energies followed by the onset of pion production which basically follows the form for the free delta, indicating that final state interactions and nuclear-structure effects are relativly weak when compared to pion production without nucleon emmissions. Our data for beryllium, though of much poorer quality, due to the lack of low energy yield points, follow the same basic trends. The factors contributing to the much larger magnitude of the cross sections are not yet understood.

C. Real-to-Virtual Ratio

In order to test the Dalitz-Yennie (DY) (DA57) virtual spectrum for a $(\gamma,2n)$ reaction, for which the dipole multipoles of the virtual photon should dominate (since they are not forbidden by selection rules), the real-to-virtual ratio was measured for $^{9}Be(\gamma,2n)^{7}Be$ at 135 MeV.

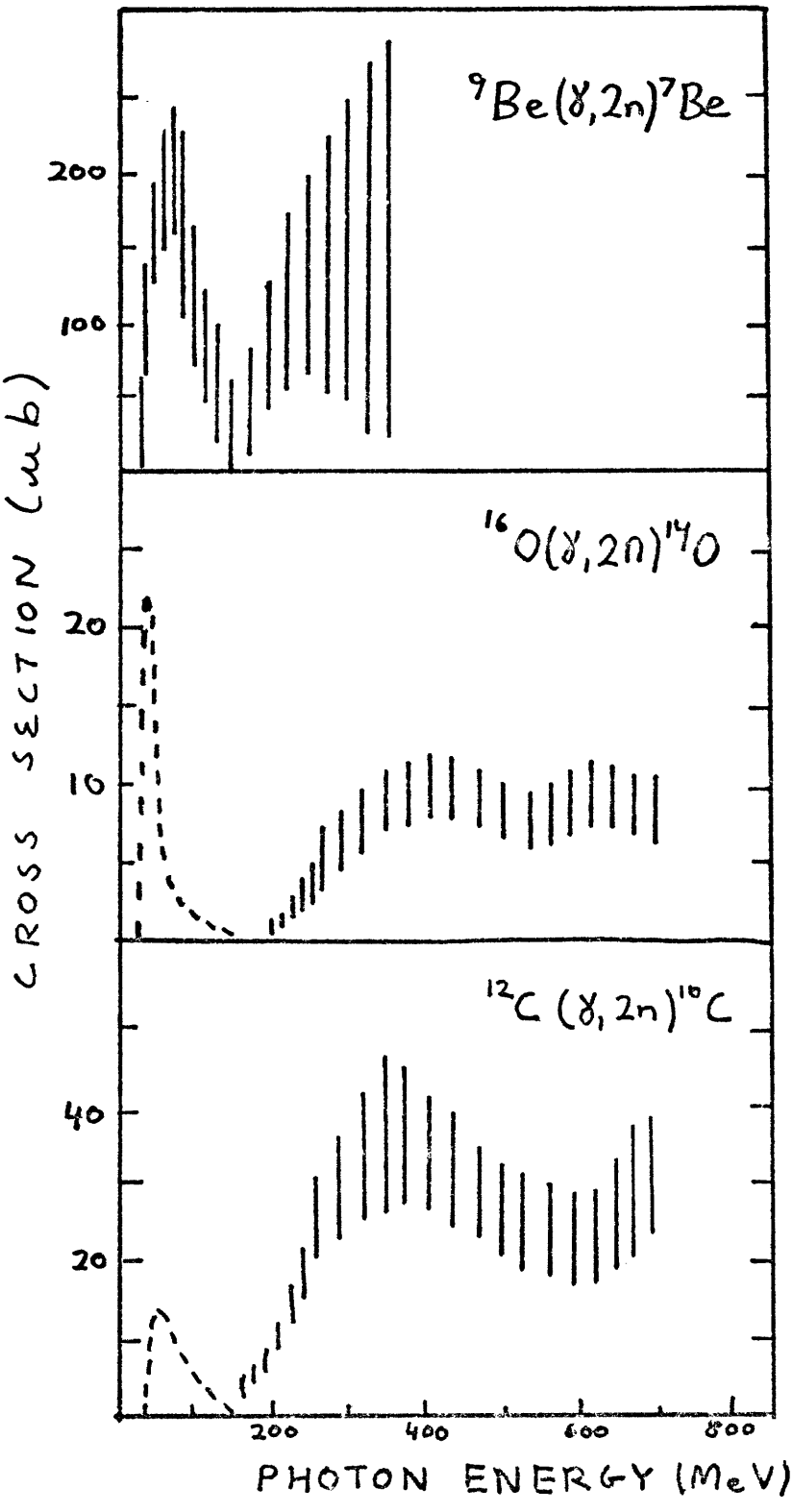
$^{9}Be(\gamma,2n)^{7}Be$
200
100
$^{16}O(\gamma,2n)^{14}O$
20
10
$^{12}C(\gamma,2n)^{10}C$
40
20
CROSS SECTION (mb)
200
400
600
800
PHOTON ENERGY (MeV)

Fig III-10

The measurement was done as a parasite off another real-to-virtual ratio study being undertaken by C. Barber. For that reason, a rather complicated packet of targets was irradiated by the electron beam of the Bates LInac. Nonetheless, of the two beryllium samples irradiated, one received a substantially larger fraction of real photons, so that a relatively good statistics value on the real-to-virtual ratio could be extracted by comparing their yields. The real-to-virtual ratio thus obtained was 53.1±.6, in good agreement with the value of 53.6 predicted by the dipole form of the DY spectrum when folded with the cross section derived in the last sub-section.

We conclude that this form of the virtual spectrum seems to work well in the region far from the endpoint, for cases in which selection rules do not prohibit dipole photons, and when the present result is added to those found for the $^{12}C(\gamma,\pi^+)^{12}N$ reaction (see section II-5) and the $p(\gamma,\pi^+)n$ reaction (see section IV-9).

Figure Captions

1. Level diagram for the A=7 system.

2. Yield data for $^{16}O(\gamma,2n)^{14}O$ and $^{12}C(\gamma,2n)^{10}C$ of J076.

3. Threshold data for $^{7}Li(\gamma,\pi^-)^{7}Be$ taken in 1975.

4. Typical NaI spectrum for the 478 KeV gamma observed from the decay of ^{7}Be..

5. Summary of existing data for the monitor reaction $^{12}C(\gamma,2n3p)^{7}Be$.

6. Yield versus endpoint energy for the $^{7}Li(\gamma,\pi^-)^{7}Be$ reaction in the delta region. The dashed line is the two-step background, and the solid curve is calculated from the predictions of Singham et. al. shown in Fig. III-7 with the two-step contribution added back in..

6. Extracted cross section for $^{7}Li(\gamma,\pi^-)^{7}Be$. The different curves result from different paramatrizations, either in terms of polynomials or gaussians, as explained in Appendix 1. The error bars are shown for the sixth degree polynomial only.

8. Cross section compared to theory for $^{7}Li(\gamma,\pi^-)^{7}Be$. The hatched zone encloses the results shown in the previous figure. Calculations of Si79. Dotted curve is Kroll-Rudeman term only with plane wave pions, dashed with full distortions. Dashed-dotted curve is full operator with plane waves, solid curve with full distortions. Contributions from each of the two final states is shown.

9. Summary of measured yields for $^{9}Be(\gamma,2n)^{7}Be$.

10. Extracted cross section for $^{9}Be(\gamma,2n)^{7}Be$ compared with two other $(\gamma,2n)$ activation measurements in the delta region.

Chapter Four

Differential Cross Sections for $^{10}B(\gamma,\pi^+)$ and $^{16}O(\gamma,\pi^+)$

IV.1 Introduction

This chapter describes the measurement of the differential cross sections for $^{16}O(\gamma,\pi^+)^{16}N$ and $^{10}B(\gamma,\pi^+)^{10}Be$ to bound states of the daughter nuclei at a lab angle of 90° and pion energies from 80 to 200 MeV.

The measurements were made by passing the electron beam of the Bates Linear Accelerator through BeO and packed powder boron targets and detecting the pions produced at 90° using the Bates Energy Loss Spectrometer in conjunction with a total absorption Cerenkov counter to reject electrons and positrons. By measuring in the region corresponding to the highest energy photons allowed by energy conservation (the endpoint region), the contributions from the the sum of the four lowest lying states in ^{16}N and the ground and first excited states in ^{10}Be separately by distinguished. The results represent the first photopion differential cross section measurements in the delta region for nuclei heavier than helium, and represent a significant advance over the information previously available only from total cross sections.

A. Theoretical Motivation

As was mentioned in Chapter One, these measurements represent only a first step in a larger program to make a detailed study of the (γ,π) reaction in the delta region

through complete angular distribution measuremtns at several energies for several nuclei. The final program has yet to be decided, but likely candidates are discussed in Chapter Five when a review of interesting experiments to be done is made.

Differential cross sections measurements make for much more precise comparisons with calculations since only one value of the momentum transfer to the nucleus is sampled at a time. For example, if the momentum transfer is kept fixed and the pion energy is varied, the nuclear structure aspects can be kept more or less fixed but the production amplitude and final state interactions will be strongly varying with energy. These types of measurements should therefore provide a basis for substantial new physics information.

The two cases chosen for the first measurements in the delta region were selected for both experimental and theoretical reasons. The experimental reasons will be discussed in the next subsection, but we note that for both of these cases the nuclear structure is reasonably well constrained from electron scattering measurements of the transverse form factors. Both have large M3 components, and hence peak at the relatively large momentum transfer region covered in the present experiment. The pion optical parameters for these cases are well constrained by elastic and inelastic scattering of charged pions

from the light nuclei at the relevant energies. It should therefore be possible to make a good test of the impulse aprroximation for (γ,π) reactions in the delta region by investigating these two cases.

B. Experimental Motication

The present measurements were done as a first step for several reasons. From the point of view of detector development, it was decided to start in a region where the requirements on the background rejection ratios would not be too great. Since the background for (γ,π^-) reactions is much larger than for (γ,π^+) reactions, the later was chosen. The background also increases rapidly with decreasing angle, therefore the value of 90° was chosen as being the greatest scattering angle at which normalization could still be conveniently be made to the well-known $p(\gamma,\pi^+)n$ reaction (see kinematics graph Fig. IV-1).

As mentioned before, the cases of $^{16}O(\gamma,\pi)^{16}N$ and $^{10}B(\gamma,\pi^+)^{10}Be$ were ideal, since the transverse form factors to the anlog states in the parent nuclei had been measured and peaked in the kinematic region spanned by the chosen conditions.

Another advantage of these targets was their ease of construction. For oxygen, BeO could be used, since the threshold for Be is much higher than for O and hence will not contribute to the endpoint spectra for the states observed in this experiment. The same is true for ^{10}B,

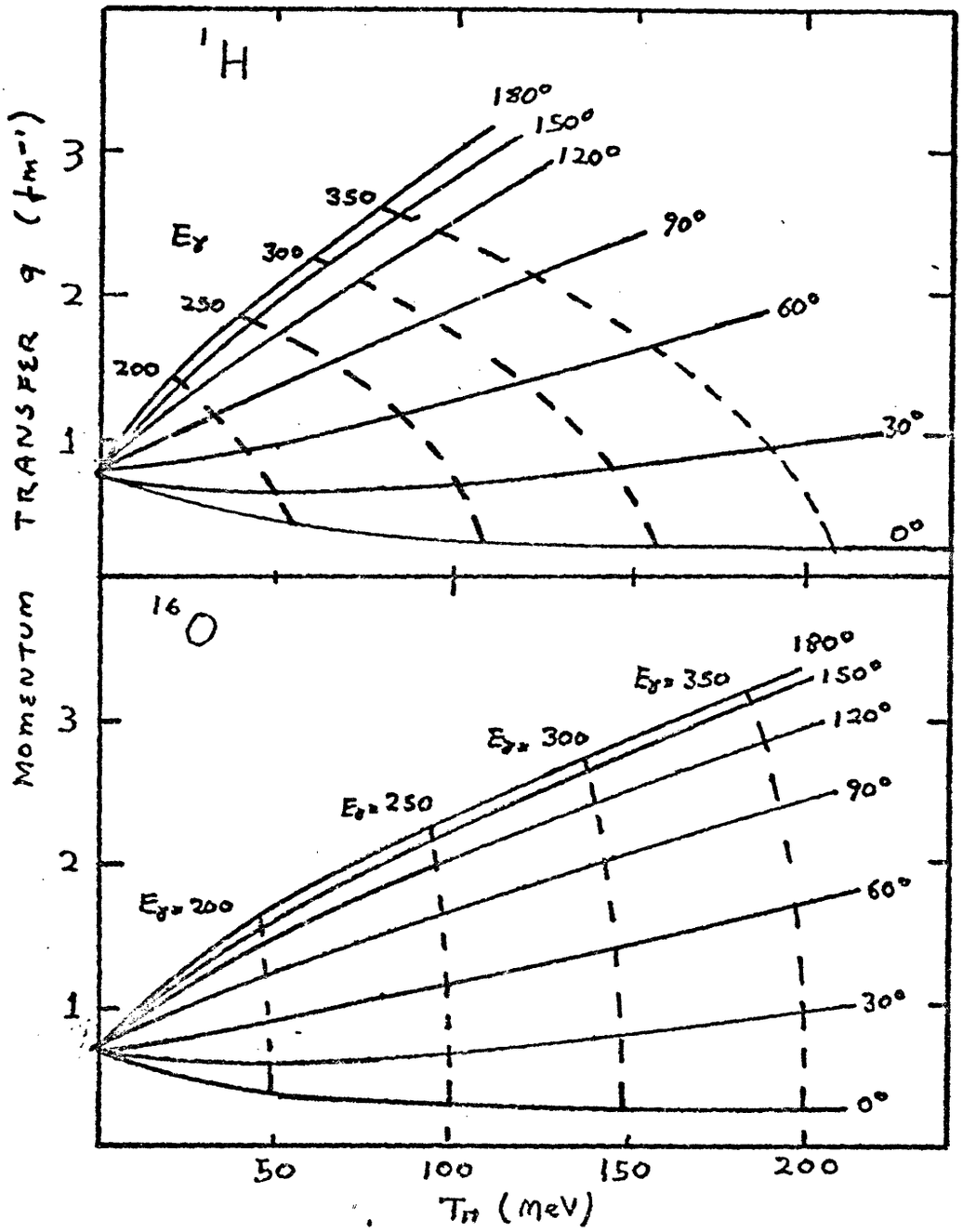
^1H
180°
150°
120°
350
E_γ
300
90°
250
60°
200
30°
0°
MOMENTUM TRANSFER q (fm^{-1})
^{16}O
180°
E_γ= 350
150°
E_γ= 300
120°
E_γ= 250
90°
E_γ= 200
60°
30°
0°
1
2
3
50
100
150
200
T_n (MeV)

Fig IV-1

where carbon foils can be used to encase the boron powder since the threshold for carbon is much higher than for boron (this is not true for the (γ,π^-) reaction, where special precautions must be taken).

Finally, the large gap (2.35 MeV) from the four closely spaced low-lying states in ^{16}N to the next excited state makes is easy to separate their contribution and thus measure their sum. The case of ^{10}B is even more favorable, with a large gap (3.35 MeV) between the ground and first excited states, and another (2.65 MeV) to the next state, permitting separate measurements of the contributions from both the ground and first excited states. It should be noted that these cases are fairly unusual; most other nuclei have much smaller level spacings, making it difficult to separate the contributions of different levels due both to resolution problems and the decreased number of photons available.

C. Overview

An overview of the rest of the chapter is now given in order that the reader might have a clearer picture of how all the different pieces fit together to form the final results.

The next section discusses some of the methods that might be used in conjunction with a pulsed electron beam and a high resolution spectrometer to eliminate electron and positron backgrounds to $(\gamma,\pi^\pm)$ reactions that arise

when the beam passes through the target. This is done both with the aim of understanding the problems that were encountered in the present measurement and how they might be better solved in the future. The performance of the detection system actually used is reviewed in the following section.

The expected shape of the pion momentum spectrum for each bound state for both photo- and electroproduction is then derived, with the effects of beam resolution and target thickness taken into account. The differences between the predicted and observed shapes are then explained in terms of pions that decay in flight into muons. The results of Monte-Carlo calculations for these effects are presented.

At this stage a digression is made into the question of how eleastic electron scattering can be used to measure the energy of the incident electron beam. It is also shown how this information can be used to measure the detection efficiency of the system for electrons. Information about the response of the system for pions is obtained from quasi-free pion production, where the results are compared with the data from Bonn University. THe detection efficiency of the system versus energy is then found using the pion production from hydrogen in the endpoint region and comparing the results to the available data and dispersion relation calculations.

Finally, the measurement of the real-to-virtual ratios necessary to convert the electroproduction cross sections to photoproduction cross sections is described. When all these ingrediants are thrown together, the extraction of the $^{16}O(\gamma,\pi^+)^{16}N$ and $^{10}B(\gamma,\pi^+)^{10}Be$ cross sections can be made. The results for the sum of the first four closely spaced levels in ^{16}N and the ground and first excited states in ^{10}B separatly are then compared with the available calculations. The last section summarizes the experimental experience and theoretical infromation gained from the present experiments.

IV.2 Comparison of Different Detection Systems

Many methods are possible to solve the problem of rejecting large numbers of electrons and positrons to detect small numbers of pions. In this section we shall briefly examine most of them and comment on their relevance to the experiments that are planned in the New Hall of the Bates Linac using the new pion spectrometer presently under construction.

A. Time of Flight Method

The first method is to use the microstructure of the beam to obtain a time-of-flight measurement of the speed of the particle. For a five meter flight path the transit time for relativistic particles would be 16.6 nsec and the difference between a pion and an electron of 300 MeV momentum would be about 1.6 nsec. Since the time between

micro-pulses at Bates is only .35 nsec, serious ambiguity problems will result when trying to discriminate between particles, even with complete track reconstruction.

Variations on this theme are possible if one were to place a counter half way through the dipole and make a time-of-flight measurement to the focal plane. This would have to be a very thin scintillator so as not to overly degrade the resolution on the instrument, and it would be difficult to come up with a design that would place the tubes out of the magnetic field yet close enough to the plastic to acheive the very fine timing information required.

An easier solution might be to place a scintillator two meters or so behind the focal plane and do the time-of-flight measurement after the particle has passed through the wire chambers. If one accepts that the present limit of the technology to measure timing information is about .3 nsec, it is clear that the more energetic the pion and the greater the ratio of electrons to pions, the furthur the distance between the counters would have to be to obtain a clear discrimation. The basic problem then is the large divergence of the particles in the new spectrometer design, which would necessitate a very large second counter.

B. Differential Energy Loss in Scintillators

Another scheme is to use the differing amounts of en-

ergy deposited in a scintillator by the two particles. Since the pion moves more slowly, it gives a bigger pulse. This technique has been used extensively to detect pions of up to 50 MeV kinetic energy, but above this value is no longer practical as the pion is moving too fast. Even if the pion is slowed down by a suitable amount of absorber, the straggling deteriorates the signal substantially. This effect, combined with the substantial losses from true pion absorbtion render the practicable limit of this method to about 60 MeV.

C. Low Refractive Index Cerenkov Detector.

Another alternative is to use a Cerenkov counter whose index of refraction is so low that only electrons will be detected. If the highest pion energy to be detected is 325 MeV, with a speed of .95c, then the index of refraction should be less than 1.05. It should have as thin walls as possible to minimize the number of electrons lost in the walls due to radiation, yet should have as high an index as possible as the number of photoelectrons generated is proportional to this quantity squared. One possibility is to use high pressure gas counters. These present some safety problems (hydrogen being the best gas to use) and requires thick containment walls. The main problem with using gases is the large area one would need to cover (most models are built for use with relatively well collimated beams).

The best solution seems to be silica aerogel, which is a foam plastic material with an index of refraction of up to 1.05 made of cells with about 30 angstroms in diameter. The material is rather opaque, making it difficult to collect enough photoelectrons per event to avoid loses in efficiency due to poisson fluctuations. A detector is presently being constructed using a diffusion box to scatter the light into three or more five inch phototubes, whose first dynodes are specially treated with GaAs to give them good one photelectron quantum efficiency. Using a 6. cm thick by 30 cm wide by 80 cm long slice of aerogel of index of refraction 1.05, we hope to get 16 photoelectrons on the average per event, so that the principal inefficiencies would be caused by radiative and scattering processes. Used in conjunction with a total absorption lead glass Cerenkov detector to eliminate any electrons that the aerogel has not vetoed due to these possible radiative processes, a detection system should be able to be built that can handle electron-to-pion ratios as large as 1,000,000 to 1.

D. Total Absorption Cerenkov Detector.

A final alternative, and the one that we have used to collect the data described in this chapter, is a total absorption Cerenkov counter in which the electron leaves a much bigger signal than the pion. A traditional shower counter with scintillators interspersed with layers of

lead is not suitable for this low range of electron energies, as the average number of showers is only two or three and most of the information is lost in the lead convertors. But a counter that is made entirely of Cerenkov material and is at least ten radiation lengths long would capture, eventually, all of the electron's energy, whereas the pion would only radiate, and then with an ever diminishing amount of light, until it has slowed down to a speed of 1/n. The possibility that the pion would be absorbed sometime during this time only helps in the separation. Constructing the counter in several layers easily elimates low energy room-background electrons, whose total deposited signal may be similar to that of a typical pion. Probably the best material for the job would be 18" piece of lead glass, the first 6" being broken up into individual slices.

Unfortunately, this was not quickly available, so as an alternative it was decided to use five 2" thick slices of lucite, whose index of refraction is 1.49. Thus, instead of having 10 radiation lengths of material, there was only about one. This means that some of the electrons will pass part way through the counters, radiate a very high energy gamma, and stop. If the gamma then escapes the counter without pair producing, the signal will look very much like that from a pion.

In the next section the manner in which the counters

were actually built will be described and the results of tests of their performance will be presented.

IV.3 Performance of Total Absorption Counter

In this section the performance of the five 2" lucite counters for detecting pions in the delta region is described.

A. Construction of Counters.

The material used was ultra violet transmitting Type II lucite. This was held in place by a frame that only touched the lucite along four 1/16" wide strips at each end to minimize light losses. Four light guides at the end of each counter guided close to 100% of the light into four RCA 8575 phototubes. One hundred and twenty volt zener diodes were used in the last four stages of the tube bases. Although this restricts the operating range of the tubes somewhat, it eliminates "sagging" caused by the current drain of large instantaneous singles rates. An LED flasher was fanned out via a fiberoptics cable into the back of each counter so that the gains of all the tubes could quickly be equalized and monitored.

Since the Snell's angle for lucite is 43° and the opening angle for relativistic Cerenkov light is 48°, almost half the light is captured by total internal reflection when the counters are placed at 45° with respect to the beam. Their location beneath the vertical drift

Fig IV-2

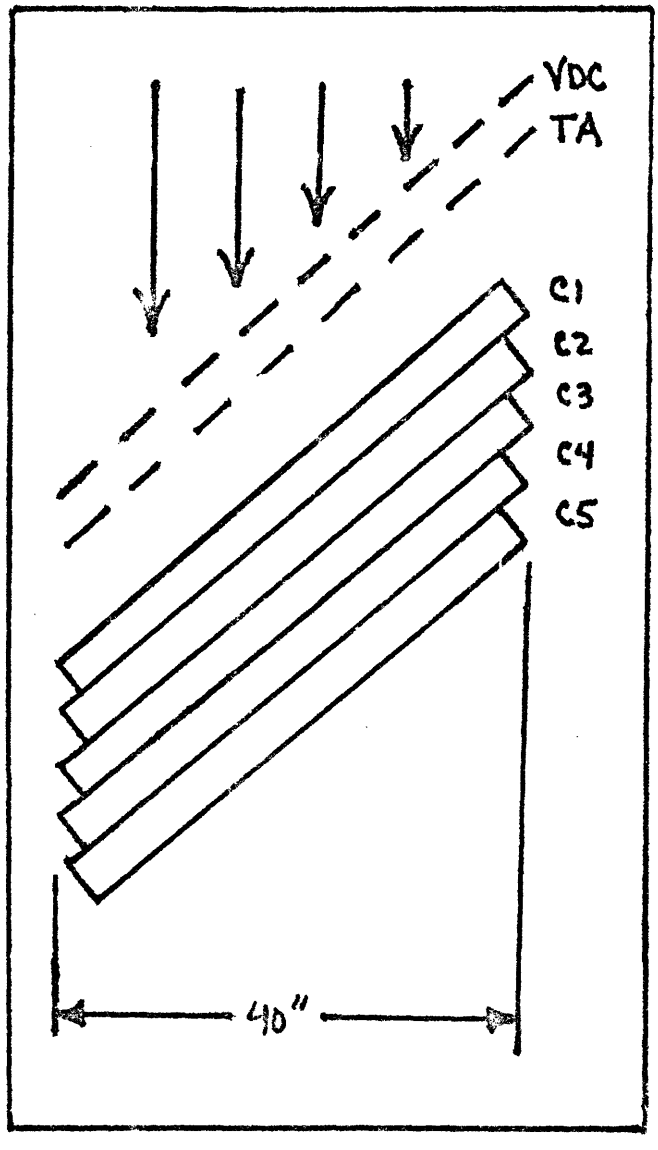

chamber and two transverse arrays in the pit of the Bates Energy Loss Spectrometer is illustrated in Fig. IV-2.

B. Performance of Counters.

The principle of operation is shown in Fig. IV-3a. These curves show the total amount of light given off by electrons and pions of various energies. As the pion slows down, it radiates less and less until at 56 MeV it stops radiating altogether. The electron, on the other hand, is always relativistic and radiates almost until it is stopped. Fig. IV-3b shows the ratio of the sum the pulse heights in all counters one would excpect for various incident pion energies. Since in this case the electrons go all the way through for momenta greater than 170 MeV, the electron signal is independent of energy. It can be seen that the experimental ratios are in good agreement with the predictions, giving us confidence in our interpretation of the experimental spectra. The results for the muons of the same momentum as the pions are also shown and again agree quite well with the predictions.

The total-pulse-height spectra used to obtain the relative pulse heights described in the last paragraph are shown in Fig. IV-4. The secondary bump that comes after the pion peak (most clearly visible for the 80 MeV pions) is attributed to muons which come from the decay of pions in flight, mostly in the first and last 3.5 meter drift spaces (see section IV-5). We note that although

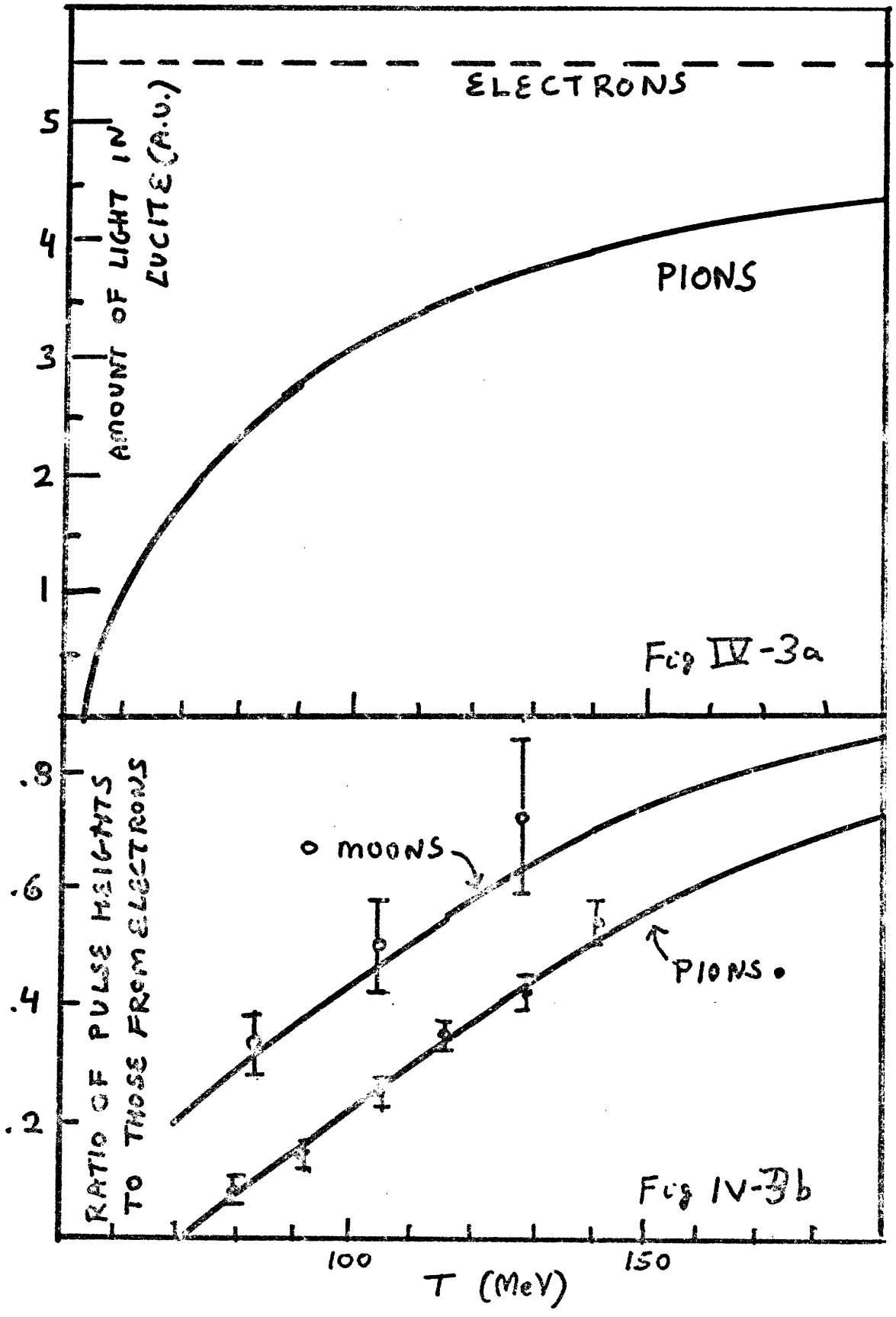
ELECTRONS
PIONS
AMOUNT OF LIGHT IN LUCITE (A.U.)
5
4
3
2
1
Fig IV-3a
RATIO OF PULSE HEIGHTS TO THOSE FROM ELECTRONS
.8
.6
.4
.2
o MOONS
PIONS •
100
150
T (MeV)
Fig IV-3b

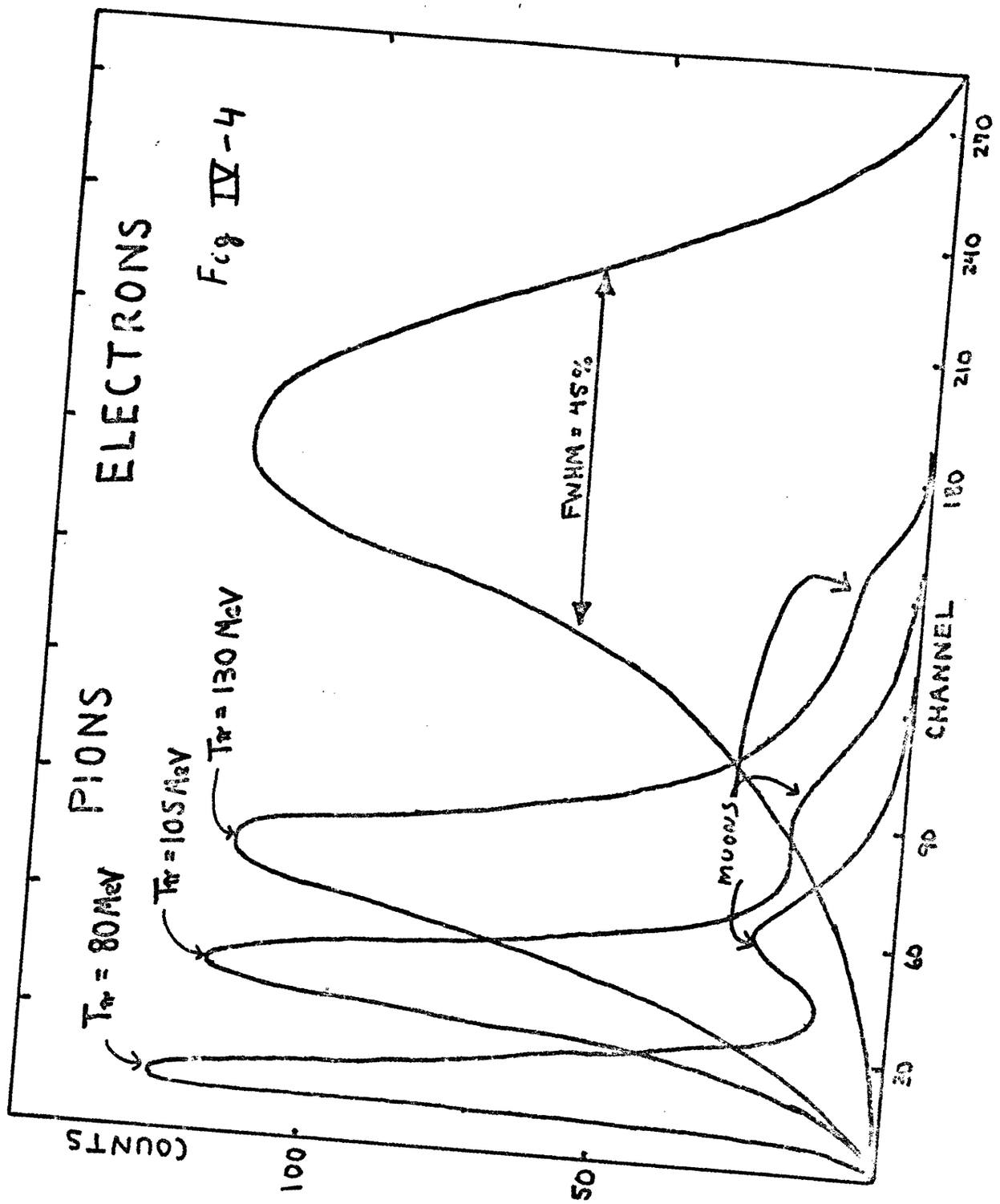
ELECTRONS
PIONS
Fig IV-4
FWHM = 45%
T_π = 80 MeV
T_π = 105 MeV
T_π = 130 MeV
MUONS
COUNTS
100
50
20
60
90
120
210
240
270
CHANNEL

corrections have been made on an event-by-event basis for experimentaly measured attenuations in the electron pulse height with increasing distance from the phototubes, the electron peak is still quite wide. This large width must be attributed to the various possible radiative, scattering, and straggling effects as the electron passes through the lucite. It is also possible that better matching of the gains of the individual counters could reduce the width.

The conclusion one must draw is that one radiation length is not sufficient to get good resolution on the electron or pion signals. By comparing areas and assigning reasonable upper cuts for the pion signals, one finds that a rejection ratio of 1:10,000 can be obtained for 80 MeV pions, 1:300 for 105 MeV pions, and only 1:20 for 130 MeV pions. Our preliminary studies have shown that one needs a rejection ratio on the order of 1:10,000 to measure (γ,π^-) cross sections. Thus, this detector will only be useful in the 70-85 Mev pion kinetic energy range. Fortunatly, we have found that a rejection ratio of only 1:2 is needed to measure even very small (ie. .01μb/sr) (γ,π^+) cross sections, and thus that this counter is usable over the entire energy range available at Bates, which is from 80 to 200 MeV. This last comment is valid for lab angles greater than 70^o. A short run at 45^o has shown that a rejection ratio on the order of one to twenty

is needed here.

IV.4 Photon Spectrum Shape

Now that we have the equipment for taking data, we know what to expect for the pion spectra that will be obtained. Given a particular electron beam energy and spectrometer angle, for each target and reaction there will be a unique threshold pion energy corresponding to a pion produced by a photon of the same kinetic energy as the incident electron. At lower pion momenta, more pions that leave the nucleus in its ground state will be produced as there are now more available bremsstrahlung photons as well as more virtual photons. The shapes of the pion spectra will thus follow the shapes of the photon endpoint spectra for each state, with succesive states adding in with the same shapes but shifted by the excitation energies of the individual levels.

A. Photoproduction.

Let us first deal with photoproduction. The exact shape of the pion spectrum is given by

$$S(p) = \sum_i \sigma_i(p)\,\phi(E_0, k_i(p)), \qquad \text{IV.1}$$

where the k_i are the photon energies corresponding to the different excited states of the residual nucleus labeled by i and the pion momentum p is given by the two-body kinematics. In order to simplify the data analysis, we assume that $\sigma(p)$ is a constant over the relatively small

momentum range spanned, and facilitate the calculation of k by writing

IV.2 $$k(p) = k(p_0) + \frac{dk}{dp}(p - p_0),$$

where p_0 is the threshold energy for that state. The derivitive term is given by the expression

IV.3 $$\frac{dk}{dp} = \frac{p}{E}\frac{(m_i - k - ke/p\cos(\theta))}{(m_i + p\cos(\theta) - e)},$$

where e is the pion energy, p the pion momentum, and m_i is the mass of the parent nucleus. The expression for dk/de is found by multiplying the above by e/p. We note that dk/de is only significantly different from 1. in the case of hydrogen.

B. Electroproduction.

In order to acheive reasonably high counting rates and still have a relatively small beam spot size, the beam was allowed to pass through the target in all the runs taken so far. Since the scattered electron is not detected, the three body final state also leads to a pion spectrum $d\sigma/d\mathcal{N}dp$, which is experimentally observed to have much the same shape as the bremsstrahlung tip. Although in principle one should compare directly with a calculation of the double differential cross section, unfortunately almost all calculations to date have been for photoproduction. In order to compare to these, we can use an effective spectrum for the virtual photons, such as the

one given by Dalitz and Yennie (DA57). Since almost all of the electrons scatter forward in a narrow cone, the virtual photons in the endpoint region are almost on-shell and their energy dependence is almost independent of multipolarity. We have found the shape of the electroproduction spectra observed so far (also see Nick Paras' thesis) (PA79) to be consistent with a simple dipole form given by

IV.4 $$\Phi(E_0,k) = \frac{\alpha}{\pi k}\left[\frac{e_i^2+e_f^2}{e_0^2-m_e^2}\right]\left(\frac{e_0e_f+p_0p_f\cos\theta}{m_e k}-\frac{2m_e}{p_i}\right)$$

where e_i and p_i are the energy and momentum of the inital electron, e_f and p_f are the energy and momentum of the final electron, and k is the photon energy. Again we make the assumption that the cross section is constant over the small energy intervals in question and factor it from the virtual photon shape, leaving only one parameter with which to fit each energy level.

C. Resolution Effects.

These considerations give us in principle the endpoint shapes; but first we must fold in the various resolution effects. In our case the spectrometer resolution is $1.2\cdot10^{-4}$, and can be neglected. For electroproduction, we fold in a square resolution which is given by the total energy loss in the target if we are in reflection mode, or one fourth of that amount if we are in transmission mode to account for straggling. Fortunately, the pion and electron energy losses are almost the same in our energy region and

thus can be set equal to a good approximation. In order to do the averaging over the required energy range, it is a good approximation to define a new shape U(e-k)

IV.5 $$U(\epsilon - k) = \frac{\epsilon}{\epsilon_0}\,\phi(\epsilon_0, k),$$

so that we only deal with differences from the endpoint energy. This approximation is not really needed for virtual photons, but greatly speeds the calculation of the real photon smearing, as the numerical formulas are so much more complicated in this case. For the case of radiator produced photons, we simply smear over the range of pion energy losses depending on where it was produced, as given by

IV.6 $$\phi_{RAD} = \int_0^T U\left(E_{kin} - t\, dE/dx\right) dt.$$

For target produced bremsstrahlung, we have a similar integral for each point in the target where the photon could have been produced, and thus must evaluate the double integral

IV.7 $$\phi_{BREM} = \int_0^{T_0} \int_T^{T_0} U\left(\frac{dE_0}{dt}\frac{(T-t)\cos\phi}{\cos(\theta-\phi)}\right) dt\, dT,$$

where the angles are defined in Fig. IV-5. This is valid for the transmission mode; in the reflection the expession in parentheses is replaced by $t\cdot\cos(\phi)/\cos(\theta-\phi)$. We used the transmission mode whenever possible, with the

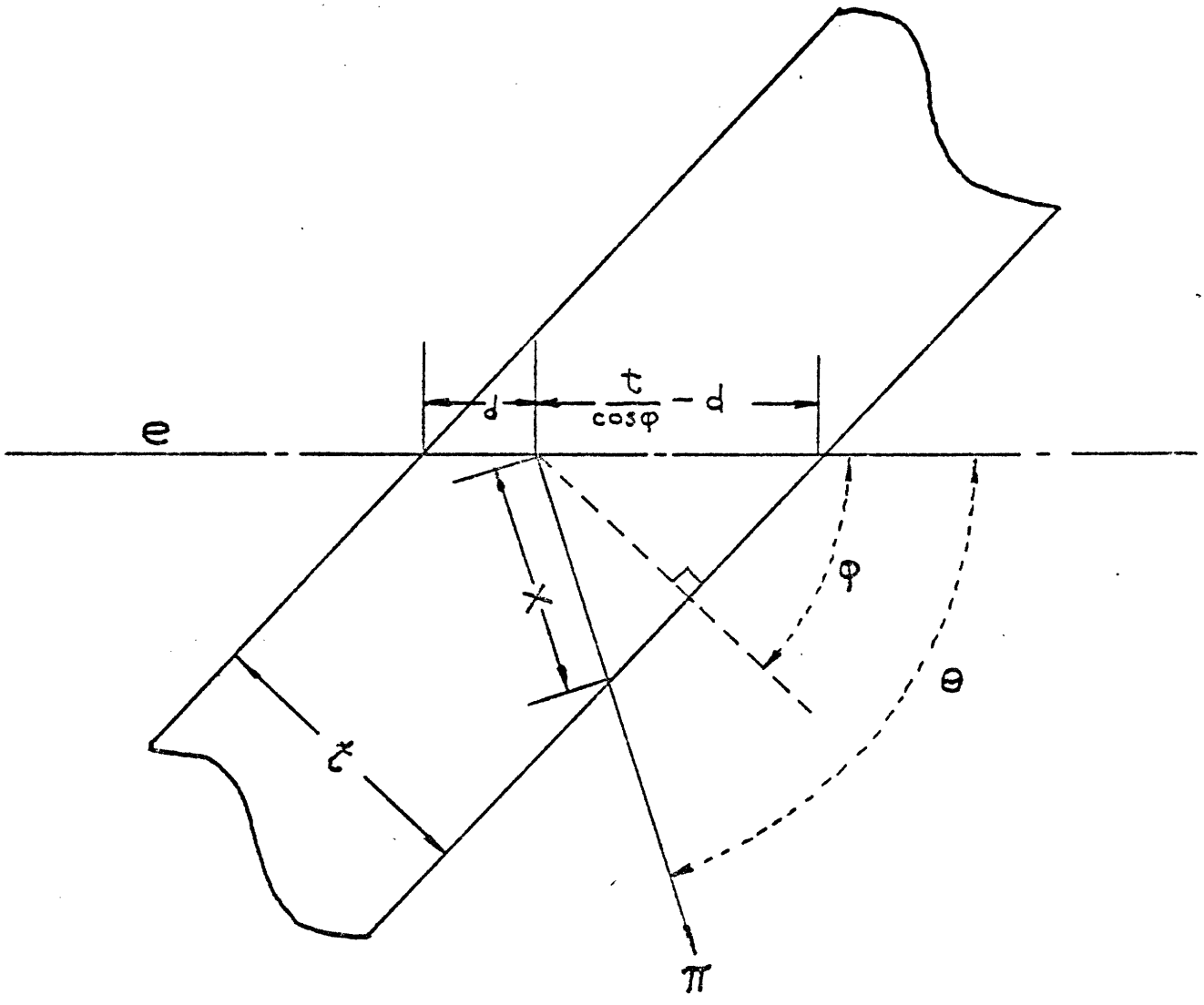

Fig IV-5

target angle at half the scattering angle, since the pion and electron energy losses are almost equal, but were forced to use the reflection mode in a preliminary run at 140° scattering angle to avoid hitting the edge of the targets. Fig. Iv-6 shows the virtual and self-bremsstrahlung spectra for a typical case with the target resolution folded in. It can be seen that the spectrum shape with no radiator is thus dominated by the contribution from the virtual photons.

This in principle gives us all the information needed to predict the shapes of the pion spectra, but in practice a substantial contribution from muons must be considered, as will be done in the next section.

IV-5 Muon Contamination

One of the most difficult backgrounds to cope with is that from the muons arsing from the pions that decay in flight. It will be seen that these muons will distort the ideal pion spectra shapes derived in the previous section.

In the Bates Energy Loss Spectrometer, the principle problems come from decays in the first and last 3.55 meter drift spaces. The muons arising from decays in between are found to be relatively harmless as they cannot have the same momentum as the original pion without suffereing a substantial angle change and are hence mostly lost to the baffles and yokes or do not hit the wire chamber within the angular acceptance limits.

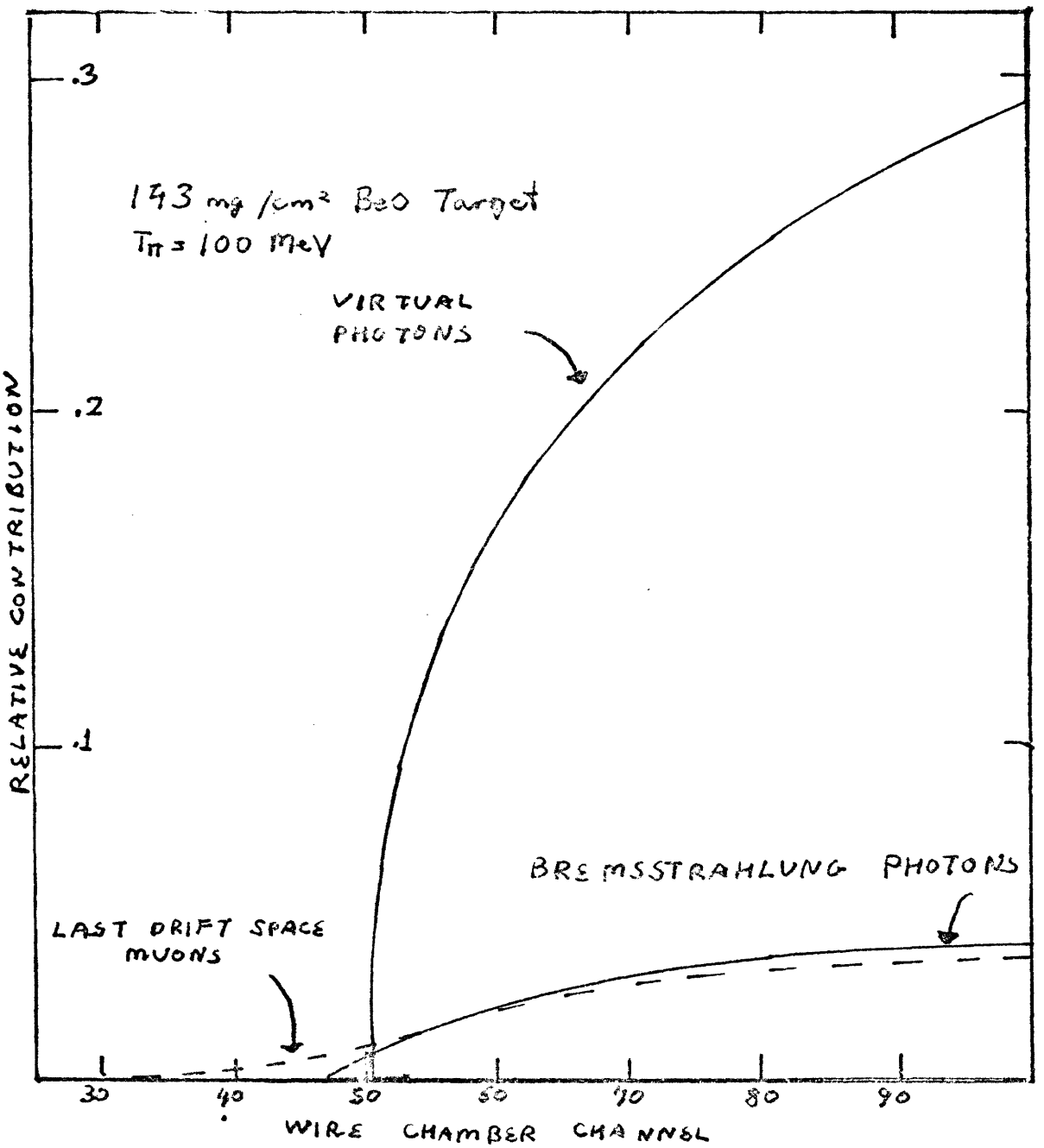
.3
.2
.1
143 mg/cm² BeO Target
Tπ = 100 MeV
VIRTUAL PHOTONS
BREMSSTRAHLUNG PHOTONS
LAST DRIFT SPACE MUONS
RELATIVE CONTRIBUTION
30
40
50
60
70
80
90
WIRE CHAMBER CHANNEL

Fig IV-6

A. Last-Drift-Space Muons.

The pions that decay in the last drift space are easier to deal with than those from the first drift space. Since the wire chamber rejects events that have angles greater than 80 mr in the momentum plane, the muon yield pretty much follows the pion yield in shape, although considerably reduced in magnitude, even though the muons have quite different momenta than the original pions, being mostly centered in two momentum peaks corresponding to forward and backward center-of-mass decay. A short subroutine was written and incorperated into the calucation of the pion shapes used in the fitting program. The calculation integrates over decay distance from the chamber, pion angles, and muon center-of-mass decay angles and only keeps those events that pass through the counters with acceptable angles and with enough energy to trigger the Cerenkov detectors. The contribution to a typical endpoint spectrum is shown as the dashed line in Fig. IV-6. The calculation was checked by applying software cuts to a hydrogen spectrum to select mostly muons and was found to be in good agreement both in shape and magnitude when a flat background level was subtracted. This flat background is attributed to muons from the first drift space, for reasons that we examine in the next sub-section.

B. First-Drift-Space Muons.

Muons that come from the first drift space decays are

more difficult, as they arise principally from pions six to ten MeV lower in momentum than those pions that have the same momentum as the emerging muons. This can be easily understood, since in order to make it through the slits (which are two meters from the target) and the magnetic optics the pions must decay without changing their angle more than a few degrees. This corresponds to either backwards or forwards center-of- mass decay angles, but only the forward decay increases the particle momentum. Since the number of pions at a given angle increases strongly with deacreasing momentum, the relative contribution in the endpoint region can be quite large.

To better understand the problem, a simple Monte-carlo program was written which integrates over an assumed pion momentum distribution and calculates the wire chamber spectrum for a given value of the central spectrometer momentum. The two pion angles are selected at random, as are the decay distance from the target and the two center of mass decay angles. The angles were transformed to the lab system and the lab muon momenta calculated using kinematical relations. It was checked that the muon (or pion) passed through the slits, which were set at 2" in the scattering plane and 10" in the azimuthal plane, and that the muon did not hit the magnet pole pieces or yoke. The known first order matrix elements for the rest of the system were then used to transport the

muon to the wire chamber, where it was checked that it was within the physical limits of the counters and had less than an 80 mr scattering angle (since events with greater angles are rejected in the software).

The results for a central momentum of 200 MeV for two different assumed pion distributions are shown in Fig. IV-7. The physical limits of the wire chamber are indicated by the vertical dashed lines. The number of muons has been normalized such that the relative ratios of pions to muons is that which should actually be observed. We see from the figure that the pion spectrum is, to first order, smeared out and shifted to higher momenta. The problem is that we did not measure the pion yields at the lower momenta required to accurately subtract the corresponding muons from our endpoint spectra, since the inportance of this correction was not realized at the time of the production run. Fortunetely, it turns out that a straight line is a reasonably good fit to the muon backgrounds when the relatively poor statistics we have on the backgrounds are taken into account. For hydrogen, which only has one state, the background is observed to be almost flat, as one would expect from the results shown in Fig. IV-7. But, for oxygen, with many closely spaced final states, the slope is quite steep, as can be seen in the two representative endpoint spectra shown in Figs. IV-11 and IV-17.

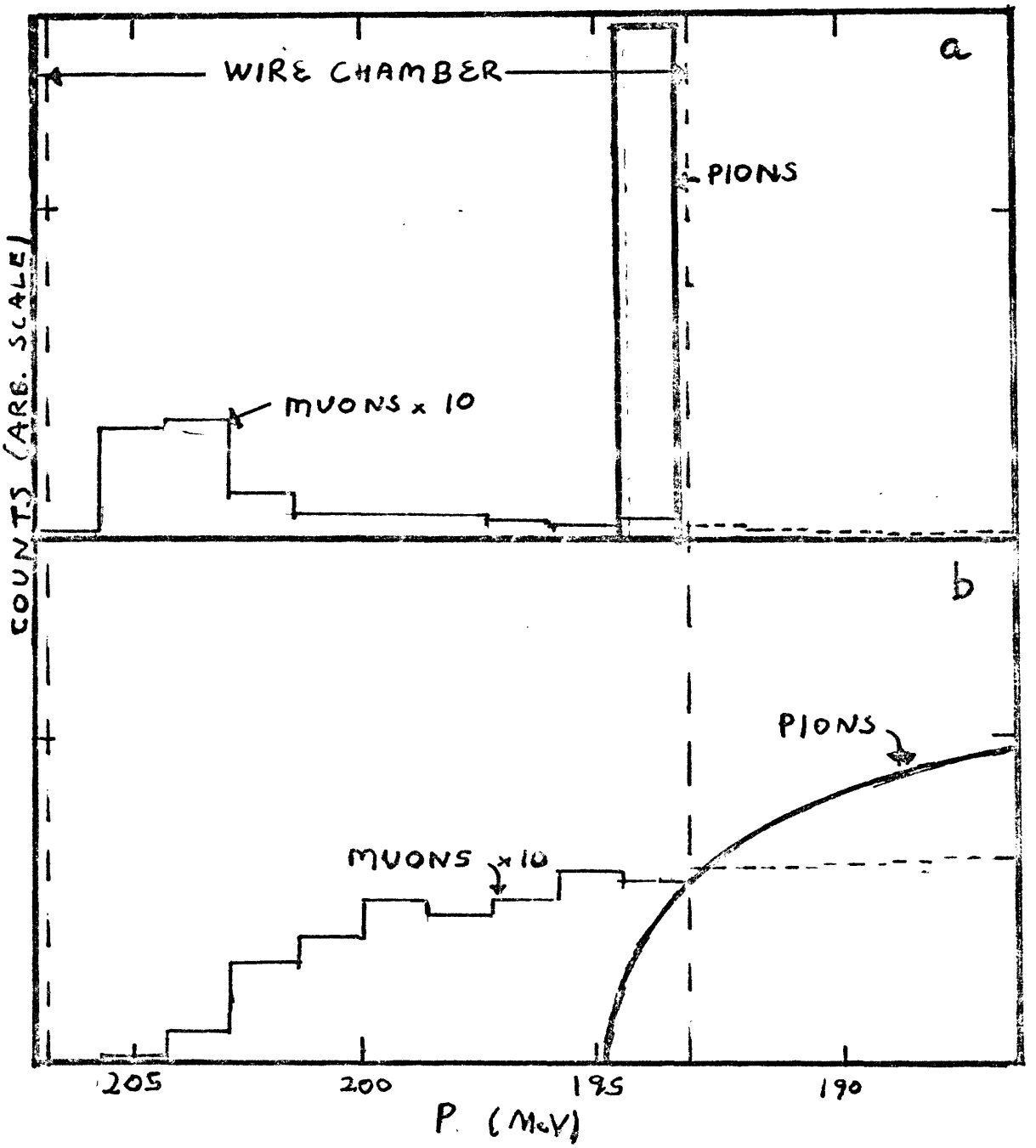
a
WIRE CHAMBER
PIONS
MUONS x 10
COUNTS (ARB. SCALE)
b
PIONS
MUONS x10
205
200
195
190
P (MeV)

Fig IV-7

C. Residual Backgrounds.

It should be noted that although we can eliminate almost all of the positron background with software cuts, the remaining backgrounds are larger than expected from muons alone. This can be understood by looking at higher energy runs, where after cuts are applied that remove almost all pions, muons, and positrons, a residual background is noted with a relatively small total pulse height, similar to the pulse height of pions at the lower energies. This background is found to be quite flat and can best be attributed to debris from electrons which are deflected upwards into the yoke of the magnets and shower down onto the detectors. Appropriate baffling could cure this problem and should be incorporated into the new pion spectrometer design.

D. Impact on New Pion Spectrometer.

We also note that first-drift-space muons will be much less of a problem in the new spectrometer due to the much shorter first drift space of only .5 meters before the first quadrapole. However, decays in the quadropoles cannot entirely be neglected, so that detailed calculations should be done to make sure that pion spectra are taken over a wide enough momentum range to subtract the correspoding muons. A better total pulse height analysis system, such as an aray of lead glass detectors, could do much to eliminate unwanted muons as well.

IV-6 Beam Energy Calibration and Electron Efficiencies

A. Beam Energy Calibration.

In order to measure the electron incident energies more accurately than was given by the nominal machine settings (which are only accurate to about 1%), the elastic electron scattering from a 143 mg/cm^2 BeO target was used.

The first thing that was checked was the nominal dispersion constant for the wire chamber, which is .068% per coarse channel. This value gave very good predictions for the relative positions of the oxygen ground and three first exited states and for the beryllium ground and (when seen) first exited state.

Since a 5/16" slab of aluminium was placed in front of the chamber to reduce the singles rates from protons when the spectrometer was in the positive polarity mode, our resolution was not terribly good (about 3.5*10-4), so we could not seperatly fit the beam energy and spectrometer constant (ratio of central momentrum to magnetic field constant) separatly. Therefore, we assumed that the nominal value of the spectrometer constant (66.12 MeV/KG) was correct and fit the beam energies to the oxygen elastic peaks using the relation

IV.8 $$e' = \frac{e}{(1 + e/m\,(1 - \cos\theta))},$$

where θ is the scattering angle, e is the energy of the incident electron, e$'$ is the energy of the final elec-

tron, and m is the mass of the struck nucleus.

The results are shown in Table IV-1, where it can be seen that the beam energies were found to be significantly lower than the values given by the machine operators, the deviation increasing strongly at higher energies. This is consistent with the observations of other experimenters, but depends strongly on the current position of the beam defining slits, which is periodically subject to change.

It should be noted that if we had used a different value of the spectrometer constant, the derived beam energies would have been different, but the endpoint channel number for the pion spectra would remain almost unchanged, since the kinematic change in photon energy with pion energy is very close to one. The exception to this statement is hydrogen, where dk/dT varies from 1.7 to 2.1 in the delta region. However, when the hydrogen spectra were fit with the endpoint channel as a free parameter, the average shift for all runs was found to be consistent with zero, implying that the nominal value of 66.12 MeV/KG, which was determined by P. Dunn at 100 MeV by supperimposing hydrogen and carbon peaks, is correct for our purposes.

B. Detection Efficiency for Electrons.

The elastic oxygen peaks were also used to measure the efficiency of the spectrometer and thus check such factors as beam monitoring toroid calibrations, target

E(MeV)	B(KG)	e'nom	e'meas	shift(MeV)
360.	531.12	351.04	348.49	-2.55
340.	502.11	331.94	324.40	-2.55
320.	474.70	213.80	310.83	-1.97
301.	445.59	294.57	242.82	-1.75
283.	419.40	277.25	276.37	-0.88
260.	285.87	255.07	254.03	-1.04
253.	375.64	248.31	247.26	-1.05
238.	352.67	233.77	232.47	-0.81
230.	342.06	226.03	225.48	-0.58

Table IV-1. Measured shifts from the nominal beam energies using elastic electron scattering peak in oxygen. E is nominal beam energy, B is spectrometer magnetic field, e'nom is the nominal elastically scattered electron energy, e'meas is the measured value, and shift is their difference.

thicknesses, solid angle, and wire chamber and Cerenkov detector efficiencies. The number of counts in each was intergrated up to the beryllium peak, then multiplied by the dead time corrections. Radiative tail corrections were applied using the values calculated with the program RADCOR of Claude Williamson, and were on the order of twenty percent, mainly arising from the Schwinger correction. Cross sections were extracted using a solid angle of 3.32 msr and the known target thickness and angle as well as the number of intergrator counts for each run. They were then compared with the known cross sections, which were calculated with the program ELASTN of M. Hynes, in which the form factor is fit to the world's supply of data with a better than 3% reliability. The resulting efficiencies are plotted in Fig. IV-8, and are found to be consistent with a 100% efficiency for electrons in the experimental setup that we used.

IV-7 Quasi-Free Pion Production

In order to measure the flatness of the wire chamber response (the so-called white spectra) and to get an idea of the efficiency versus energy response of the system for pions, quasi-free pion production from a 200 mg/cm^2 carbon target was measured at two incident electron energies (360 and 320 MeV) for various pion momenta.

A. White Spectra

As far as white spectra are concerned, we found in

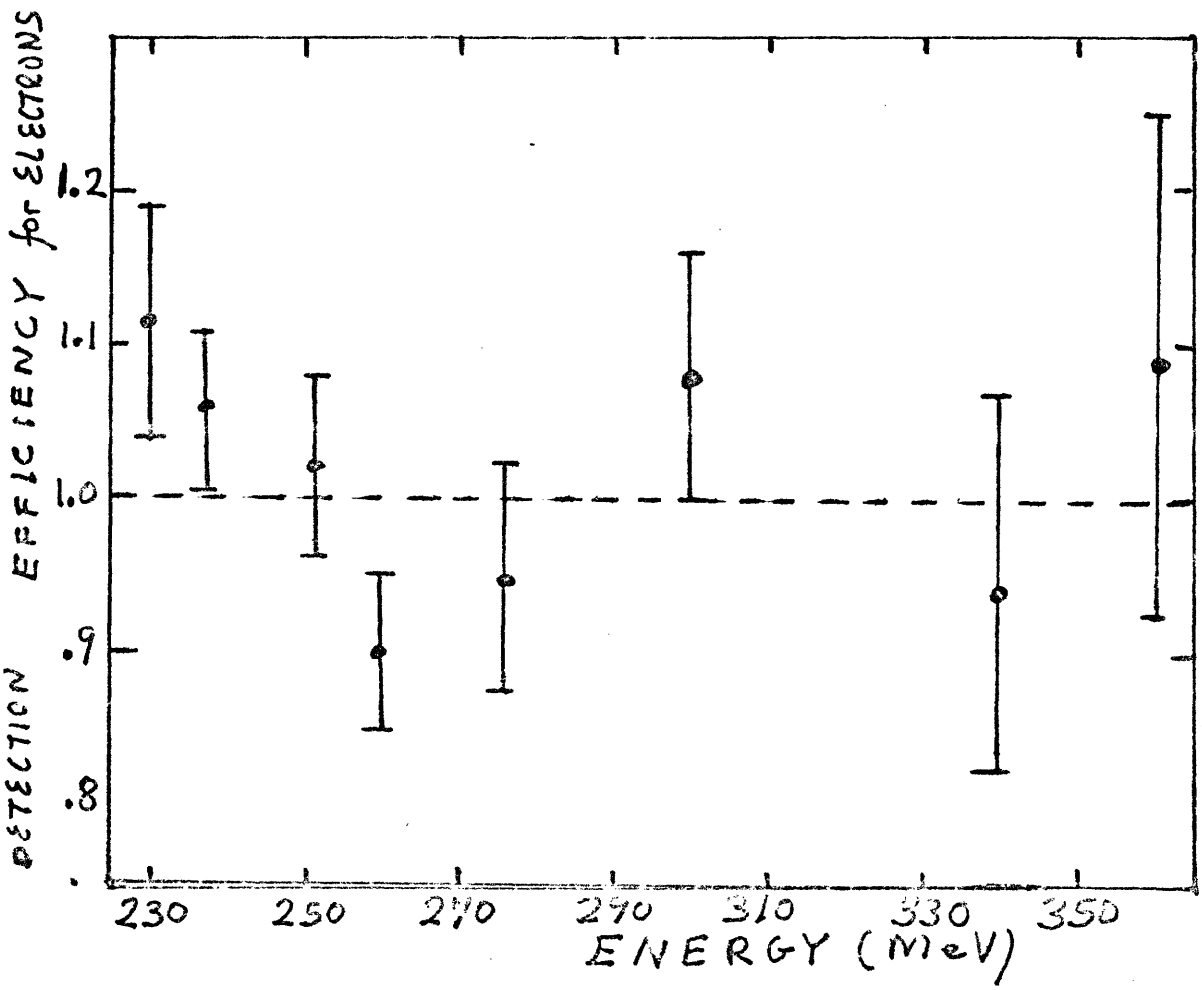
DETECTION EFFICIENCY for ELECTRONS
1.2
1.1
1.0
.9
.8
230
250
270
290
310
330
350
ENERGY (MeV)

Fig. IV-6

previous runs that with the first two Cerenkovs demanded in the coincidence system (C1-C2 trigger), the wire chamber response showed a definite decrease on the low momentum side corresponding to the increased distance from the phototubes in the Cerenkov detectors. In the production run this problem was eliminated by using only the transverse array and the first Cerenkov counter in the trigger requirement (C1-TAC trigger). The slopes of the yields were then consistent with those predicted by the model in the following paragraph. Thus, by using the C1-TAC trigger for the lowest few pion energies, we did not have to modify the production data with a sloping white spectrum.

B. Comparison with Other Experiments.

In order to get some ideas about the efficiency of the system for pions, count rate predictions were made using the data of the Bonn group for the quasi-free production of charged pions from carbon (EY78). Their data was taken with tagged photons in 20 MeV photon bins, 30 degree lab angle bins, and 10 MeV pion energy bins with error bars ranging from 50% near the kinematic limit to 10% at the peak of the quasi-free spectrum. In order to interpolate their data to the desired energies and angle, it was parametrized in terms of simple functions. After integrating over the virtual photon flux for the cross sections at a given pion energy, the cross section was

multiplied by the number of target atoms, the number of incident electrons, the spectrometer solid angle, the pion energy acceptance of the wire chamber, and the pion decay factor to arrive at the predicted number of counts. The data points were corrected for dead time losses and cuts were used to eliminate electrons and most muons.

Comparison between the two is shown if Fig. IV-9. It can be seen that the overall agreement is reasonable, with the efficiency falling off at lower pion momenta due to the decreased Cerenkov responce, especially in the case of C1-C2 triggering. While the efficiencies one could extract from these comparisons are generally somewhat larger than those found from the hydrogen normalization (see next section), they are not inconsistent when the uncertainties in the predictions based on the Bonn data are taken into account. For this reason the more reliable hydrogen data were used in the final efficiency determinations.

C. Comparison of Different Triggers.

It is of interest to compare more quantitavely the effects of including the second Cerenkov in the trigger requirement. For this reason we have plotted the ratio of the number of counts for C1-C2 triggering versus C1-TAC for the same number of incident electrons in Fig. IV-10. It can be seen that the ratio goes to zero for 170 MeV pions, as one would expect from the energy losses in the proton absorber and first Cerenkov. One also notes that

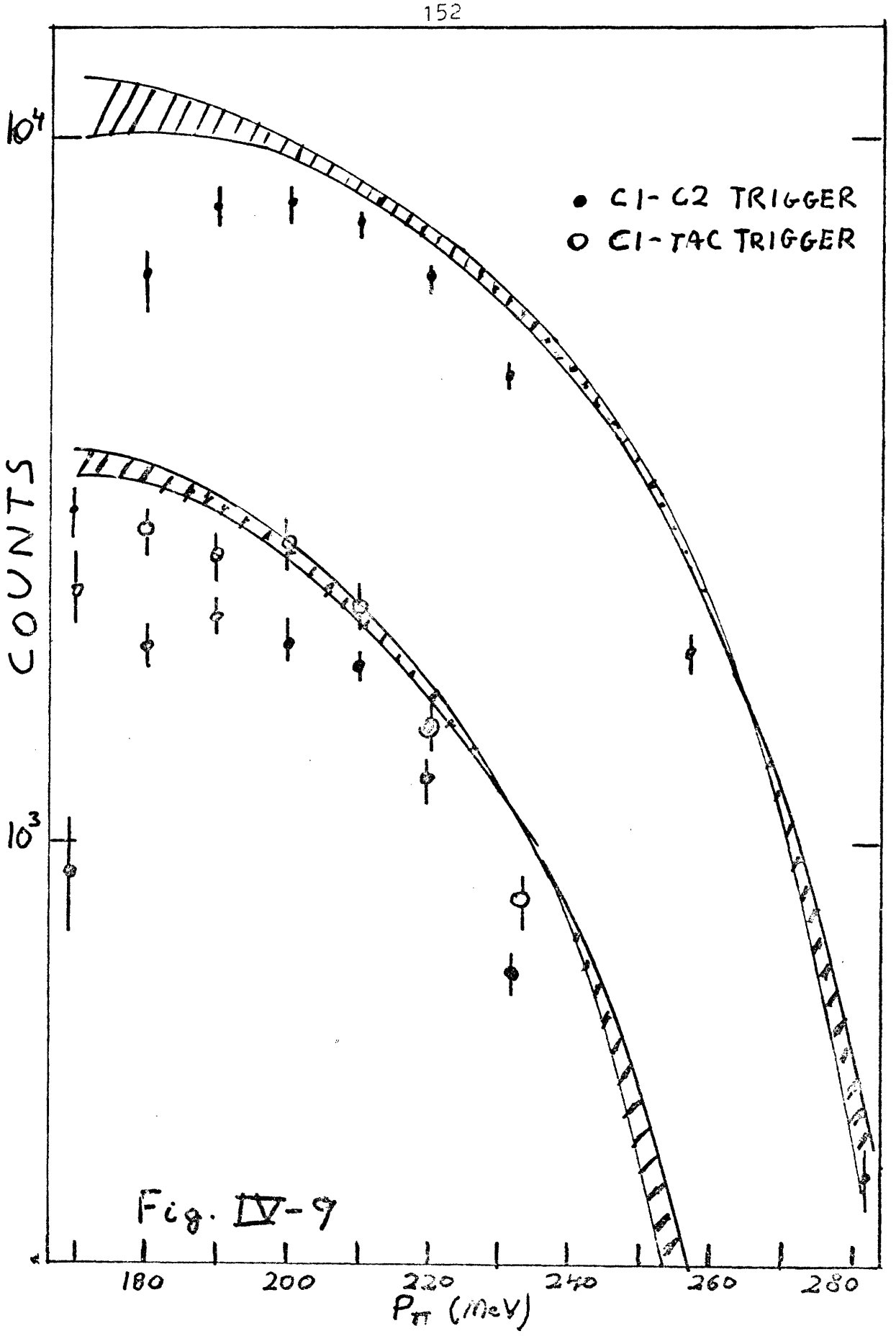
10⁴
10³
COUNTS
• C1-C2 TRIGGER
o C1-TAC TRIGGER
180
200
220
240
260
280
P_π (MeV)

Fig. IV-9

the maximum ratio is less than 100% due to pion absorption in the first counter. This is shown as the dashed line, which is calculated using the known inelastic and true absorption cross sections for carbon in the delta region, measured by Navon et al (NA79). The elastic cross section was not included as it is very forward peaked. This calculation is an overestimate since some of the inelastically scattered pions will still have enough energy to radiate in the second counter, but seems to give a good account for the observed ratios.

We conclude from the figure that the second Cerenkov counter should only be included in the trigger requirement for energies above 105 MeV, where the ratio attains the maximum value allowed from the effects of pion absorption in the first counter. While including the second counter inevitably implies some loss in efficiency, this is offset by the better room background rejection obtained with two counters in coincidence.

IV-8 Data for $p(\gamma,\pi^+)n$ and Absolute Efficiency

This section describes the manner in which the well studied $p(\gamma,\pi^+)n$ reaction was used to determine the absolute detection efficiency of the apparatus for pions as a function of energy.

A. Targets.

The target used was a rotating sheet of polyethylene with a thickness of 50.2 mg/cm^2 and a diameter of 8.78 cm.

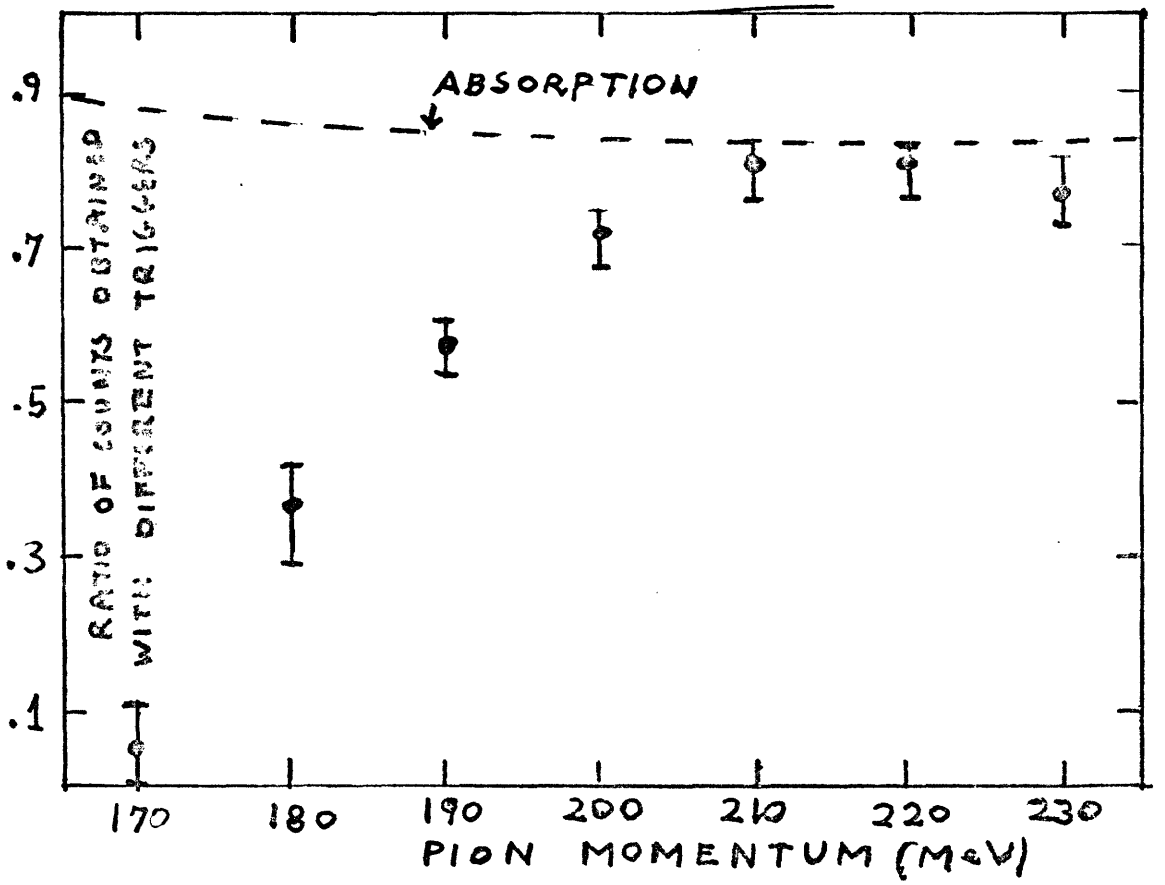
ABSORPTION
RATIO OF COUNTS OBTAINED WITH DIFFERENT TRIGGERS
.9
.7
.5
.3
.1
170
180
190
200
210
220
230
PION MOMENTUM (MeV)

Fig. III-10

It was noticed that the target had turned brown and suffered some deformations due to the high electron flux, even though we ran with only 3 mA peak current and less than 10 μA average current when using this target (normally we ran with 50 μA average current). Fortunatly, no melting occured, so that the target uniformity was fairly well preserved, and no detectable change in the total target weight was observed. For each run the carbon contribution was subtracted using a 48.1 mg/cm^2 carbon target. This contribution is large because the threshold for carbon is so much lower than for hydrogen, at least at 90°, and was almost as large as the hydrogen yield at a few MeV above threshold.

B. Kinematics and Fitting Method.

Due to the large recoil energy for pion production from hydrogen at 90°, we were only able, with the maximum beam energy of 360 MeV, to measure up to pion energies of 127 MeV, as can be seen by examining the kinematics graph shown in Fig. IV-1. The results shown in the graphs were calculated using the relation that

$$p_\pi = \left(-b - \sqrt{b^2 - 4ac}\right) / 2a$$

IV.9

$$a = k\cos\Theta / (m_i + k)^2 - 1$$

$$b = k\cos\Theta \left(m_i^2 - m_f^2 + 2m_i k + m_\pi^2\right)^2 / (m_i + k)^2$$

$$c = \left(m_i^2 - m_f^2 + 2m_i k + 2m_\pi^2\right)^2 / 4(m_i + k)^2 - m_\pi^2,$$

where k is the photon energy, M_i and M_f are the masses of

the initial and final nuclei, and θ is the scattering angle. Knowing the elctron energies measured from electron scattering, the corresponding maximum photon energies are found by subtracting one electron mass. The endpoint channel in the wire chamber is then found using the known magnetic field and taking into account the energy loss in the target. The pion energy in each coarse channel is then calculated relative to the endpoint energy using the known dispersion, and the corresponding photon energies and photon energy width per channel are evaluated using the relation that

IV.10 $$\frac{dk}{dT_\pi} = \frac{(m_i - \beta k \cos\theta + k)}{(m_i + p_\pi \cos\theta - E_\pi)}, \quad \beta = \frac{p_\pi}{E_\pi}.$$

As mentioned before, this is a number on the order of two for hydrogen, but is very close to one for heavier elements. The pion spectrum shape is then evaluated as described in the previous sections, and is fit with a flat background to the actual data. Options exist to allow for a slope in the background and for a shift in the endpoint channel. The program CURFIT described by Bevington (BE69) was used to find the optimal values of the parameters.

A typical spectrum is shown in FIg. IV-11. It can be seen that the fit is good given the error bars, as confirmed by χ^2 values less than 1.2 for all the runs we took. The cross sections in μb/sr were found by dividing the fit parameter for the shape function by the number of

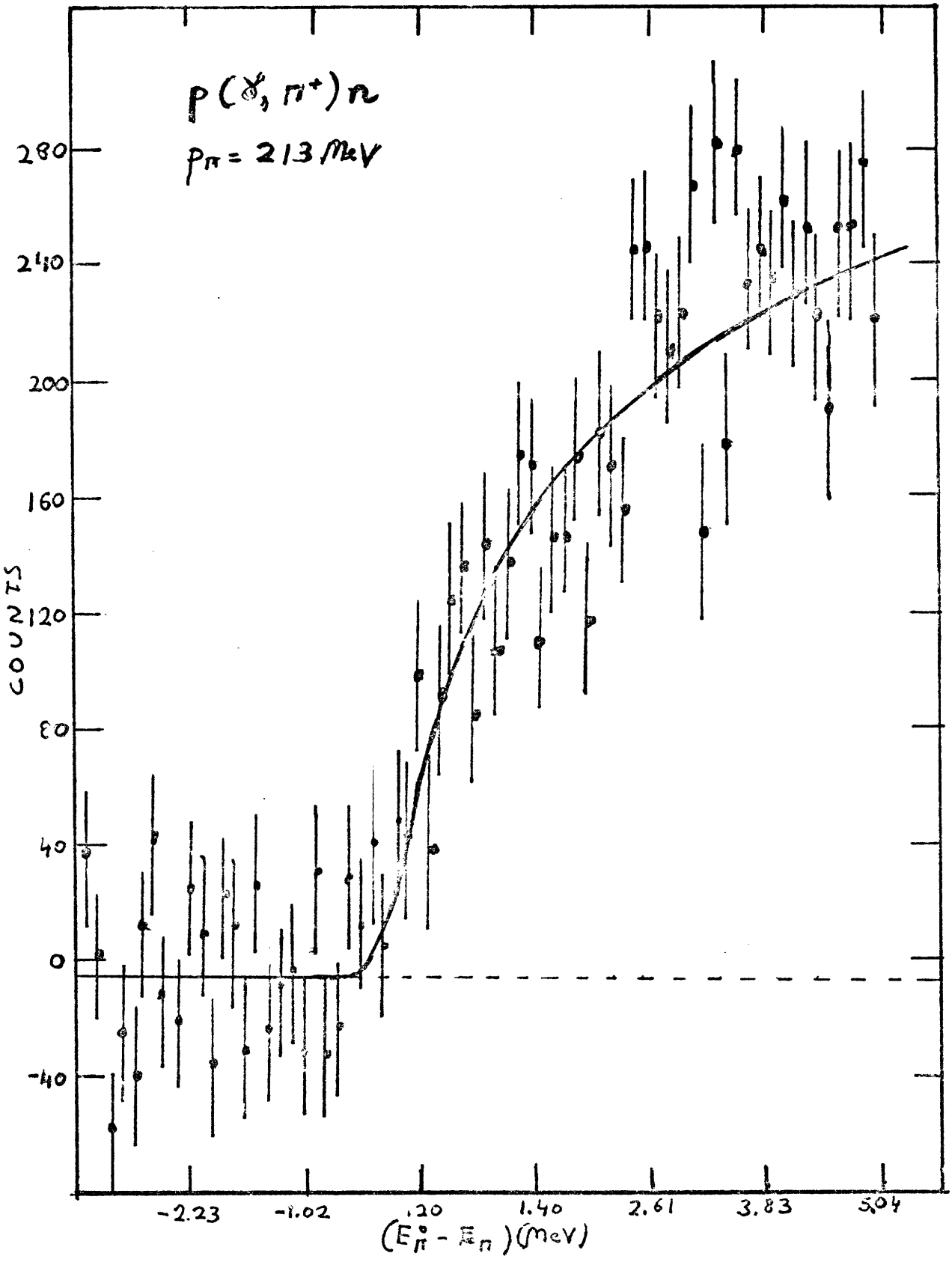
p(γ, π+)n
pπ = 213 MeV
280
240
200
160
120
80
40
0
-40
COUNTS
-2.23
-1.02
.20
1.40
2.61
3.83
5.04
(Eπ° - En) (MeV)

Fig IV-11

target atoms, the number of incident electrons, the solid angle, and the pion decay factor. The first three factors were derived in the same way as when we calculated the electron efficiencies (see section IV-6), so that we can be certain about the constants needed in their evaluation. The pion decay factor is given by

IV.11 $$e^{-\left(\frac{L}{\beta\gamma c\tau_0}\right)} \quad \text{with } \beta = \frac{p_\pi}{E_\pi} \text{ and } \gamma = \frac{1}{\sqrt{1-\beta^2}}$$

where L is 11.6 meters and τ_0 =26.0 nsec.

C. Data Analysis

It was found that including a shift in the endpoint energy did not significantly alter the results, with the average shift being 1.2±2.2 channels. As mentioned before, this confirms our choice of 66.12 MeV/KG as the spectrometer constant. Including a slope in the residual background tended to decrease the cross sections by 5% to 10%, except for the lowest energy where it made the cross section 10% higher. Since no improvements in the χ^2 values were found by including the slopes, and the change in the results were less than the error bars on the points, the values without the slopes were used in the final efficiency evaluations.

In each case the data were analyzed both with and without the same total- pulse-height and timing cuts as were used to analyze the final oxygen and boron endpoint spectra at the corresponding pion energies. The ADC cuts

were chosen at the valleys between the positron and pion peaks. Knowing the energy loss for pions in lucite, the TDC information was used to require that the last N counters not fire (since the pions would no longer have enough energy to radiate), where N was three for the lowest energy, two for the next two energies, and one for the two highest pion energies. It should be noted that the positron background was relatively small for the hydrogen spectra due to the much larger cross sections involved compared to photoproduction from complex nuclei. The reduction in the extracted cross sections was found to be between 6% and 11% when the cuts were used, since inevitably a part of the pion spectra were cut into as well.

D. Extraction of Efficiencies.

The observed differential cross sections, (with dead-time corrections applied), are tabulated in Table IV-2. They are then compared to the known values to derive the efficiency. The theoretical values were taken from the dispersion relation calculation of Berends (BE67), which is fit to the world's supply of data. The calulated curves were used as they give a good fit, on the average, to the existing data, whereas systematic errors in the data make it scatter by as much as twenty percent when comparing the results of different experiments, even though the error bars on the points themselves are generally less than five percent. Error bars on the calculated values are also

given by the authors, and range from 7% to 10%. Using simple kinematics, one finds that the center-of-mass angle is 107^{o} in our energy range for a lab angle of 90^{o}, and the Jacobian to transform the cross sections to the lab system is between .91 and .93 for lab photon energies from 283 to 360 MeV. The efficiencies are found by dividing the experimental cross sections by the theoretical ones, and the results are plotted in Fig. IV-12. Note that the first two values were taken with the C1-TAC trigger. The efficiency drops as the second counter is added to the trigger and again quickly climbs with increasing energy. The solid line shows the exterpolated values used to normalize the higher energy data, with estimated errors given by the dashed lines. The values are also tabulated in Table IV-2.

It should be noted that the maximum value for the efficiency at the highest pion energies was chosen to be close to 100%. Based on the fact that some of the pions are absorbed in the first Cerenkov counter and therefore cannot fire the second counter, which is also included in the triggering requirement, one might expect a maximum value that is somewhat less than 100% (see Fig. IV-10). But, as will be explained in the next section, this is offset by the observation that the virtual spectrum used to extract the cross sections was too small by a factor of 1.27. Using too small a virtual spectrum would, in prin-

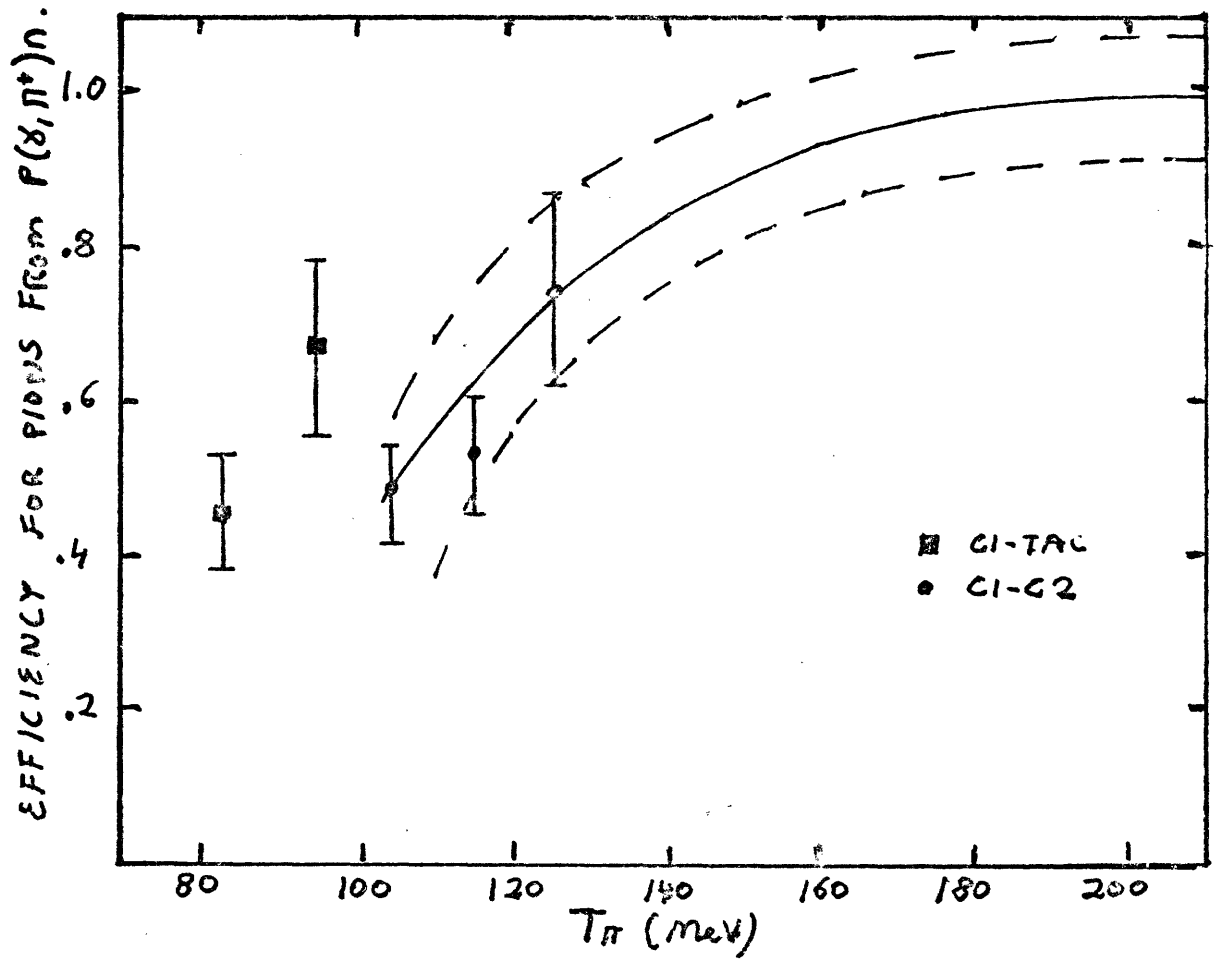
EFFICIENCY FOR PIONS FROM P(γ,π⁺)n.
1.0
.8
.6
.4
.2
80
100
120
140
160
180
200
Tπ (MeV)
C1-TAC
C1-C2

FIG IV-12

E_γ	T_π	P_π	$d\sigma/d\Omega$exp	$d\sigma/d\Omega$BE67	efficiency
283.	84.	175.	8.4(1.2)	18.4(1.3)	.46(.073)
301.	94.	187.	13.(2.0)	20.5(1.4)	.67(.109)
320.	104.	200.	9.8(1.0)	16.9(1.5)	.49(.056)
340.	115.	213.	8.8(1.0)	16.9(1.5)	.49(.056)
360.	126.	226.	9.2(1.2)	12.3(1.1)	.75(.118)
		245.			.81(.110)
		265.			.94(.110)
		285.			.97(.110)
		305.			.99(.110)

Table IV-2. Values of detection efficiency derived using the $p(\gamma,\pi^+)$ n reaction. Error bars are given in parentheses. E_γ is the endpoint photon energy, T_π is the pion kinemtic energy, $d\sigma/d\Omega$exp is the experimentally measured cross section, $d\sigma/d\Omega$BE67 is the theoretical one of BE67, and the efficiency is found by taking theri ratios and extrapolating to higher energies.

ciple, give efficiencies larger than 100% when compared with the correct photoproduction cross sections. The two effects taken together, one which would lower the maximum possible efficiency that could have been obatined by the analysis method used, and one that could have raised it, work together to give once again a maximal detection efficiency that should approach 100% as the pions become sufficiently energetic to always trigger the Cerenkov counters in the absence of pion absorption.

IV.9 Real-to-Virtual Ratios.

Most of the data we have taken has really been electroproduction, not photoproduction, but we have assumed that the two cross sections are equal in using a virtual photon spectrum to parametrize our electroproduction yields. We have already seen that the assumed shape for the virtual spectrum gives very good fits. But in order to check its magnitude we ran in a few cases with a radiator in front of the target so that we could have mostly real photons.

Two radiators were used, a 94 mg/cm^2 Ta radiator for which we had about as many real photons as virtual ones, and a 235 mg/cm^2 Ta radiator for which the real photons outnumbered the virtual ones by a factor of three. In the case of hydrogen, only the thicker radiator was used, at a beam energy of 340 MeV. When the results are compared using the same cuts and fitting options, it is found that

the cross sections with the radiator are consistently smaller than those without. We therefore define an effective strength factor, F, by which the virtual spectrum should be multiplied to give consistent results with the real spectrum. The value of F for hydrogen is found to be 1.27±.08, regardless of the cuts or fitting method used, although the error is almost twice as large if the backgrounds are allowed to have a slope.

Real-to-virtual ratios were also measured for the $^{16}O(\gamma,\pi^+)^{16}N$ reaction at pion momenta of 200 and 226 MeV in the endpoint region using both radiators. Very little information was gained from the thin radiator as the size of the effect we are looking for is smaller than the error bars on the points. But, with the thick radiator it was possible to notice a significantly smaller cross section for real photons. The average value of F for all oxygen runs was found to be 1.17±.11. This is consistent with the value found by Nick Paras (PA79) for the endpoint regions in the oxygen and beryllium (γ,π^+) reactions of 1.28±.08.

We note that this is the first measure of F for hydrogen in the endpoint region. A number of the size we have found is not surprising, for while all the multipoles have a similar shape in this region, we are only using the electric dipole componant and have assumed plane waves for the electron. It would be interesting to measure F as a

function of energy from the endpoint, especially given the measurements of WI79 that show that at 33 and 52 MeV from the endpoint the values of F are .96±.08 for 17 MeV pions and .99+.08 for 30 MeV pions for hydrogen. The beam energy used in these measurements was 230 MeV. More precise experiments will definitly require this knowledge of how F apparantly changes from 1.27 in the endpoint region to essentially 1.00 only 30 to 50 MeV away.

We conclude that all the endpoint cross sections that we have derived for electroproduction will be high by 1.25±.06 (taking the average value of all measurements). Since this problem affects the hydrogen data used to extract the pion detection efficiencies as well as the production data from oxygen and boron, the efficiencies in the previous section will still give the correct photoproduction cross sections when applied to the heavier elements to derive the final differentail cross sections for $^{10}B(\gamma,\pi^+)^{10}Be$ and $^{16}O(\gamma,\pi^+)^{16}N$.

IV-10 Results for $^{10}B(\gamma,\pi^+)^{10}Be$.

We now discuss the final results for the $^{10}B(\gamma,\pi^+)^{10}Be$ cross sections at 90^0 for pion energies from 84 to 183 MeV. The ground state of ^{10}B is a 3^+ state, and the observed states in the residual ^{10}Be nucleus are both the ground state (0^+) and the first exited state (2^+). The analog states in ^{10}B are at 1.47 and 5.11 MeV respectively. (AJ74) These states are easily separated due to

their large spacing (3.35 MeV between the ground and first exited state, and 2.65 to the next state). Higher states are very closely spaced and cannot be separated with our present resolution, so no attempt was made to examine them.

The next subsection describes the manner in which the data were analyzed to obtain the differential cross sections for the two lowest lying states in ^{10}Be, following which the results will be interperted in light of the available information and comparison made with a still preliminary calculation.

A. Data Analysis

The target used in these runs was made of 116 mg/cm^2 powdered boron of 92% purity sandwiched between two 23 mg/cm^2 ^{12}C foils and mounted in a standard electron scattering aluminum target holder. Since the thresholds for both carbon and ^{19}B are more than 6 MeV higher than for ^{10}B, they will not contribute to our pion yields.

A typical spectrum using this target is shown in Fig. IV-13. The beam energy was 230 MeV, and the pion energy was 84 MeV. The running time was about three hours, with an average beam current of 45 μA and a peak current of 6 mA. In this case the slope of the background was close to zero due to a cancellation between the increasing muon yield and the decreasing detection efficiency with decreasing momentum. In all of the other cases, positive

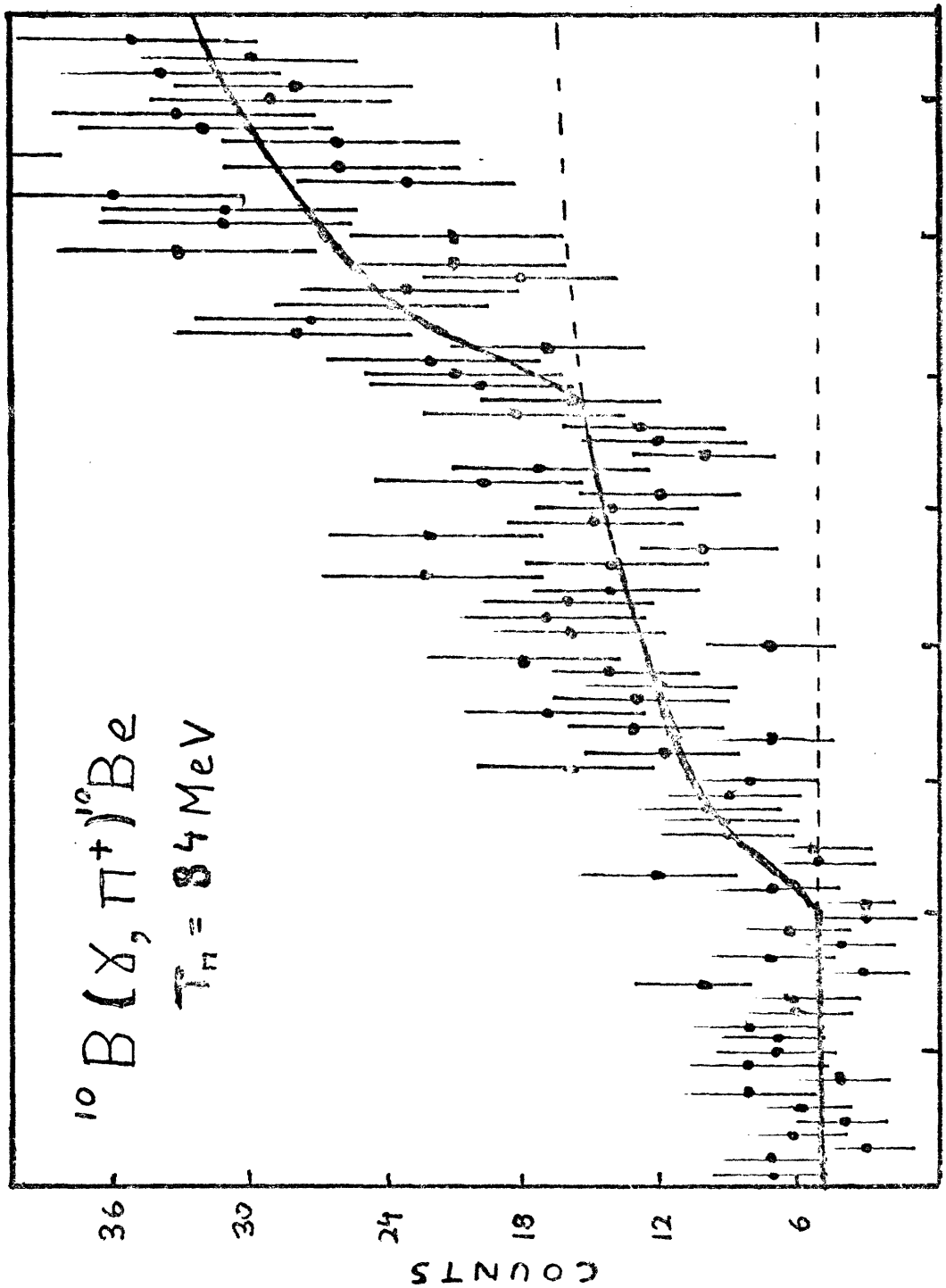
$^{10}B(\gamma, \pi^+)^{10}Be$
$T_\pi = 84$ MeV
COUNTS
36
30
24
18
12
6
-2.90
-1.09
-0.18
0.72
1.63
2.54
3.45
4.36
5.26
$(E_\pi^\circ - E_\pi)$ (MeV)

Fig IV-13

slopes to the backgrounds were needed to give good fits to the data. Allowing the endpoint channel to shift from the values calculated using the beam energies determined from elastic electron scattering showed no improvements in the fits, with the average shift found to be consistent with zero.

Total pulse height and timing cuts were important in reducing the almost flat positron backgrounds. The same values were used as in the efficiency determination using hydrogen. The positron background was largest at the lowest energies (as much as a factor of two), while at the highest energies the main background was found to come from small total-pulse-height events presumably associated with debris from electrons scattered into the magnet yokes. This would be expected since the positron background falls off very fast with increasing momentum transfer q (somewhere between q^{-4} and q^{-8}), whereas the pion yield only decreased one order of magnitude over the energy region spanned by the present expreiment.

The extracted cross sections were corrected for dead time and divided by the efficiency to arrive at the final values plotted in Fig. IV-14. The excited state is indicated by the solid squares, the ground state by the solid circles. Also shown, as the open squares and circles, are the preliminary data of D. Rowley et al (RO79) at lower pion energies taken with the Bates Low Energy Pion Spec-

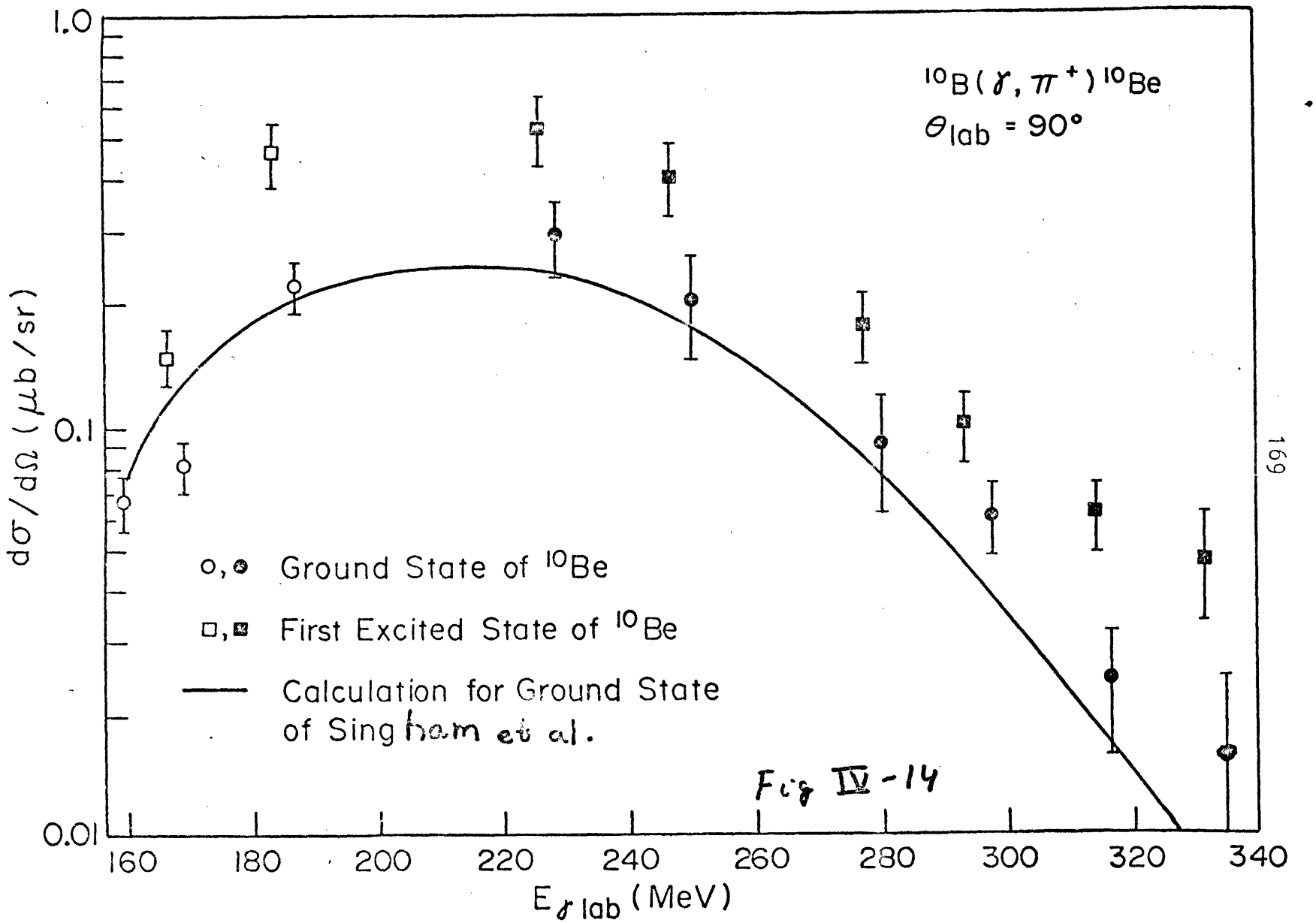
$^{10}B(\gamma, \pi^+)^{10}Be$
$\theta_{lab} = 90°$
o, ● Ground State of ^{10}Be
□, ■ First Excited State of ^{10}Be
Calculation for Ground State of Singham et al.
$d\sigma/d\Omega$ (μb/sr)
1.0
0.1
0.01
160
180
200
220
240
260
280
300
320
340
$E_{\gamma\,lab}$ (MeV)

Fig IV-14

trometer.

B. Interpertation and Comparison With Theory.

A great deal can be understood about the fianl differential cross sections for $^{10}B(\gamma,\pi^+)^{10}Be$ shown in Fig. IV-14 by comparing them to the transverse electron scattering form factorrs for the analog states in ^{10}B shown in Fig. IV-15. The beam energies needed to produce pions at 90° lab angle with the appropriate momentum transfers are included in the horizontal scale to facilitate comparison with the photopion data. It can be seen that the shapes are both decreasing with increasing momentum transfer, as expected since the combinations of transition densities that enter into both processes are similar, as explained in Chapter One. Due to the increasing pion absorption at higher energies, the photopion cross section can be seen to be decreasing significantly faster than the elastic scattering form factors.

It is also interesting to compare the ratio of the excited to ground states for the photopion reaction and the form factors. This is done in Fig. IV-16, where the dashed line was taken from the Helm model fits to the form factors shown in Fig. IV-15 (AN79). It can be seen that the ratios are quite similar for the two processes, as expected, since the dominant multipolarities are the same for both states in this region (M3 components dominate) and hence the same tensor couplings to the photoproduction op-

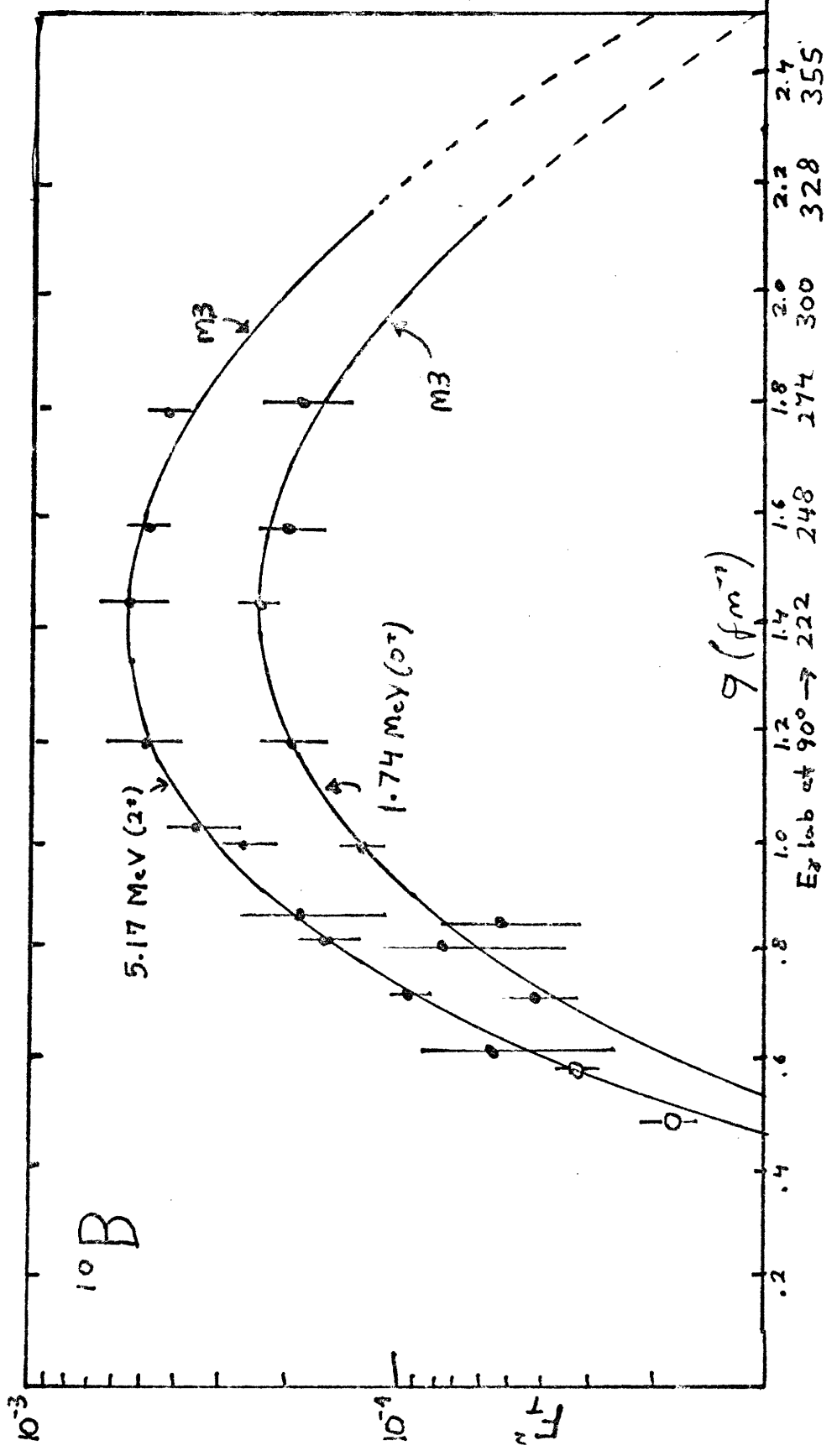
10^{-3}
10^{-4}
FT_2
^{10}B
5.17 MeV (2⁺)
1.74 MeV (2⁺)
M3
M3
.2
.4
.6
.8
1.0
1.2
1.4
1.6
1.8
2.0
2.2
2.4
E_x lab at 90° → 222 248 274 300 328 355
q (fm⁻¹)

Fig IV-15

erator and final state pion wave functions will be involved in both cases.

A more quantitative comparison can be made for the ground state, where a still preliminary calculation of M. Singham and F. Tabakin is shown as the solid line in Fig. IV-14. (SI79) The approximations made in their calculations have been examined in Chapter One, and are the same as used in the calculation of the total cross section for $^{12}C(\gamma,\pi^-)^{12}N$ and $^{7}Li(\gamma,\pi^-)^{7}Be$ described in the previous chapters. We recall that the most important approximations are that of the impulse approximation and the use of a coordinate space version of the Blomqvist-Laget operator (BL77) that tends to overestimate the Born terms and underestimate the delta terms for pion energies above 100 MeV. They used Cohen-Kurath wave functions for the initial and final nuclear states that give a good fit to the form factor shown in Fig. IV-15, and pion optical potential parameters of Stricker et al (ST79) that give good fits to the pion elastic scattering data for carbon.

It can be seen that the calculation accounts for the data reasonably well in general, but seems somewhat low at the higher energies. It is interesting to speculate that this may be due to two-body and medium corrections not taken into account in the production operator part of the calculation and only in a phenomenological way in the final state interactions. Before any such conclusion

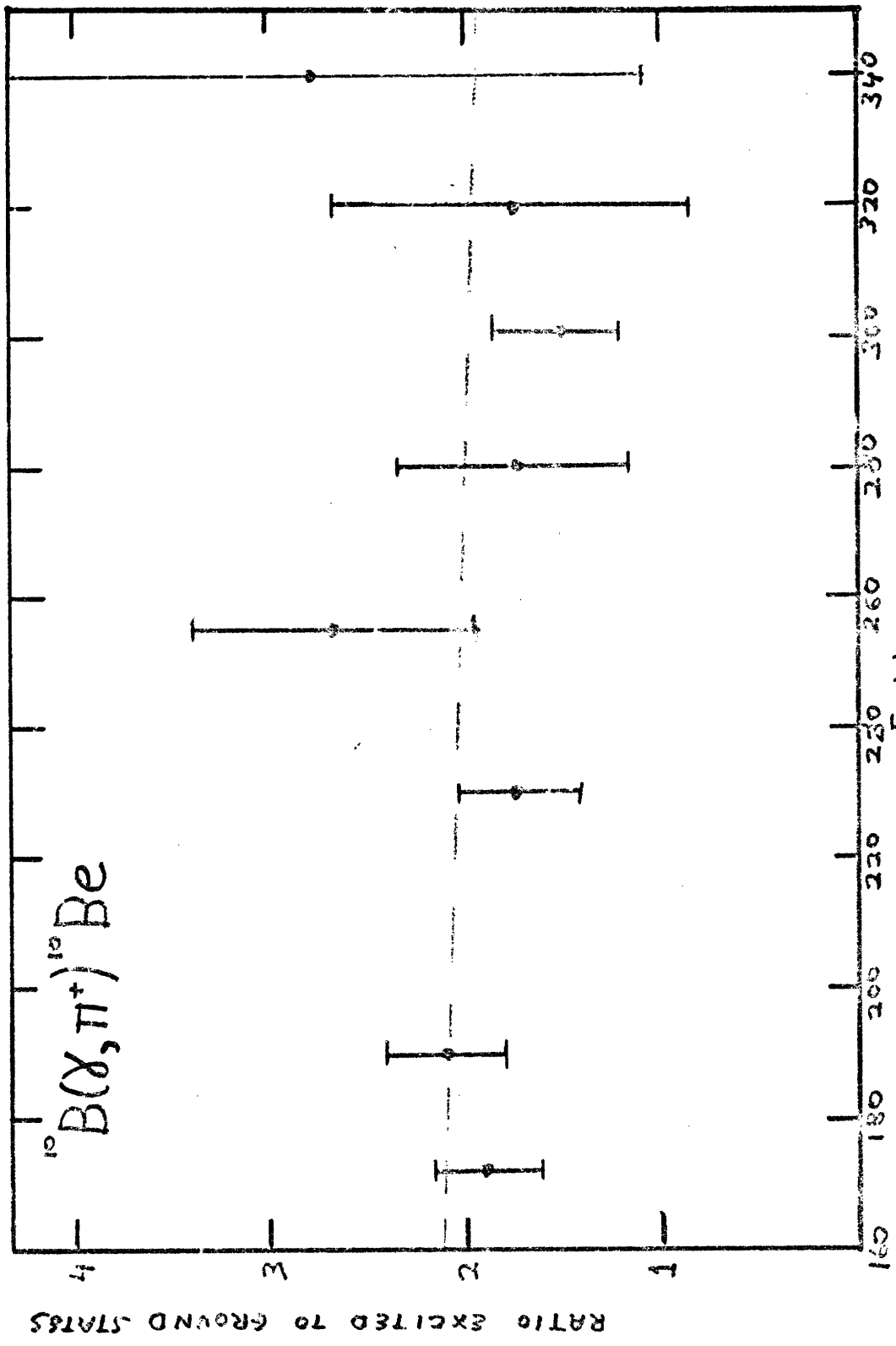
$^{10}B(\gamma,\pi^+)^{10}Be$
RATIO EXCITED TO GROUND STATES
E_γ lab
160
180
200
220
240
260
280
300
320
340
1
2
3
4

Fig. III-16

could be drawn, the results of a momentum space calculation in which the elementary production operator can be handled more exactly should be awaited. The formalism for such a calculation has been worked out by Singham, but has not yet been implemented in the form of a computer code.

We conclude that the present data for the differential cross sectios for $^{10}B(\gamma,\pi^+)^{10}Be$ to two separate states in Be should provide a valuable test case for studying photopion production from complex nuclei in the delta region. For this reason current plans include extending the present measurements to other angles and measuring the total cross section by the activation method in the near future.

IV-11. Results for $^{16}O(\gamma,\pi^+)^{16}N$.

In this section we present the final differential cross section results for $^{16}O(\gamma,\pi^+)^{16}N$ to sum of the four closely spaced low lying levels of the residual nucleus at 90° lab scattering angle and for pion energies from 84 to 204 MeV. Although we cannot separate the contribution of these closely spaced states of ^{16}N, there is a large gap (2.48 MeV) to the next state, which is the breakup channel $^{15}N+n$, so we can readily measure the sum of their contributions. The quantum numbers of these states are 0-, 1-, 2-, and 3-, with excitation energies of .12, .40, 0.0, and .30 MeV respectively. Thus the spacing between the levels is about the same as our effective resolution.

We will first describe the manner in which the data were analyzed, followed by a discussion of the available calculations and how their results compare to the present data.

A. Data Analysis.

The target used was made of 282 mg/cm^2 BeO. Placed at 45° with respect to the beam direction, the average energy loss for electrons and pions was 0.81 MeV. This large energy loss meant that the real-to-virtual ratios we obtained using the Ta radiators did not have as good statistics as they might have due to the large resolution smearing for real photons. However, the resolution for virtual photons from the target comes mostly from straggling and hence was not more than .30 MeV, much smaller than the level spacing to the 2.48 MeV state. One of the better spectra that was obtained is shown in Fig. IV-17. Even with cuts to remove almost all of the positron background, a relatively large muon background remained for this run, which was taken with a photon energy of 236 MeV and a pion energy of 84 MeV. The running time was 2.6 hours with an average current of 45 μA.

As in the boron case, the nominal endpoint channels were found to be in good agreement with those found by the fitting program when the endpoint channel was allowed to vary as a free parameter. Allowing the background to have a slope was found to be essential to give good fits, espe-

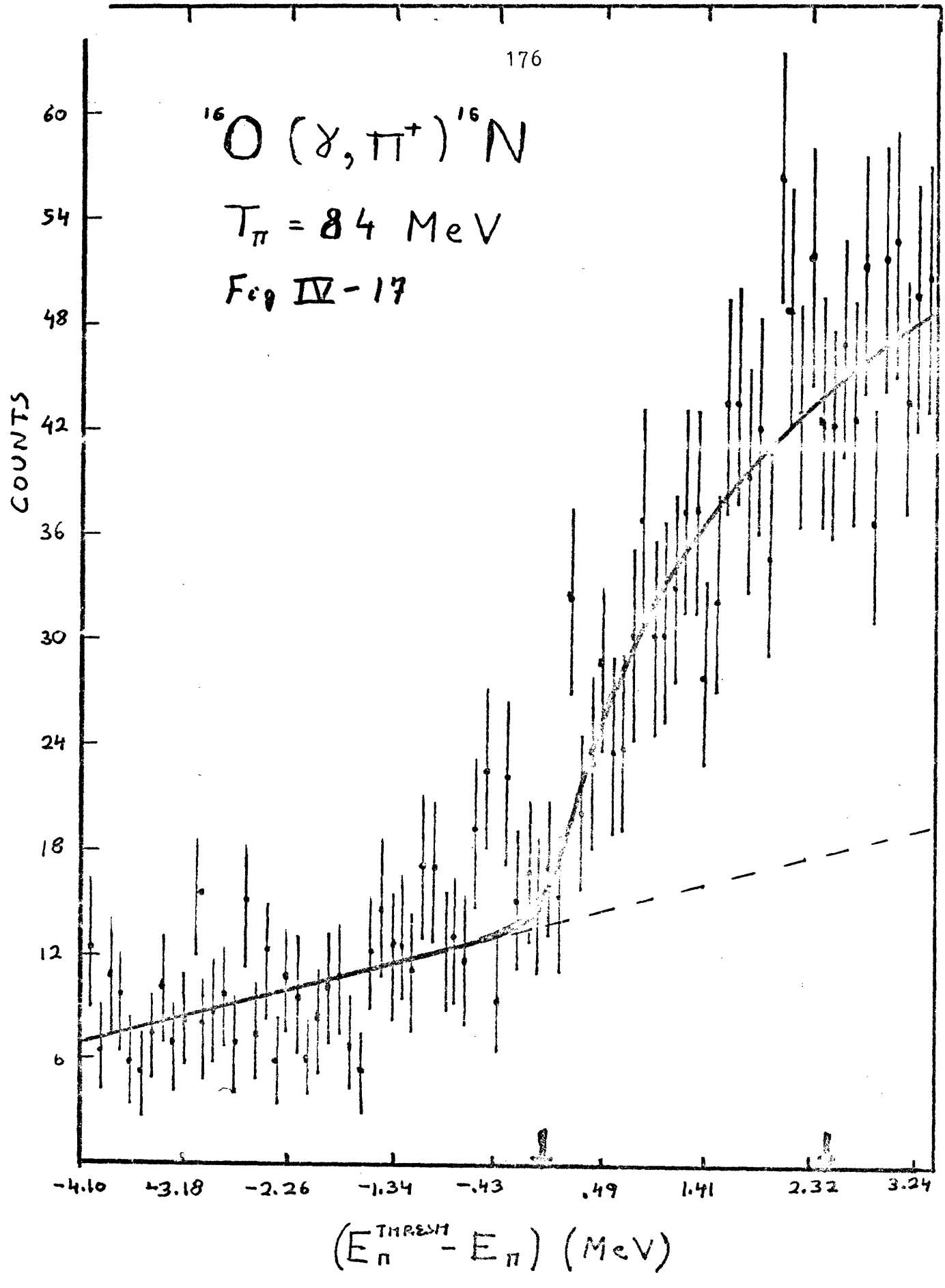
$^{16}O(\gamma,\pi^+)^{16}N$
$T_\pi = 84$ MeV
Fig IV-17
COUNTS
60
54
48
42
36
30
24
18
12
6
-4.10
-3.18
-2.26
-1.34
-.43
.49
1.41
2.32
3.24
$(E_\pi^{THRESH} - E_\pi)$ (MeV)

cially at lower energies where we have better statistics. The cross sections were therefore extracted using slopes but no energy shifts with the same cuts as were used in the hydrogen normalization. The results were then converted to cross sections in the same manner as was done for boron.

The final results are plotted as a function of incident photon energy in Fig. IV-18. The corresponding pion energies are from 84 to 204 MeV.

B. Description of Available Calculations.

There presently are two calculations available for this reaction, that of Nagl (NA79), shown as the solid line in Fig. IV-18, and that of Devanathan et al (DA79), shown as the dashed line. In this section we will discuss some of the approximations made in these calculations, following which they will be compared to the present data.

The calculation of Nagl (solid line) uses the Helm model (UB72) to fit the electron scattering transverse form factor shown in Fig. IV-19 (SI69). The solid line in the figure is the result of the random phase approxiation calculation for this form factor of Donnelly et al (DO75). Nagl used the Kisslinger model optical potential with the density dependent terms derived from the scattering phase shifts with the appropriate kinematic transformations and the Ericson-Ericson effect included. He fit the density-squared terms to agree with the elastic

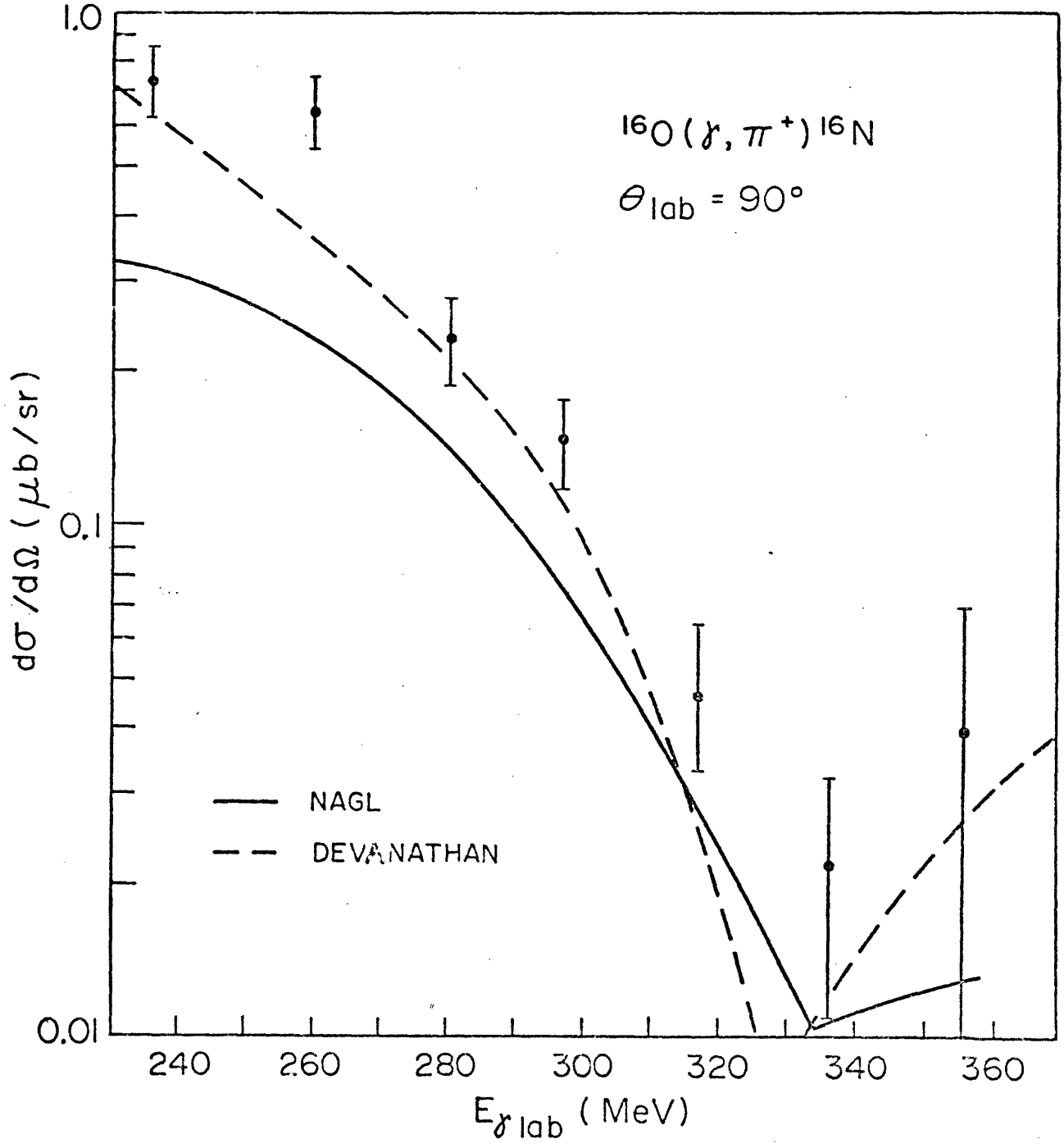
1.0
0.1
0.01
$^{16}O(\gamma, \pi^+)^{16}N$
$\theta_{lab} = 90°$
$d\sigma/d\Omega$ (μb/sr)
NAGL
DEVANATHAN
240
260
280
300
320
340
360
$E_{\gamma\,lab}$ (MeV)

Fig IV-18

scattering data for negative pions from oxygen of Binon et al (BI70) and Bercaw et al (BE72). The p-wave density squared absorbtion is found to be strongly energy dependent and is responsible for a large reduction in the photopion cross sections at the peak of the delta resonance. He used the CGLN formalism for the elementary amplitute, with the numerical values of the coefficients taken from Berends (BE72). He uses the numerical value of half the momentum transfer for the nuclon momentum, which is not treated as a gradient operator in this approximation. This does not appear to be a bad approximation, since when the nuclear momentum was set to zero very little change was found in the results. The pion momentum was treated correctly.

The calculation of Devanathan and Girija suffers from some more drastic approximations. The most serious of these is the fact that they do not take into account the effect of the pion gradient operator in the elementary operator. This becomes most important at lower pion energies, where volume production dominates. Hence it is not surprising that their cross sections blow up at low pion energies, reaching values much larger than the total cross section measurement of Meyer et al (ME65) (see Chapter One). This would also explain the increasing discrepancy with the Nagl calculation as one moves from higher to lower energies. The other problem with their results

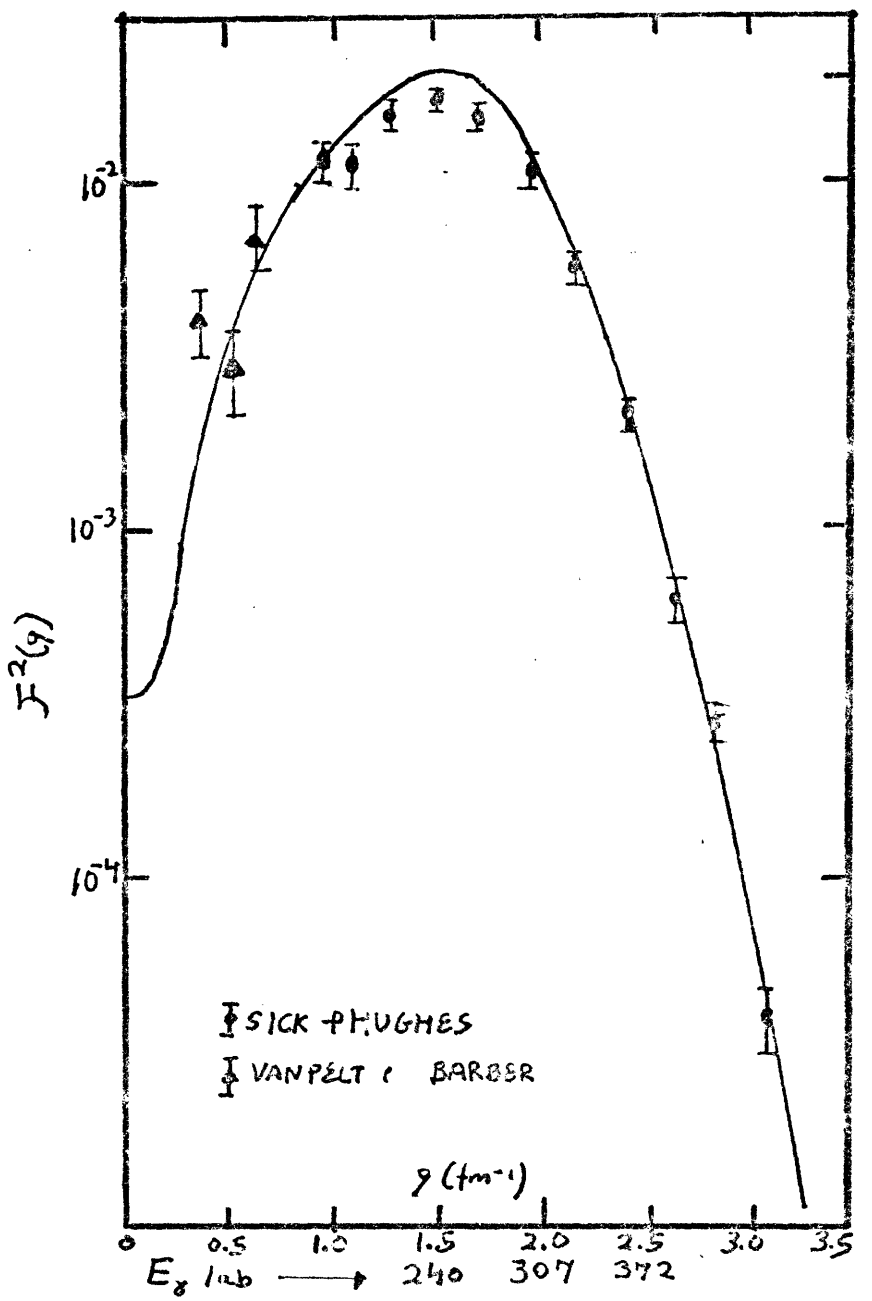
10^{-2}
10^{-3}
10^{-4}
$F^2(q)$
SICK PHUGHES
VANPELT & BARBER
q (fm^{-1})
0
0.5
1.0
1.5
2.0
2.5
3.0
3.5
E_e lab ⟶
240
307
372

Fig IV-19

could come from the nuclear structure input. They investigated the effects of using independent particle harmonic oscillator wave functions, Wood Saxon wave functions (PE69), and Rho's wave functions calculated from the theory of Migdal (RH67). These produce progressively smaller results for the photopion cross sections, but only the last is in agreement with muon capture rates. No attempt was made to compare with electron scattering results, so it is not clear whether or not the Migdal wave functions would reproduce the form factor in our kinematic region or not.

C. Comparison with Theory and Conclusions.

We therefore conclude that, of the two calculations, that of Nagl is probably the more reliable. This being the case, it remains a puzzle as to why the experimental data is so much higher than this calculation, especially at the lower energies where one would not expect special problems from the pion distorted waves.

Unlike with the Singham calculation, there should not be large problems from the manner in which Nagl treated the elementray operator, except that in his approach there are no nucleon momentum gradients. There could, however, be problems with the Helm model paramatrization of the form factor. Since four states are being summed over, there are many ways to fit the Helm model parameters to the form factor, but the different fits may not give the

same photopion cross sections. These effects are currently under investigation by Nagl. A calculation by Singham using the transition densities of Donnelly (D075), which are directly connected to the shell model, is also under way. The effects of many-body interactions and medium corrections to the elementary operator have yet to be investigated, as has the detailed sensitivity of the calculations to different pion optical potentials.

We conclude that the present data, although suffering somewhat by virtue of summing over four final states, should provide a valuable testing ground for photopion calculations in the delta region. For this reason, the present measurements will be extended to other angles and the total cross section will be measured by the activation method in the near future.

IV. 12 Summary and Conclusions.

In this section an attempt will be made to summarize the experimental experience as well as the physics information gained from the present measurements. It should be remembered that these are the first differential cross section measuremnts in the delta region and thus represent the first step in an ongoing program in which experimental techniques still have a great scope for improvement and the advent of more refined calculations will dictate the cases most interesting for furthur study.

A. Experimental Experience.

The single most important thing learned from the present measurements is that they are possible to perform in a reasonable amount of running time with acceptable statistical precision. Preliminary studies at 45^{o}, 90^{o}, and 140^{o} indicated that the background rates from positrons for (γ,π^{+}) reactions were tolerable, but that rejection ratios of at least 1:100,000 would be needed to overcome the electron background levels to (γ,π^{-}) reactions. A lucite total absorption counter was developed that was sufficiently good for (γ,π^{+}) reactions, but not (γ,π^{-}). A silica aerogel detector that should cure this problem is presently under construction.

From the point of view of actually taking data, we have found that reactions that proceed to levels in the final nuclei with large apacings betwen them offer several advantages. Firstly, there are more available photons for larger separations, and secondly thicker targets can be used to increase the count rate since the effects of target resolution are relatively smaller. Using elastic electron scattering has been found to be useful in determining incident beam energies and electron detection efficiencies. This reaction could also be used in the future to measure the thickness of packed powder targets. We have found quasi-free pion production to be a useful tool in investigating the response of the detection system to the large numbers of pions and muons produced by this re-

action.

A convenient method of obtaining absolute normalizations has been found in the $p(\gamma,\pi^+)n$ reaction. Due to limitations in the maximum available beam energy, this cannot be used at back angles, where work will be needed to ensure that the efficiency of the detection system will be stable over long periods of time. We have found that muons arising from pions that decay in flight can add significant backgrounds and distort the observed pion spectra. The new aerogel detector will not, in general, discriminate between pions and muons, but hope is offered by the possibility of placing a high resolution lead glass total absorption lead glass detector as the last element in a back-up array.

When the experience summarized in the previous paragraphs is put to work in conjunction with the new high resolution, large solid angle pion spectrometer presently under construction, it should be possible to obtain very clean pion endpoint spectra for both (γ,π^+) and (γ,π^-) reactions for a wide range of pion energies and a complete range of angles.

B. Physics Information and Conclusions.

The present measurements provide valuable new input to the store of availabe photopion information since they are the first differential cross section measurements to discrete states of the final nuclei in the delta region.

We have found the present results to be in reasonable agreement with the currently available distorted wave impulse approximation calculations, but, particularly in the case of $^{16}O(\gamma,\pi^+)^{16}N$, the data seems to be somewhat larger than the calculations. Since many of the calculations are still undergoing active refinement by their authors, it would be premature at this stage to draw any conclusions about the validity of the impulse approximation in the delta region. Although it would be rather surprising if the impulse approximation were to work well in this region, due to the delta dominance of the production operator for which substantial medium corrections would be expected based on the corrections found by Hirata et al (HI79) to be necessary to similar diagrams in pion interactions, the other aspects of the reaction mechanism should be carefully treated before any definite conclusions could be drawn.

We conclude that the present data should provide a valuable testing ground for the more refined calculations now in progress. For this reason the differential cross section measurements will be extended to other angles and target nuclei in the near fuure, and total cross section measurements will also be performed to constrain the total strengths predicted by the calculations.

Figure Captions

1. Kinematic relations between pion lab angle, pion energy, beam energy, and momentum transfer for $p(\gamma,\pi^+)n$ adn $^{16}O(\gamma,\pi^+)^{16}N$ differential cross sections.

2. Location of the five 2" Cerenkov counters in the pit of the Bates Energy Loss Sptectrometer.

3. a) Relative pulse heights in ten inches of lucite for electrons and pions. b) Ratio of pulse heights for muons and pions to those from electrons compared with expected values.

4. Pulse height spectra used to extract the ratios shown in Fig. IV-3a.

5. Definition of angles and distances used in folding targetresolution effects into the shapes of pion spectra.

6. Breakdown of the components of a typical endpoint spectrum.

7. Illustration of the shape of the calculated muon contaminations from pion decays within the first spectrometer drift space for two different original pion spectra.

8. Detection efficiency for electrons as determined by elastic electron scattering as a function of energy.

9. Quasi-free production of pions from carbon for two different incident beam energies at 90° . The

   solid points were taken with the first two Cerenkov counter required in coincience as the event trigger, open circles correspond to the first Cerenkov only required in coincidence with the transverse wire chambers. Hatched zones are predicted number of counts based on the data of EP78.

10. Ratio of number of pions observed when the second Cerenkov counter was required in the event trigger to the number observed when it was not as a function of energy. The dashed line is the maximum value expected due to the effects of pion absorption in the first counter.

11. Typical spectrum for $p(\gamma,\pi^+)n$. The ^{12}C contribution from the CH target has been subtracted. The solid line shows the best two-parameter fit for a flat background plus the pion shape expected from the real and virtual photons.

12. Efficiencies for pions as a cuntion of pion energy as determined from the $p(\gamma,\pi^+)n$ reaction. The two lowest energy points were taken without the second Cerenkov counter in the coincidence requirement for the event trigger. All other points had this requirement. The solid line shows the extrapolated values used at higher energies, with the estimated error indicated by the dashed lines.

13. Thypical spectrum for $^{10}B(\gamma,\pi^+)^{10}Be$. The solid line showsthe best four parameter fit for a straight line plus a pionspectrum shape for each of the two levels observed in ^{10}Be.

14. Final differntial cross section for the $^{10}B(\gamma,\pi^+)^{10}Be$ reaction. The circles indicate the contributions form the ground state in ^{10}Be, while the squares indicate the first excited state. THe opne squares and circles are from RO79, while the solid symbols represent the present data. The solid line is the calculation of SI79.

15. Transverse electron scattering form factors for theanalog states in ^{10}B to those probed in the photopion reaction (AN79). Solid lines are Helm model (UB72) fits to the data.

16. Ratios of photopion differential cross sections for $^{10}B(\gamma,\pi^+)^{10}Be$ from the first excited state in ^{10}B to those from the ground state. The dashed curve is the ratio of the fits to the form factors shown in the previous figure.

17. Typical spectrum for $^{16}O(\gamma,\pi^+)^{16}N$. THe solid curve is the result for the best three parameter fit for a straight line plus a shape for the sum of the four lowest lying levels in ^{16}N.

18. Final differential cross sections for $^{16}O(\gamma,\pi^+)^{16}N$. The observed final states are the the sum of the four lowest lying levels in ^{16}N. The solid curve is the calculation of NA79, the dashed curve that of DE79.

19. Transverse form factor for the 13 MeV complex in ^{16}O which are the analog states in ^{16}O to the states in ^{16}N probed by the photopion reaction. Solid line is calculation of DO75.

Chapter Five

Conclusions and Outlook for the Future.

In this chapter the information derived from the present experiments is put in the context of the photopion field as a whole and some of the current ideas in the field of nuclear physics. Suggestions are then made regarding which future experiments should be performed to yield the most interesting physics information and how these might fit in with the new experimental facilities currently under construuction at the Bates Linear Accelerator.

V.1 What Has Been Learned.

The total cross sections for two reactions, $^{12}C(\gamma,\pi^-)^{12}N$ and $^{7}Li(\gamma,\pi^-)^{7}Be$ have been found to be in good agreement with DWIA calculations in the pion energy region from 0 to 120 MeV. Interpretation was facilitated since only the ground state in ^{12}N was observed and only the first two states in ^{7}Be were summed over, unlike the case of most of the other total cross section measurements in this energy region. A wider scope can be given to the interpretation since the first case involves a transition to a non-analog state while in the second case the inital and final states are isobaric analogs of each other.

This agreement is contrary to what has been observed in the total (π^+,π^0) cross sections for ^{13}C, ^{10}B, and

^{7}Li, also measured by the activation method and for which the initial and final states are the same as in the photopion reactions. Here the DWIA calculations are found to be considerably smaller than experiment in the 80 to 200 MeV range. Only when Pauli blocking effects, different proton and neutron radii, and local energy changes are included does the calculation for ^{13}C come into agreement with the data (LA79). Part of these effects can be explained in terms of an effective spreading interaction in the isobar-doorway model, where the interactions of the propogating deltas in the nuclear medium are found to be important (SA79).

Many of these effects are taken into account by the use of phenomonological optical potential (fit to elastic scattering data) in the photopion calculations. But the medium interactions of the intermediate propogating deltas in the photoproduction vertex have not been specifically evaluated. Since true pion absorption is a large part of the total pion reaction cross section the delta resonance region, one would expect such processes to seriously alter the delta prouction amplitudes. Modifications to the Born terms in the photopion amplitude could also occur when an intermediate nucleon interacts with another particle in the nuclear medium, but their importance is hard to estimate since a microscopic decomposition of the physical amplitude would be nequired to evaluate the relative con-

tribution of higher order self-energy diagrams relative to the bare contact term, for which no medium effects would be possible. For the delta part of the physical amplitude, one would expect the effects to be significant since even the bare diagram (no self-energy bubbles) involves an intermediate delta.

Viewed in this context, it is perhaps not so surprising that the total cross sections we have measured are in good agreement with DWIA calculations. This is because the energy region where we have good error bands on the data is from 0 to 80 MeV, well below the peak of the delta amplitude at 150 MeV. Above 80 MeV the error bars on the cross sections become increasingly large due to the intrinsic difficulties involved in unfolding yield curves (see Appendix 1). Measurements of yield curves to over 500 MeV incident electron energies with very good statistical and systematic errors will be necessary to extract accurate total cross sections in the 80 to 200 MeV region. Such an experiment could best be done with the $^{12}C(\gamma,\pi^-)^{12}N$ reaction, due to the unusually small two-step background, and should soon be possible when the beam energy doubling recirculator becomes operational at the Bates Linac.

The above discussion may also have a bearing on why DWIA calculations do not do as good a job in describing the differential cross sections for $^{16}O(\gamma,\pi^+)$ and

$^{10}B(\gamma,\pi^+)$ to discrete states of the residual nuclei as they did for the total cross sections previously discussed. Since the differential cross sections were taken at energies directly spanning the peak of the delta amplitude, the medium corrections to the elementary operator may be larger. However, the calculations are still in the preliminary stages, and furthur refinements will be needed before any definite conclusion can be drawn. At this stage, the calculations do a remarkably good job in accounting for the shapes of the differential cross sections as a function of pion energy, and agree fairly well for the ^{10}B case in absolute magnitude (although all of the data points lie on the high side of the calculation). In the case for ^{16}O, we have the puzzling situation that, of the two available calculations, the one with the most dreastic approximations best describes the absolute magnitude for the data.

We conclude that the present experiments have advanced the field of photopion physics in two ways. The total cross section measurements are the first to be performed with relatively high precision in the 0 to 120 MeV range to small numbers of final discrete states and therefore for which the nuclear structureis sufficiently well understood as to permit reasonably accurate DWIA calculations. The differential cross section measurements are the first to discrete states in the delta region (80 to

200 MeV pions). Since the nuclear structure is well understood for the chosen cases, they should provide the first benchmark measurements for testing the impulse approximation in this energy region.

V.2. Outlook for the Future.

As we have mentioned several times before, the present measurements are part of an ongoing program to learn about photopion interactions in nuclei. We will therefore now review the outlook in the immediate future, particularly as concerns the extensions of the present measurements, following which a brief outline of the broader picture, which may eventually include new facilities such as a 1 to 4 GeV 100% duty cycle electron accelerator.

A. Total ($\gamma\pi$) Cross Section Measurements.

As for the extension of the total cross section activation measurements, there are two interesting directions to pursue. The first is to study other nuclei. This direction can be divided into two catagories: those with previous measurements and those without. The principle requirement for the chosen cases should be that the number of particle stable final states is small and that their nuclear structure should be fairly well understood.

The first catagory has one obvious candidate, the $^{13}C(\gamma,\pi^-)^{13}N$ reaction. The residual nucleus in this case has only one particle stable state which is the mirror of the ^{13}C ground state, greatly facilitating the nuclear

structure aspects of calculations. Furthermore the analogous pion charge exchange reaction has been observed and has caused a great flurry of theoretical activity to explain the large cross sections observed. The reason that this reaction has not yet been observed is the great difficulty found in separating the 1.3 MeV endpoint β^+ spectrum of ^{13}N, which has a lifetime of 10 minutes, from the much more abundant 1.0 MeV decay of 20 minute half-life ^{11}C produced by the $^{13}C(\gamma,2n)^{11}C$ reaction. We beleive the technical problems can be overcome by using both a plastic scintillator in coincidence with two NaI detectors to detect the annihilation gamma rays and the half life information to separate the contributions from ^{13}N and ^{11}C. The measurements will therefore be attempted this coming spring and summer.

In addition, there are several cases in the second catagory, that of total cross section measurements by the activation method with prior measurements, for which the existing data is of sufficiently poor quality and the physics interests are sufficiently great that better measurements would seem justified. Four such cases are the $^{16}O(\gamma,\pi^+)^{16}N$, $^{14}N(\gamma,\pi^-)$, $^{11}B(\gamma,n^+)$ and $^{10}B(\gamma,\pi^+)^{10}Be$ reactions. The first and last cases are of particular interest in view of the current activity in measureing the differential cross sections. The second case has only an order of magnitude measurement at present, yet should be

interesting since the calculations of Singham and Tabakin have shown that this reaction should be particularly sensitive to gradient terms in the elementary operator, even close to threshold, because of a suppresion of the $\hat{\sigma}\cdot\hat{\varepsilon}$ term due to the selection rules between the initial and final states involved. This can be seen in the strongly suppresssed Gamov-Teller matrix element. Another nice feature of this case is that only one final state is involved (see Chapter One for more discussion on all of these cases). Since the half-lives for all of these cases are in the 7 second to 1 minute range, they can easily be measured in conjunction with the planned $^{13}C(\gamma,\pi^-)$ measurement with very little increase in the beam time required. Plans are therefore underway to measure these cases as well.

The other direction that should be pursued is to extend the measurements to higher energies, so that the unfolded cross sections in the 100 to 200 MeV range might have error bars at the 20% level. This will require a beam energy higher than presently available at Bates, and very small sytematic and statistical error bars on the yield points. This type of measurement should become possible in about a year when the energy is doubled at Bates. Since the error on the extrapolation of the two step background increases at higher energies, the best case to extend to higher energies would be the $^{12}C(\gamma,\pi^-)^{12}N$ reac-

tion, for which the two-step background is anomolously low.

B. Differential Cross Sections for (γ,π) Reactions.

As far as differential cross sections are concerned, it is clear that the present measurements for pion energies from 80 to 200 MeV at only one angle are somewhat unsatisfactory. Complete angular distributions are desirable to map the energy dependence of the photopion interactions at different values of the transferred momentum. By keeping the momentum transfer fixed, the nuclear structure aspects remain more or less constant, and the physics we are presently interested in, namely the pion nucleus interactions and the effects of the nuclear medium on the production amplitude, can be most clearly seen. As a first step in this direction, we hope to repeat the $^{10}B(\gamma,\pi^+)$ and $^{16}O(\gamma,\pi^+)$ measurements from 80 to 200 MeV at 45^o. As can be seen from Fig. IV-1, the momentum transfer will then be almost constant, and it will be possible to normalize to the $p(\gamma,\pi^+)n$ reaction over the entire energy range. This run should take place in the near future, at which time the new aerogel detector will also be tested and the feasibility of performing (γ,π^-) reactions will be investigated.

The next stage in the program should start in about a year when the new high resolution, large solid angle, large momentum acceptance, and short flight path spectrom-

eter designed escpecially for pions comes on the air. It should then be possible to take complete angular distribution (including 0^{o}) in a reasonable amount of running time. It is planned to have the capability of a pure photon beam for those angles and polarities where the resolution is not required to be extremely good but the background from electrons or positrons is intolerably high. We will now discuss the most likely candidates for study with this new spectrometer over the next few years.

The first case to study should be a benchmark measurement of a reaction for which the nuclear structure is well understood, target construction and impurities are not overwhelmingly difficult, there are large gaps between the final states of the residual nucleus, and for which the cross sections are not expected to be unusually small. The most likely candidate at this point seems to be the $^{10}B(\gamma,\pi^{\pm})$ reactions, for which all of these requirements are met. Another possibility is the $^{13}C(\gamma,\pi^{-})^{13}N$ reaction. Complete angular distributions over the entire available energy range could be used to to study pion and delta interactions in nuclei and to test the validity of the impulse approximation over a wide range of kinematic conditions.

It would be then interesting to go to a heavy nucleus, where the effects of the pion distorted waves should be much more pronounced. A good candidate is the

$^{209}Bi(\gamma,\pi^+)^{209}Pb$ reaction, for two reasons. The first is that this is one of the very rare cases in nuclei heavier than oxygen where the level spacing between the ground and first excited state is reasonably large (about 1 MeV). The second is that these nuclei are well described in the shell model since they both have only one valence nucleon outside closed shells for both protons and neutrons, and they have been well studied with electron scattering. The two problems likely to be encountered are with the low melting point of the target and the much higher background rates from a high Z element.

Moving back to lighter nuclei, the cases of $^{14}N(\gamma,\pi^-)$ should be interesting. The calculations of Singham and Tabakin have shown that there is greater sensitivity to pion and nucleon gradient terms within the production operator than in most transitions due to the suppression of the normally dominating $\vec{\sigma}\cdot\vec{\epsilon}$ term. This can be seen in the highly suppressed Gamov-Teller matrix element for ^{14}N. They have also predicted minima in the angular distributions, not seen in the form factors, which arise from interferences in the pion optical potential. These cases should be particularly useful in probing the pion wave function within the nucleus. The extremeley large gaps between the ground and first excited states (about 4 and 6 MeV) help to compensate for the rather small cross sections involved (typically from 100 nb/sr on down to less

than 1 nb/sr in the 0 to 150 MeV range).

Another case of particular interest should be to investigate the ground states of the residual nuclei in the $^{12}C(\gamma,\pi^{\pm})$ reactions in the region of the second maximum in the form factor, where the large deviation seen from shell model predictions may be due to critical opalescence, in which pions are condensed within the nuclear medium.

Another interesting set of reactions is $^{3}He(\gamma,\pi^{\pm})$. The three body problem is the heaviest for which almost exact solutions can be found, and ^{3}He offers the advantage of being tightly bound, so that the density is similar to that found in heavier nuclei (unlike the loosely bound deuteron). Since the pion wave functions should not be much distorted by final state interactions due to the small size of the nucleus, these cases should be ideal testing grounds for second order processes and possible medium corrections.

Of course, there are many other cases one could investigate, maybe even with the purpose of learning about the nuclear structure of spin flip, isospin flip transitions to which the photopion reaction is particularly sensitive, as has been done for the 4.5 MeV complex of states in the $^{12}C(\gamma,\pi^{+})$ reaction, but the cases mentioned in the last paragraphs should go a long way in improving our understanding of the problems of pion and delta interac-

tions in nuclei and the corrections needed to the elementary amplitude needed to understand the photopion creation process in complex nuclei.

C. Coherent (γ,π^o) Production

A similar experiment to measuring charge pion differential cross sections is to examine (γ,π^o) differential cross sections. We should first mention that recent experimental activity has been concentrated on measuring total cross sections in the threshold region. Here it has been found, particularly for the lightest elements, that large corrections from second order diagrams (such a charge pion being produced and charge exchange scattering from another nucleon) and binding effects are needed to explain the cross sections. At higher energies, the delta production is completely dominant, unlike for charged pions where the Born terms also have large contributions, so that this experiment should be a good tool for studying delta propagation through the nuclear medium, especially if coherence is developed by requiring that the final nucleus be in its ground state. Such experiments are presently being conducted at Bates, where a large neutral pion spectrometer is being built in which each of the two gamma rays from the decay of the neutral pions are detected with lead glass Cerenkov detectors and their position measured with wire chambers. The results from these experiments should be especially interesting in light of re-

cent isobar-doorway model calculations. (SA79)

D. Bound State Pions.

Another single arm class of experiments that can be done is to scatter a particle from a nucleus, leaving a pion bound in an atomic orbit. This type of experiment could complement the measurements of pionic level spacings and widths observed with the X-rays produced as stopped pions cascade down the atomic levels before being absorbed by the nucleus, and offers hope for examining levels not reached in the cascades (such as the 1s level) in heavier nuclei. Although the backgrounds from the elastic radiative tail and quasi-free electron scattering are very large, it may be possible to observe the pions produced in the 1s orbital in the $^{27}Al(e,e'\pi^+)^{27}Si$ reaction if the calculation of Koch (KO79) for this cross section is correct. Plans are in progress to look for this narrow (41 KeV) peak at one pion-mass energy loss using electron scattering at Bates in the near future. An earlier attempt using carbon was unsuccesful, perhaps in part because the spectrometer resolution and signal to noise ratios had not been optimized. Even if the planned run is succesful, 10 hours of running with good resolution will be necessary to distinguish the peak from the over 100 times greater backgrounds.

A proposal has also been made to use proton scattering to look for these pionic levels. This may offer some

hope, since one can run at more forward angles than with electrons since there is no radiative tail to contend with and one can therefore be placed further from the quasi-elastic peak. In addition the bound state pion cross sections increase rapidly at forward angles. The interpertation may be somewhat clouded due to the strong interactions of the probe in this case.

E. Inclusive Experiments

Another aspect to single arm (γ,π) reactions are inclusive experiments in which the nucleus is not left in a definite discrete bound state, but generally is broken up with single or multiple nucleon emmisions. Such experiments are presently rather difficult to interpert since large Monte-Carlo programs are needed to trace the strongly interacting pion and struck nucleon (or nucleons) through the nucleus as they propagate. With monochromatic photon beams which only allow one specific energy transfer to the nucleus at a time these experiments could eventually offer hope for learning about pion absorption in nuclei, since the pions are produced throughout the nuclear volume (as opposed to when discrete states of the final nucleus are involved the transition densities tend to peak at the surface since generally valence nucleons only can participate). This is tied up with the fact that the inclusive cross sections contain most of the photopion reaction stregth, and therefore should also be valuable in studying

the dominant reaction mechanisms. Such experiments (which have only been done to now at Bates with bremsstrahlung beams) are currently taking place at Bonn and elsewhere and should soon be possible to perform with very good counting rates at Bates when a tagged photon or monochromatic photon system is installed.

F. Coincidence Experiments.

Coincidence experiments offer considerable advantages in pinpointing the specific kinematic conditions for a given process. Examples of this can be seen in the (e,e'N) and (p,p'N) experiments which can directly map the momentum distribution of the struck nucleons, or (e,e'NN) and (p,p'NN) reactions which directly probe two-body correlations in nuclei.

The reason that there have not been many coincidence experiments involving complex nuclei to date is simply that the counting times are intolerably long and large backgrounds produce accidental coincidences which mask the process being measured. With a 100% duty cycle machine the problems of signal to noise ratios can be vastly improved, and, with the high currents now available from modern linacs and the large solid angles of the new spectrometers now under construction in the new hall at Bates, the counting times should become very reasonable even for very small cross sections.

We have not yet discussed the question of meson ex-

change currents explicitly, as this would take a whole chapter in itself, but it should be noted at this point that the photo-and electrodisintigration of the deuteron experiments, in which two or more particles are measured in coincidence, could shed valuable light on this aspect of nuclear physics.

As far as directly examining photopion reactions, there are two types of experiments which should be very interesting. The first is to detect a scattered electron and a pion in coincidence, with the pion being emmited in the direction of the virtual photon. If the pion does not strongly interact as it leaves the nucleus, this type of experiment could be used to directly map pion wave functions. This interpretation would be most clear at low energies, where the pion interactions are mostly electromagnetic, while at higher energies the effects of pion interactions could be directly investigated.

The other type of coincidence experiment would be aimed at probing off-shell photon effects in the elementary production vertex. Particularly interesting would be the $p(e,e'p)\pi^0$ and $d(e,e'd)\pi^0$ reactions in which the recoil nuclei are detected with one spectrometer and the scattered electrons with another. Caculations by this author have predicted very large effects when the photons are far from real. However, it can be shown that such experiments, whether they examine charged or neutral pion pro-

duction, are much more favorable when high beam energies (over 1 GeV) are used. This would then seem like a good set of experiments for when the 1 to 4 GeV 100% duty cycle electron accelerator is built. The same could be said of the experiments mentioned in the last paragraph, but here the high energy is not as crucial.

Another experiment that can be done with coincidence experiments using the deuteron is to search for the delta contribution to the deuteron wave function. Appropriately designed experiments in which a Δ^{++} is identified by kinematics, angular distributions, and polarization properties could then measure both the static and dynamic form factor for the delta explicitly.

V.3. Concluding Remarks

It is hoped that the preceeding discussion, which has forcibly become more brief and less specific as the experiments become less well defined and furthur off in the future, has given the reader a feel for the large and exciting scope for expansion in the field of photopion physics. Although entire parts of the field (such as (π,γ) reactions, search for isomeric states, and so on) have been neglected, it should nonetheless have become clear that a great deal of new information about the fundamental properties of pion and delta interactions in nuclei will be learned in the next decade or so as advances in both experimental apparatus and accelerator facilites make it

possible to do ever more specific experiments in which individual components of the reaction mechanism are separatly dissected. Tied with this must of course be a corresponding advance in our ability to handle the complicated numerical calculations needed to make accurate predictions, as well as advances of our fundamental understanding of pions and nucleons and the basic mechanism for their strong interaction.

Appendix 1

Unfolding Method

There are several methods to determine the cross section when the yield

A.1 $$Y(E_0) = \int_{E_{THRESH}}^{E_0} \Phi(E_0, E)\, \sigma(E)\, dE$$

is known the a certain level of precision. E_0 is the energy of the incident electron, E is the energy of the photon, $\Phi(E_0, E)$ is the photon spectrum function, and $\sigma(E)$ is the cross section to be determined. Older approaches involve taking the first differences bewteen succesive yield points to determine the average cross section in that bin. The basic problem with that approach is that the errors rapidly propogate as one goes to higher energies and the cross section thus extracted will exhibit many unphysical fluctuations. Other methods such as the Penfold-Leiss method rely on higher order differences between the yield points but still do not do well when the errors on the individual yield points are significant compared to the difference between succesive yield points. Attempts to smooth the cross sections obtained with these methods are usually ambiguous as they rely on the feeling of the experimenter to determine what would constitue a significant fluctuation.

One way to take advantage of the knowledge that the cross section is a slowly and smoothly varying function of energy is to paramatrize it put some function that has this

property and solve the resulting matrix equation. Two such functions are polynomials in powers of the energy above threshold, and a sum of gaussians positioned over the data points with widths that respresent the expected resolution of the experiment to peaks and valleys in the cross section. The cross section is then expressed as

A.2 $$\sigma(E) = \sum_i F_i(E)$$

where

A.3 $$F_i(E) = (E - E_{THRESH})^{i-1}$$

for polynomials and

A.4 $$F_i(E) = e^{-\frac{(E-E_i)^2}{G_i^2}}$$

for gaussians. In the first case E_{THRESH} is the threshold energy for the reaction, and in the second the E_i are the centroid energies of the guassians and the G_i are their widths. It has been found that for equally spaced yield points, the E_i should be roughly equally spaced, and the G_i should be at least twice the spacing between succesive guassians.

If there are N data points and we wish to fit them using M free parameters, we find the yield equation can be transformed into a matrix eguation

A.5 $$X_{ij}\, a_j = Y_i$$

where Y_i are the data points and X_{ij} is defined by

A.6 $$X_{ij} = \int_{E_{THRESH}}^{E_0} \Phi(E_i, E)\, F_j(E)\, dE$$

If we now define

A.7 $$\chi^2 = \sum_i (Y_{CALC} - Y_i)^2 W_i$$

where W_i are the inverses of the error bars on the data points squared, and the set the derivitives of χ^2 with respect to each of the a_i equal to zero, we obtain the matrix equation

A.8 $$A_{ij}\, a_j = B_i$$

where A_{ij} is an M by M matrix given by

A.9 $$A_{ij} = \sum_K X_{Kj}\, X_{Ki}\, W_K$$
$$\text{and} \quad B_i = \sum_K X_{Ki}\, Y_K\, W_K$$

The M by M error matrix E_{ij} is then found by inverting A_{ij}. The errors on the coefficients a_i are given by the square roots of the diagonal elements E_{ii}, and the error on the cross section at a particular energy E can by found by evaluating

A.10 $$d\sigma(E) = \sqrt{\sum_{ij} E_{ij}\, F_i\, F_j}$$

In order to test these methods, two models for the cross section, one a constant value of 5 microbarns, and another which follows the form of a calculation for the $^{12}C(\gamma,\pi^-)^{12}N$

cross section, have been used. The model cross sections were first converted to yields using the bremmstrahlung photon flux, then the yield points calculated at 10 MeV intervals were randomly changed to simulate five percent statistical errors. These curves were then analyzed with the unfolding method described above for polynomials of various maximum degrees. The results are shown in figure A-1. It can be seen that up until 80 MeV above threshold the differences from the theoretical curve are well within the 5 percent error range, but increase rapidly as we approach the end of the data set, as each point becomes less and less important in determining the cross section have been used. The error bars calculated by the program are shown in each case for only one paramatrization, and it can be seen that they represent fairly well the range of curves obtained from different paramatrizations.

Thus we conclude that at least for the type of data under consideration it is reasonable to derive the cross section from the yield curve for a wide range of physically reasonable paramatrizations and represent the final result as an error band that encompasses the range of obtained results. Care should be taken, however, to remember that that the error range indicated by this band is highly correlated, and the error on the total integrated cross section will be much less than the sum of the errors shown at each energy for which there is an experimental yield point.

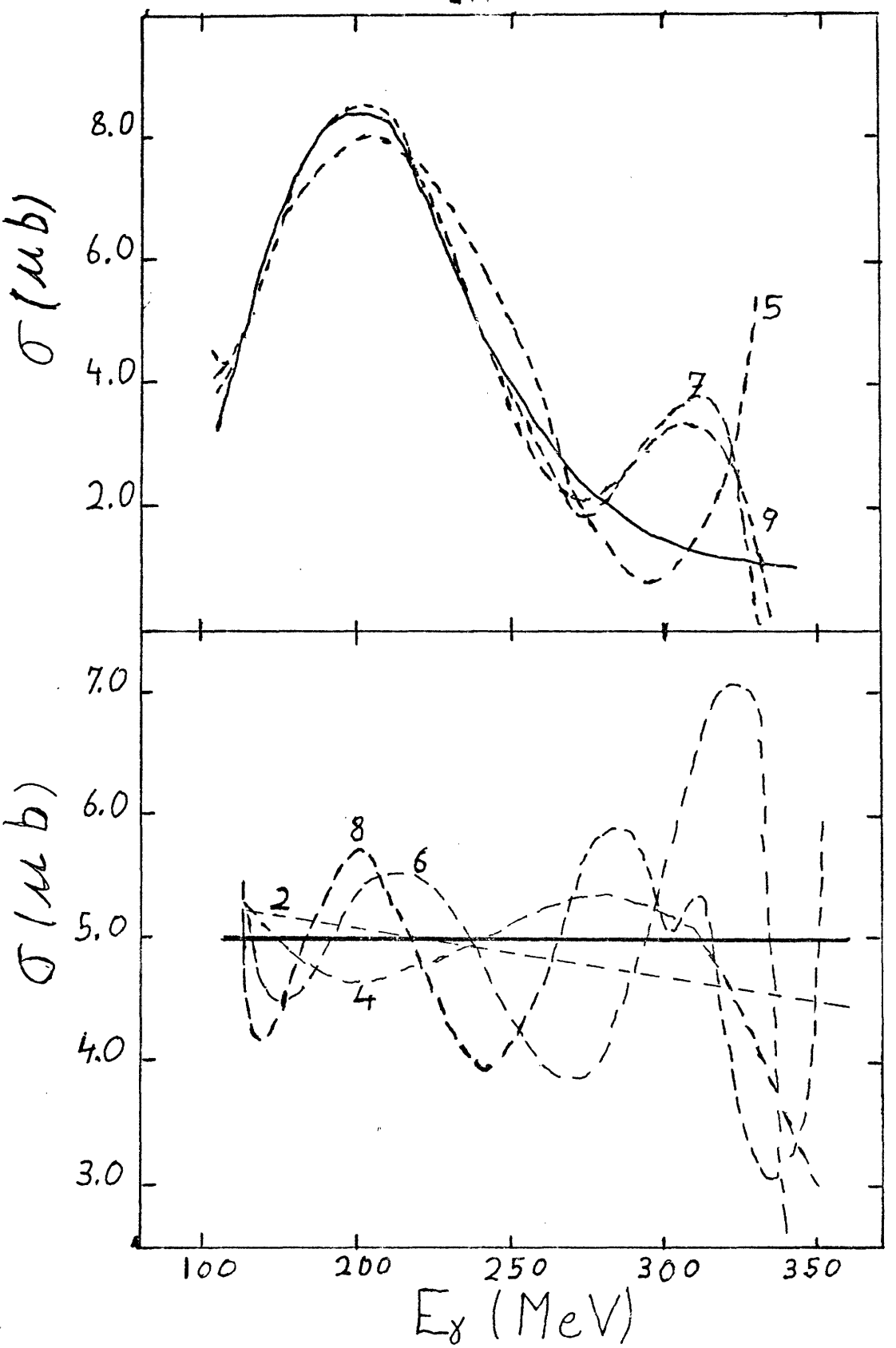

Fig A.1. See text for explanation of curves

References

AJ70 F. Ajzenberg-Selove, Nucl. Phys. A152 (1970) 1.

AJ71 F. Ajzenberg-Selove, Nucl. Phys. A166 (1971) 1.

AJ72 F. Ajzenberg-Selove, Nucl. Phys. A190 (1972) 1.

AJ74 F. Ajzenberg-Selove, Nucl. Phys. A227 (1974) 1.

AJ75 F. Ajzenberg-Selove, Nucl. Phys. A248 (1975) 1.

AL79 J. C. Alder et al, Photopion Nuclear Physics, (P. Stoler Ed.), Plenum Press, N.Y. 1979 pages 101 and 107.

AL79 J. Alster and J. Warszawski, Phys. Reports 52 (1979) 7.

AN79 Ansaldo et al , Nucl. Phys. A322 (1979) 527

BA70 G. Backenstoss, Ann. Rev. Nucl. Sci. 20 (1970) 467.

BA78 C. J. Batty et al, Phys. Rev. Lett. 40 (1978) 931.

BE55 H. Bethe and F. de Hoffman, Mesons and Fields, Vol. II, Dow, Peterson and Company, Evanston, Ill. 1955 for a review of early papers on photopion physics.

BE67 F. A. Berends et al, Nucl. Phys. B4 (1967) 1, 54.

BE69 P. R. Bevington, Data Reduction and Error Analysis for the Physical Sciences, McGraw-Hill, N.Y. 1969.

BE71 F. A. Berends and D. L. Weaver, Nucl. Phys. B30 (1971) 575.

BE75 F. A. Berends and D. L. Weaver, Nucl. Phys. B84 (1975) 342.

BE72 R. W. Bercaw et al. Phys. Rev. Lett. 29 (1972) 1031.

BE76 A. M. Bernstein et al, Phys. Rev. Lett. 37 (1976) 819.

BI70 F. Binon et al. Nucl. Phys. B17 (1970) 168.

BL71 I. Blomqvist et al, Nucl. Phsy. A162 (1971) 193.

BL77 I. Blomqvist et al, Phys. Rev.C5(1977) 988.

I77 I. Blomqvist and J. M. Laget, Nucl. Phys. A280 (1977) 405.

BO79 E. C. Booth, Photopion Nuclear Physics (P. Stoler Ed.) Plenum Press, N. Y. 1979. p129.

Ch67 Chew, Goldberger, Low, and Nambu, Phys Rev 106 (1957) 1345.

CL74 A. S. Clough et al, Nucl. Phys B76 (1974) 15.

CO57 B. Cook et al, Phys. Rev. 106 (1957) 300.

CO65 S. Cohen and D. Kurath, Nucl. Phys. 73 (1965) 1.

DA57 R. H. Dalitz and D. R. Yennie, Phys. Rev 105 (1957) 1598.

DE64 D. Denisov et al, JETP 19 (1964) 1007.

DE79 V. DeCarlo, N. Freed, and W. Rhodes, Photopion Nuclear Physics (P. Stoler Ed.) Plenum Press, N.Y. 1979, p. 165.

DI71 V. di Napoli, Nucl. Instr. Meth. 93 (1971) 77.

DE79 V. Devenathan, private communication.

DO75 T. W. Donnelly and J. D. Walecka, Ann. Rev. Nucl. Sci. 25 (1975) 329.

DO76 H. Dollard et al, Phys. Lett. 63B (1976) 416.

DU78 J. Dubach and W. Haxton, Phys. Rev. Lett. 41 (1978) 1453

DY62 P. Dyal and J. P. Hummel, Phys. Rev 127 (1962) 2217.

DY77 S. A. Dytman et al, Phys. Rev. Lett. 38 (1977) 1059.

DY78 S. Dytman et al, Phys Rev C18 (1978) 2316.

EP74 V. D. Epaneshnikov et al, Sov. J. Nucl. Phys. 19 (1974) 242.

EP78 G. Epstein, M. Singham, and F. Tabakin, Phys. Rev C17 (1978) 702.

EY78 S. Eyink, Bonn thesis IR-78-4, February 1978, Physics Institute, Bonn University, Germany.

FL79 J. Flanz. Private communication and to be published.

FR72 J. I. Friedman and H. W. Kendall, Ann. Rev. Nucl. Sci. 22 (1972) 203.

HA78 W. C. Haxton, Phys. Lett. 76B (1978) 165.

HI79 M. Hirata et al, Ann. Phys. 120 (1979) 205.

HY70 G. Hylthen, Nucl. Phys. A158 (1970) 225.

JO76 B. Johnsson, M. Nilsson, and K. Lindgren, Lund Preprint LUNFDG/(NIFR 3005)/I-18 (1976)

JO78 B. Johnson et al, Nucl. Phys. A296 (1978) 444.

KE79 B. D. Keister (to be published) "Phase-Shift-Equivalent-Potenials and Pion Nucleus Reactions".

KO79 J. Koch. Private communication.

LA79 R. Landau and A. Thomas, submitted to Phys. Rev. Lett. Sept. 1979.

LE79 M. Leitch. M.I.T. Thesis January 12 1979.

LU79 Private communication from Lund cyclotron (from I. Blomqvist).

MA73 J. L. Matthews and R. D. Owens, Nucl. Instr. and Meht. 91 (1973) 37.

ME65 R. Meyer, W. Walters, and J. P. Hummel, Phys Rev 128B (1965) 1421.

MO79 E. Moniz, M.I.T. C.T.P. preprint 797 (1979) and Photopion Nuclear Physics, Plenum Press, (P. Stoler Ed.) 1979, p. 335.

NA79 A. Nagl and H. Uberall, Photopion Nuclear Physics, Plenum Press, N.Y. 1979, p. 155 and private communication

NA79 I. Navan et al, 8th Internation Conference on High Energy Physics and Nuclear Structure, Abstracts p 48, TRIUMF, August 1979.

NO71 V. I. Noga et al, Ukranian J. Phys. 16 (1970) 1850.

NO79 V. I. Noga et al. Kharkov Linac Internal Report.

OC72 J. S. O'Connell et al, Phys. Rev C6 (1972) 719.

PA79 N. Paras, M.I.T. Thesis, June, 1979.

PE69 S. M. Perez, Nucl. Phys. A136 (1967) 599.

PE79 J. P. Perroud, Photopion Nuclear Physics, (P. Stoler Ed.), Plenum Press, N.Y. 1979 Page 69.

PF72 W. Pfeil and D. Schwela, Nucl. Phys. B45 (1972) 379.

RH67 M. Rho, Phys. Rev. Lett. 18 (1967) 671.

RO79 D. Rowley. Private Communication. This data was taken by an RPI/MIT collabaration at the Bates Linac using the low energy pion spectrometer.

SA68 L. Saunders, Nucl. Phys B7 (1968) 293 and M.I.T. Thesis.

SA79 A. N. Saharia and R. M. Woloshyn, Phys. Lett. B84 (1979) 401.

SI69 I. Sick et al, Phys. Rev Lett. 23 (1969) 1117.

SI79 M. Singham and F. Tabakin, Phys. Rev Lett. 43 (1979) 1476 and private communications.

ST79 K. Stricker, H. McManus, and T. A. Carr, Phys. Rev. C19 (1979) 929.

TA79 F. Tabakin, Photopion Nuclear Physics, (P. Stoler Ed.) Plenum Press, N.Y. 1979 p. 301.

UB72 H. Uberall et al, Phys. Rev C6 (1972) 1911.

WI79 J. Winhold et al, private communication.